A STUDY OF LASER-ARC HYBRID WELDABILITY OF NICKEL-BASE INCONEL 738 LC SUPERALLOY

By

OYEDELE TEMITOPE OLA

A Thesis Submitted to the Faculty of Graduate Studies of

The University of Manitoba

in Partial Fulfillment of the Requirements for the Degree of

DOCTOR OF PHILOSOPHY

Department of Mechanical and Manufacturing Engineering

University of Manitoba

Winnipeg

ABSTRACT

Precipitation strengthened nickel-base superalloys, such as IN 738, are very difficult to weld by fusion welding techniques due to their high susceptibility to heat-affected zone (HAZ) intergranular liquation cracking. An improvement in weldability could be realized by the deployment of innovative welding processes and/or the modification of the materials' microstructural characteristics. Laser-arc hybrid welding is a relatively new welding process that appears to possess great potentials for joining the difficult-to-weld nickel-base superalloys. The research described in this Ph.D. dissertation was initiated to perform a systematic and comprehensive study of the cracking susceptibility of nickel-base IN 738 superalloy welds made by laser-arc hybrid welding process, and how to minimize it by using a combination of pre-weld microstructural modification and the application of various welding filler alloys.

Laser-arc hybrid welding produced a desirable weld geometry in IN 738 Superalloy. Cracking did not occur exclusively in the fusion zone. Analysis of the fusion zone material using EPMA, SEM, TEM and EBSD revealed elemental partitioning pattern, the presence of secondary solidification reaction constituents and the grain structure of the fusion zone. Non-equilibrium liquation of various second phases that were present in the alloy prior to welding contributed to intergranular liquation in the HAZ that consequently resulted in extensive HAZ intergranular cracking. A very significant reduction in HAZ intergranular liquation cracking was achieved by the use of an industrially deployable and effective pre-weld thermal processing procedure developed during this research work. This novel procedure, designated as FUMT, was developed on the basis of the control of both boride formation and intergranular boron segregation in the pre-weld material.

Propensity for HAZ intergranular liquation cracking in the weldments was also observed to vary depending on the Al+Ti+Nb+Ta concentration of the weld metal produced by different filler alloys, which can be attributed to variation in the extent of precipitation hardening in the weld metals. The newly developed FUMT treatment procedure, coupled with the selection of an appropriate type of filler alloy, is effective in reducing HAZ intergranular cracking both during laser-arc hybrid welding and during post-weld heat treatment (PWHT) of the laser-arc hybrid welded IN 738 superalloy.

ACKNOWLEDGEMENT

I want to thank my advisor, Dr. M.C. Chaturvedi, for accepting me into the doctoral degree program and for giving me an opportunity to work on this attractive project. I also thank my co-advisor, Dr. O.A. Ojo, for his contributions to the success of this research. My advisors were timely in their advice, provided all the research facilities that I required and believed that I could do the work successfully. I am grateful.

I thank the University of Manitoba for the Award of the University of Manitoba Graduate Fellowship and other scholarships. I also thank NSERC for their financial support. I am grateful to Red River College and StandardAero for their partnership which established the Centre for Aerospace Technology and Training (CATT) where all the welding aspects of this research were carried out. I thank Anand Birur and Justin Grehan of Standard Aero Limited for their help.

I am grateful to Dr. R.K. Sidhu and Dr. Abdul Khan for their assistance. The technical support of Don Mardis, Mike Boswick, John Vandorp and Cory Smit is appreciated. I also thank Elenor Friesen for her support. I appreciate Richard Buckson and Dr. Lawrence Osoba. I also thank my friends – Dr. Tolulope Sajobi, Dr and Dr Mrs Opapeju, Dr. Seun Idowu, Dr. Dotun Akinlade, Dr. Dami Adedapo and Akinbola George.

I thank my dad and mum for their encouragement and advice. I also thank my siblings – Oyewole Ola, Oyefunke Afolayan and Oyekunle Ola. I appreciate my lovely daughter, Inioluwa, for her understanding. I am overwhelmed by the continual love and support of my wife, Olaitan, throughout my studies. Lastly, I honour the source of life and wisdom, the Almighty God, without whom this work would have been impossible.

DEDICATION

I dedicate this doctoral dissertation to

My Father, Solomon I. Ola

And

My Mother, Caroline A. Ola

For the invaluable sacrifice that they made toward my upbringing and career pursuit

TABLE OF CONTENTS

LIST OF FIGURES

LIST OF TABLES

COPYRIGHT PERMISSIONS

Figure 2-2: Source - S. Kuo, Welding Metallurgy, 2nd ed., John Wiley & Sons Inc., Hoboken, 2003. *Reprinted with permission from Global Rights Dept., John Wiley and Sons, Inc. (5 June, 2013).*

Figure 2-3: Source - S. Kuo, Welding Metallurgy, 2nd ed., John Wiley & Sons Inc., Hoboken, 2003. *Reprinted with permission from Global Rights Dept., John Wiley and Sons, Inc. (5 June, 2013).*

Figure 2-4: Source - ASM Handbook Volume 6: Welding, Brazing and Soldering, Copyright 1993. *Reprinted with permission from ASM International (17 May, 2013). All rights reserved*. www.asminternational.org

Figure 2-5: Source - ASM Handbook Volume 6: Welding, Brazing and Soldering, Copyright 1993. *Reprinted with permission from ASM International (17 May, 2013). All rights reserved*. www.asminternational.org

Figure 2-6: Source - ASM Handbook Volume 6: Welding, Brazing and Soldering, Copyright 1993. *Reprinted with permission from ASM International (17 May, 2013). All rights reserved*. www.asminternational.org

Figure 2-7: Source - ASM Handbook Volume 6: Welding, Brazing and Soldering, Copyright 1993. *Reprinted with permission from ASM International (17 May, 2013). All rights reserved*. www.asminternational.org

Figure 2-8: Source - K. Masubuchi, Analysis of Welded Structures, 1980, ISBN 0-08-0261299. *Reprinted with permission from the Author, Koichi Masubuchi (30 June, 2013)*

Figure 2-9: Source: R.G. Baker, Philosophical Transactions of the Royal Society of London, Series A: Mathematical and Physical Sciences, Vol. 282 No 1307 (1976) pp.207-223. *Reprinted with permission from The Royal Society (21 May, 2013)*

Figure 2-10: Source: R.G. Baker, Philosophical Transactions of the Royal Society of London, Series A: Mathematical and Physical Sciences, Vol. 282 No 1307 (1976) pp.207-223. *Reprinted with permission from The Royal Society (21 May, 2013)*

Figure 2-11: Source - J.J. Pepe and W.F. Savage, Weld. J., Vo146 (No. 9), 1967, p 411-s. *Reprinted with permission from the American Welding Society (2 August, 2013)*

Figure 2-12: Source - J.J. Pepe and W.F. Savage, Weld. J., Vo146 (No. 9), 1967, p 411-s. *Reprinted with permission from the American Welding Society (2 August, 2013)*

Figure 2-13: Source – W.F. Savage and C.D. Lundin, Weld. J., Vo1 44 (No. 10), 1965, p 433-s. *Reprinted with permission from the American Welding Society (2 August, 2013)*

Figure 2-14: Source - Weld. J., Vo1 26 (No. 11), 1947, p 673-s. *Reprinted with permission from the American Welding Society (2 August, 2013)*

Figure 2-15: Source - Industrial Heating, Vol. 53 (No 12) Dec. 1986, p.28. *Reprinted with permission from Industrial Heating (31 July, 2013)*

Figure 2-16: Source - Hybrid Laser-Arc Welding, Edited by Flemming Ove Olsen, Copyright 2009, ISBN 978-1-84569-652-8. *Reprinted with permission from Woodhead Publishing Limited (14 May, 2013)*

Figure 2-17: Source - Hybrid Laser-Arc Welding, Edited by Flemming Ove Olsen, Copyright 2009, ISBN 978-1-84569-652-8. *Reprinted with permission from Woodhead Publishing Limited (14 May, 2013)*

Figure 2-18: Source - Hybrid Laser-Arc Welding, Edited by Flemming Ove Olsen, Copyright 2009, ISBN 978-1-84569-652-8. *Reprinted with permission from Woodhead Publishing Limited (14 May, 2013)*

Figure 2-19: Source - C.V. Hyatt, K.H. Magee, J.F. Porter, V.E. Merchant and J.R. Matthews: Weld. J., (2001) pp.163s-172s. *Reprinted with permission from the American Welding Society (2 August, 2013)*

Figure 2-20: Source - Y. Naito, S. Katayama and A. Matsunawa: First International Symposium on High-Power Laser Macroprocessing – Proceedings of SPIE, Vol. 4831 (2003) pp. 357. *Reprinted with permission from The International Society for Optical Engineering (23 May, 2013) and one of the Authors, Seiji Katayama (4 June, 2013).*

Figure 2-21: Source - Y. Naito, S. Katayama and A. Matsunawa: First International Symposium on High-Power Laser Macroprocessing – Proceedings of SPIE, Vol. 4831 (2003) pp. 357. *Reprinted with permission from The International Society for Optical Engineering (23 May, 2013) and one of the Authors, Seiji Katayama (4 June, 2013).*

Figure 2-22: Source - Hybrid Laser-Arc Welding, Edited by Flemming Ove Olsen, Copyright 2009, ISBN 978-1-84569-652-8. *Reprinted with permission from Woodhead Publishing Limited (14 May, 2013)*

Figure 2-23: Source - Hybrid Laser-Arc Welding, Edited by Flemming Ove Olsen, Copyright 2009, ISBN 978-1-84569-652-8. *Reprinted with permission from Woodhead Publishing Limited (14 May, 2013)*

Figure 2-24: Source - Hybrid Laser-Arc Welding, Edited by Flemming Ove Olsen, Copyright 2009, ISBN 978-1-84569-652-8. *Reprinted with permission from Woodhead Publishing Limited (14 May, 2013)*

Figure 2-25: Source - Hybrid Laser-Arc Welding, Edited by Flemming Ove Olsen, Copyright 2009, ISBN 978-1-84569-652-8. *Reprinted with permission from Woodhead Publishing Limited (14 May, 2013)*

Figure 2-26: Source - Hybrid Laser-Arc Welding, Edited by Flemming Ove Olsen, Copyright 2009, ISBN 978-1-84569-652-8. *Reprinted with permission from Woodhead Publishing Limited (14 May, 2013)*

Figure 2-27: Source - Hybrid Laser-Arc Welding, Edited by Flemming Ove Olsen, Copyright 2009, ISBN 978-1-84569-652-8. *Reprinted with permission from Woodhead Publishing Limited (14 May, 2013)*

Other: Source - O.T. Ola, O.A. Ojo and M.C. Chaturvedi: Materials Science and Technology, 2013, Vol. 29, No 4, pp.426-438. *Reprinted with permission from Maney Publishing (12 July, 2013)*

CHAPTER 1

INTRODUCTION

1.1 Background Information

Superalloys are utilized at a higher proportion of their actual melting point than any other class of broadly commercial metallic material. Applications of superalloys include aircraft, marine and industrial gas turbines, as well as in rocket engines, nuclear reactors and petrochemical equipment [1]. Superalloys are divided into three classes, namely nickel-base superalloys, cobalt-base superalloys and iron-base superalloys. Nickel-base superalloys are used in the manufacturing of hot section components of aero and land-based gas turbines, where the demand for higher operating temperatures requires the use of materials that possess excellent high temperature strength and hot corrosion resistance. IN 738 superalloy is a γ' precipitation strengthened nickel-base superalloy used for such gas turbine applications.

Fabrication of new gas turbine components and the repair of service-damaged parts usually require joining, economically, by the use of various welding techniques. A major factor that limits the weldability of precipitation strengthened nickel-base superalloys that contain a substantial amount of Al and Ti, such as IN 738 superalloy, is their high susceptibility to heat-affected zone (HAZ) intergranular cracking during joining [2, 3]. Intergranular HAZ cracking in IN 738 has been attributed to a combination of two major factors. The rapid thermal cycling experienced by the HAZ during welding causes non-equilibrium intergranular liquation, which consequently results in the formation of crack-susceptible microstructure [4]. HAZ cracking eventually occurs under the influence of a

driving force, the thermally-generated tensile stress that causes decohesion along one of the solid-liquid interfaces at the liquated grain boundary [4, 5]. The inherent weld cracking problems and the subtle dimensional changes occurring during gas turbine service introduce significant complications during repair of components [6]. Therefore, improvement in the ease of repairing gas turbine components by improving the weldability of precipitation strengthened nickel-base superalloys is desirable. This could be realized by the deployment of innovative welding techniques and/or the re-engineering of the materials' microstructural characteristics.

Advancements in fusion welding led to the invention of laser-arc hybrid welding. Laser-arc hybrid welding is a relatively new welding process in comparison to other traditional welding processes. This process has been reported to be better than laser beam welding and arc welding. The laser-arc hybrid welding concept was first introduced by Steen et. al. at the Imperial College of Science and Technology, London, when they combined CO_2 laser beam with tungsten inert-gas (TIG) for welding and cutting materials [7-9]. In laser-arc hybrid welding, a laser beam and an arc interact, simultaneously, in the same molten weld pool, where both heat sources affect and complement each other [10-12]. The synergistic effects of the interaction of the laser beam and the arc during hybrid welding have been reported to result in a combination of the best characteristics of laser welding and arc welding [7, 12-14]. Proper setting of the laser and arc parameters resulted in significant advantages (over the individual laser welding and arc welding processes), which include increased welding speed and weld penetration, improved gap and misalignment tolerance, enhanced process stability, reduced porosity and quality advantage. This has made the process attractive and promising for the joining of several

materials, especially those that are difficult to weld. Laser-arc hybrid welding is currently attracting a great deal of attention in the joining of different materials in different industries [12, 15-18]. This technique appears to have great potentials for joining difficult-to-weld precipitation-strengthened nickel-base superalloys. However, the mere application of an innovative and potentially advantageous welding technology does not guarantee the elimination of the inherent weldability problem encountered during fusion welding of precipitation strengthened nickel-base superalloys.

1.2 The Problem and the Research Objective

1.2.1 The Problem

As mentioned in the last section, nickel-base IN 738 superalloy contains a substantial amount of Al and Ti, which form the major strengthening γ' phase in the alloy. Like other precipitation strengthened nickel-base superalloys, IN 738 superalloy is known to be very difficult to weld by fusion welding techniques due to its high susceptibility to heat-affected zone (HAZ) integranular cracking during welding. A significant mitigation or total elimination of this cracking problem will immensely improve the ability to fabricate and repair aero and land-based gas turbine components manufactured from IN 738 superalloy. Laser-arc hybrid welding is becoming attractive for joining various materials with several reported advantages and appears to possess great potentials for achieving high quality welds in nickel-base superalloys. However, this process is rarely applied to joining nickel-base superalloys for gas turbine applications. Studies on the weldability of IN 738 superalloy, and the identification of weldability improvement opportunities, during laser-arc hybrid welding is considered critical in the application of this technology for the joining of the alloy. The objective of this work is presented as follows.

1.2.2 Research Objective

This research was initiated to perform a systematic and comprehensive study of the cracking susceptibility of nickel-base IN 738 superalloy welds made by laser-arc hybrid welding process, and how to minimize it by using a combination of

A. pre-weld microstructural modification through thermal treatment
B. the application of various welding filler alloys

1.3 Research Methodology

In order to accomplish the stated objective, the following research methods were adopted.

1. The application of various materials selection and preparation procedures including electro-discharge machining and standard metallography, before and after welding
2. The re-engineering of the microstructure of the alloy prior to welding by the application of various pre-weld heat treatments based on proven metallurgical principles.
3. The actual laser-arc hybrid welding of work pieces (butt welding) by using the robotic 6 kW laser – 500 A MIG hybrid welding equipment at the Centre for Aerospace Technology and Training, Winnipeg, Canada
4. The application of various nickel-base welding filler alloys during welding based on precipitation hardening characteristics.
5. The deployment of different advanced characterization techniques, including scanning electron microscopy (SEM), electron probe microanalysis (EPMA), transmission electron microscopy (TEM), electron back-scattered diffraction

(EBSD) analysis, etc, to studying the response of IN 738 superalloy to laser-arc hybrid welding process.

6. Extensive weldability assessment by microscopy
7. Gleeble physical simulation of the thermal cycle experienced in the HAZ of the alloy during welding
8. Thermodynamic calculation of solidification behaviour

1.4 Summary of Major Findings

Laser-arc hybrid welding has been demonstrated to have the ability to produce high-quality welds in IN 738 superalloy. The process produced a desirable weld profile in the alloy and no cracking occurred exclusively in the fusion zone. Elemental partitioning pattern in the weld metals showed that Ti, Ta, Nb, Mo, Al and Zr partitioned into the interdendritic regions of the fusion zone and resulted in the formation of MC-type carbides. Non-equilibrium liquation of various second phases that were present in the alloy prior to welding contributed to intergranular liquation in the HAZ, which consequently resulted in extensive HAZ intergranular cracking.

A drastic reduction in HAZ intergranular liquation cracking was achieved by the development of an industrially deployable and effective pre-weld thermal processing procedure (FUMT) based on the control of both boride formation and intergranular boron segregation. Also, propensity for HAZ intergranular liquation cracking in the weldments was observed to vary depending on the concentration of Al + Ti + Nb + Ta in the weld metals produced by different filler alloys, which can be attributed to variation in the extent of precipitation hardening produced in the weld metals. Additionally, shrinkage, and the consequent volumetric changes, due to γ’ precipitation in the weld metals could

have contributed to excessive tensile loading of the crack susceptible HAZ and aided intergranular liquation cracking.

The newly developed FUMT treatment procedure, coupled with the selection of an appropriate type of filler alloy, is effective in reducing HAZ intergranular cracking both during laser-arc hybrid welding and during post-weld heat treatment (PWHT) of the laser-arc hybrid welded IN 738 superalloy.

1.5 Thesis Organization

This dissertation consists of six chapters, organized as follows.

- Chapter 1 contains background information about this research, the research problem, objective and methodology, and a summary of major findings.

- Chapter 2 is the literature review, which contains information on the physical metallurgy of IN 738 superalloy and a review of various welding technologies, including laser-arc hybrid welding. Various methods of weldability testing and the defects and problems associated with fusion welding of materials are discussed. The last part of the literature review contains the scope of this research.

- Chapter 3 provides detailed description of the experimental methods and equipment used for this research. The specifications for all processes and equipment are provided in this chapter. The chemical compositions of as-received IN 738 superalloy and those of the welding filler alloys are also supplied.

- Chapter 4 is divided into sections containing experimental results and discussion of the results. In section 4.1 the microstructural characteristics of a typical laser-arc

hybrid welded IN 738 superalloy is discussed. A discussion on the development of an effective and industrially feasible thermal treatment procedure for the alloy is presented in section 4.2. The role of filler alloys of various chemical compositions on laser-arc hybrid weldability of the alloy is discussed in section 4.3, while section 4.4 focussed mainly on post-weld heat treatment behaviour.

- Chapter 5 contains an expanded summary of the major findings and conclusions. The result from the entire work is summarized in a single sequence but according the sections presented in chapter 4.

- Chapter 6 provides some suggestions for future work.

In addition, references and research contributions are provided at the end of the thesis.

CHAPTER 2

LITERATURE REVIEW

2.1 Introduction

This review of literature consists of three major parts. An overview of the physical metallurgy of IN 738 superalloy is presented first (Section 2.2). This is followed by a discussion of the various fusion welding techniques and problems associated with fusion welding, especially in the joining of complex multi-component materials such as nickel-base superalloys (Section 2.3). Some weldability testing procedures are also discussed in Section 2.3. In the last part of this review (Section 2.4), laser-arc hybrid welding is presented, which is a relatively new and emerging joining technology that possesses several advantages over the other traditional welding technologies. Laser beam welding and arc welding processes, including their benefits and shortcomings, are discussed in some detail. The synergistic effect of combining laser welding and arc welding in laser-arc hybrid welding is discussed. The advantages and current applications of laser-arc hybrid welding are identified and discussed. This review of literature is followed by the scope and objective of the present study.

2.2 A Review of the Physical Metallurgy of IN 738 Superalloy

IN 738 is a remarkable nickel-base superalloy, which is both solid solution and precipitation strengthened, and usually selected for applications that require good high temperature mechanical, corrosion and oxidation properties. It has a face-centered cubic (fcc) austenitic solid-solution as the matrix with an intermetallic compound phase, usually known as gamma prime (γ') particles [19]. The alloy was designed to combine the strength of IN 713C, which possesses excellent high temperature strength, with the

oxidation and sulfidation resistance of Udimet 500. Like IN 713C, IN 738 also derives its high temperature strength mainly from the precipitation of the ordered $L1_2$ intermetallic Ni_3(Al, Ti), γ', phase. Its excellent corrosion and creep resistance allow it to be used at temperatures up to approximately 980^{o}C. Two different versions of the alloy exist in the cast form depending on the carbon content. The low carbon version (C≈0.09 – 0.13 wt%) is designated as IN 738LC which also has a lower Zr content to improve the alloy's castability in large sections, while the high carbon (C≈0.15 – 0.20wt%) is designated as IN 738C [20].

IN 738 superalloy is vacuum melted and vacuum cast and was developed at the Paul D. Merica research laboratory [21]. To partially eliminate the microporosity formed, and its detrimental effect, during solidification of the investment cast material hot isostatic pressure (HIP) is usually applied to the cast alloy in an argon atmosphere at high temperature. After casting, the alloy is usually subjected to a standard solution heat treatment (SHT) at 1120^{o}C for 2hrs, air-cooled, followed by a standard aging treatment at 845^{o}C for 24hrs, then air-cooled. Other researchers have also discussed the physical metallurgy of the alloy in some detail [22-24]. The effect of alloying elements and the various microconstituents present in the alloy are discussed next.

2.2.1 Alloying Elements and their Effect on Microstructure

In IN 738 superalloy, the alloying elements and their concentration play a significant role in the alloy`s microstructure and strength. The compositions of both IN 738LC and IN 738C are given in Table 2-1 [20]. The atomic diameter of nickel is about 0.2491 nm [25] and the diameters of the alloying elements differ from this by about 0 to 18%, with the difference of atomic diameter of niobium being the highest (18%). Co, Cr, Fe, Mo, W

Table 2 - 1: Chemical composition of cast IN 738C and IN 738LC

Element	IN 738C (wt%)	IN 738LC (wt%)
Carbon	0.17	0.11
Cobalt	8.5	8.5
Chromium	16.00	16.00
Molybdenum	1.75	1.75
Tungsten	2.60	2.60
Tantalum	1.75	1.75
Niobium	0.90	0.90
Aluminum	3.40	3.40
Titanium	3.40	3.40
Boron	0.01	0.01
Zirconium	0.1	0.05
Iron	LAP*	LAP*
Manganese	LAP	`LAP
Silicon	LAP	LAP
Sulphur	LAP	LAP
Nickel	Balance (61)	Balance (61)

*Low as possible

and Ta are solid solution strengtheners, W, Ta, Ti, Mo, Nb and Cr are carbide formers and Al and Ti are the main Ni_3(Al, Ti), γ', phase forming elements. Co raises the solvus temperature of γ' while Cr lowers it and the addition of Al, Cr and Ta provides resistance to high temperature oxidation. Enhancement of creep rupture properties is achieved by the presence of B and Zr [19]. Apart from the γ' phase in IN 738, several second phase particles are also present in the alloy as a result of its multi-component nature and the metallurgical reactions that are possible in the alloy, depending on the processing route and the actual composition [23]. Such phases include carbides, sulphocarbides and borides, and other solidification products [26]. The microstructure of the cast alloy will be discussed next.

2.2.2 Microstructure of the Cast Alloy

Cast IN 738 superalloy consists of: the gamma (γ) matrix, the gamma prime (γ') phase, carbides, sulphocabides and borides, and other solidification products.

2.2.2.1 The Gamma (γ) Matrix

The γ phase is a continuous matrix of nickel-base austenite. It has an fcc crystal structure [27] and contains a significant amount of solid-solution strengthening elements such as Co, Cr, Mo, W, Al and Ti. Their atomic diameters differ from Ni by 1 – 18% and normally occupy substitutional atomic positions in Ni crystal producing a distorted lattice with spherical symmetrical strain field. This strain field can interact with the strain field around a dislocation, producing an elastic dislocation-solute atom interaction and provide solid-solution strengthening. Al, in addition to being a precipitation strengthener, is a potential solid-solution strengthener. W, Mo and Cr are also strong solid-solution strengtheners. Above $0.6T_m$ (T_m is the melting temperature of the alloy in Kelvin scale),

which is the range of high temperature creep, creep strength is diffusion dependent and the slow-diffusing elements Mo and W are the most beneficial for reducing high-temperature creep. Also, Co, by decreasing stacking fault energy of nickel, which causes dissociation of dislocations into partial dislocations, makes cross-slip more difficult and thereby increases high-temperature stability [25]. The matrix has a high endurance for severe temperatures as a result of the high tolerance of nickel for alloying without phase instability owing to its nearly filled third electron shell [28]. Cr in the γ matrix, depending upon the amount present, forms Cr_2O_3-rich protective scales having low cation vacancy content, thereby restricting the diffusion rate of metallic elements outward, and that of oxygen, nitrogen, sulphur and other aggressive atmospheric elements inward. There is also an additional tendency to form Al_2O_3-rich scales with exceptional resistance to oxidation [28].

2.2.2.2 The Gamma Prime (γ') phase

The γ' phase is an intermetallic fcc phase having a basic composition Ni_3(Al, Ti). It is the principal high-temperature strengthening phase of precipitation-hardened superalloys and it is usually coherent with the austenitic γ matrix. γ' phase generally forms by the reaction of Al and Ti with Ni. It displays the primitive cubic, $L1_2$, crystal structure with Al (and/or Ti) atoms at the cube corners and Ni atoms at the centres of the faces [27]. A typical unit cell of the $L1_2$ crystal structure of the γ' phase is shown in Figure 2-1 [29]. Other elements, such as Nb, Ta and Cr, also enter γ' [30]. It has been suggested that the composition of γ' in IN 738 is [31]:

$$(Ni_{.922}Co_{.058}Cr_{.017}Mo_{.002}W_{.002})(Al_{.518}Ti_{.352}Ta_{.046}Nb_{.410}W_{.014}Cr_{.020})$$

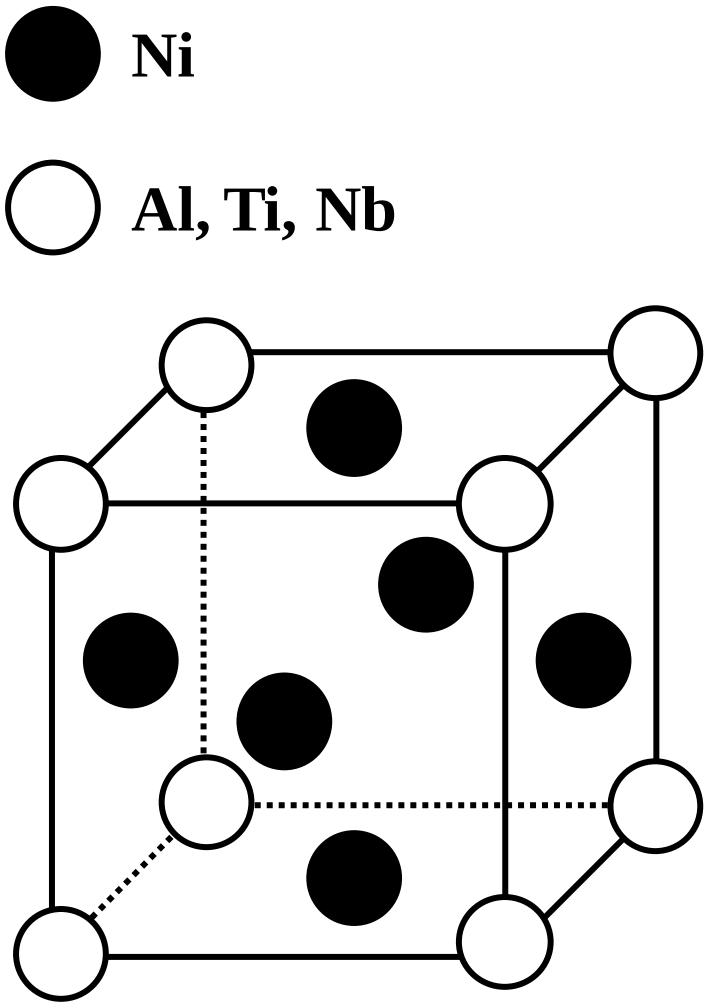

Figure 2 - 1: Unit cell illustrating $L1_2$ ordered FCC lattice of γ' phase

The mismatch between γ and γ' unit cells determines the γ' morphology. γ' occurs as spheres at 0-0.2% lattice mismatch, becomes cubic at mismatches around 0.5-1.0% and then becomes plate shape at mismatches above 1.25% [32]. The γ' phase, which nucleates homogeneously with low surface energy and has extraordinary long-term stability, can be precipitated in the austenitic γ matrix by precipitation hardening heat-treatments [25].

Due to the long range order exhibited by γ', anti-phase boundary (APB) faults occur generally in γ'-strengthened nickel-base alloys whenever shear strain is applied to the alloy, consequently resulting in APB strengthening by dislocation- γ' precipitate interaction. Also, the degree of order in Ni_3(Al, Ti) increases with temperature [25], therefore, IN 738 with a high volume fraction of γ' possesses a higher strength at higher temperatures compared to γ'-lean alloys.

Gamma Prime (γ') Precipitation Hardening Theories

The total strength of a polycrystalline material includes contributions from the intrinsic strength of the lattice, solid solution strengthening, hardening by grain size and precipitation hardening [33]. When the critically resolved shear stress (CRSS) of a crystal is exceeded under the influence of a load, slip is activated and dislocations glide freely through the crystal. Precipitation hardening occurs when the motion of a gliding dislocation is impeded by a secondary phase, such as the ordered $L1_2$ Ni_3(Al,Ti) intermetallic γ' phase in nickel base superalloys. Among many existing theories of dislocation-particle interaction, the two major mechanisms that have been used to describe precipitation strengthening in several materials, especially nickel-base and iron- and cobalt-rich alloys, are the looping or by-pass (Orowan) and the precipitate shearing

or cutting (order hardening) mechanisms [34-36]. The Orowan mechanism is based on the premise that the particles are strong enough to withstand the local stress exerted on them by a dislocation without shear or fracture [33, 37]. The dislocation bypasses the particles, leaving dislocation loops around them. One of the simplest forms of the Orowan mechanism is expressed as

$$\Delta\tau = \frac{G_m b}{L} \ldots\ldots\ldots\ldots\ldots\ldots (2-1)$$

where G_m is the shear modulus of the matrix, b is the Burger's vector and L is the inter-particle spacing. Results from both theoretical and experimental studies have suggested that the Orowan mechanism is operative only above a critical particle diameter, which was calculated to be as low as 120 nm and 270 nm for γ' volume fractions of 22% and 51%, respectively, in nickel-base Nimonic 105 superalloy [34]. It is conceivable that precipitation hardening in nickel alloys with γ' precipitate sizes of only a few nanometers may preclude the dominance of Orowan mechanism.

In order hardening, a matrix dislocation shears an ordered precipitate, creating an anti-phase boundary (APB) on the slip plane of the precipitate. The energy per unit area on the slip plane, γ_{apb} (APB energy) represents the force per unit length opposing the glide of a dislocation as it penetrates the particle. The dislocations causing plastic deformation (with b = a<110>/2) travel in pairs during shearing. The passage of the trailing dislocation through the particle restores perfect order on the {111} slip plane on which an APB was created by the leading dislocation. The CRSS for the case of a single dislocation interacting with small particles, has been expressed as [36, 38].

$$\tau_c = \frac{\gamma_{apb}}{b}\left[\frac{3\pi^2\gamma_{apb} f < r >}{32\Gamma}\right]^{1/2} \quad \text{.....(2-2)}$$

where b is the burger's vector, f is the volume fraction of the precipitate, <r> is the average particle radius and Γ is a parameter used to describe the character of the dislocation. More complex expressions for CRSS, which account for the influence of the trailing dislocation, have been derived [36]. More importantly, experimental data on yield strength or CRSS as a function of aging time and/or precipitate size in several single crystal and polycrystalline nickel-base alloys are available in the literature [36, 38, 39-41]. Equation 2-2 suggests that, for an alloy strengthened by a distribution of small spherical particles, the CRSS should increase with increase in f and <r> within the particle size range for which the equation is valid. According to the data available for the Ni-Al system [39, 42], order hardening appears to be the most likely dominant dislocation-particle interaction mechanism when the particles size is only a few nanometers.

2.2.2.3 Gamma-Gamma Prime (γ-γ') Eutectic

γ-γ' eutectic forms as a result of supersaturation of interdendritic liquid with γ'-forming elements, caused by continual solute enrichment, at temperatures approaching the equilibrium solidus. The γ-γ' eutectic mainly consists of γ' phase separated by thin lamellae of γ phase. In IN 738, the temperature of γ-γ' eutectic reaction occurring towards the end of solidification process has been reported to be around 1230^{o}C [43] and 1198^{o}C [44]. Metallographic examination of directionally solidified IN 738 from above the liquidus temperature to different on-cooling temperatures, followed by water

quenching, has shown that γ-γ' eutectic reaction in the alloy occurs over a range of temperatures [45].

2.2.2.4 Carbides

MC, $M_{23}C_6$ and M_6C type carbides are common in nickel-base superalloys. [1]. The most common carbide in IN 738 is the MC type carbide. MC carbides usually form during solidification, when the level of carbon concentration is above 0.05% [46], by the reaction of carbon with elements such as Ti, Ta and Nb. They can be monocarbides or contain several carbide forming elements with the general formula "MC", where "M" stands for metallic elements such as Ti, Ta, Nb or W [25]. MC carbides usually take a coarse random cubic or irregular morphology. They occur as discrete particles distributed heterogeneously throughout the alloy, both in intergranular and intragranular positions, usually interdendritically, with little or no orientation relationship with the matrix [1]. Primary MC carbides are dense and have fcc crystal structure with relatively high thermal stability and strength. The chemical formula of MC carbides has been suggested to be: $(Ti_{.5}Ta_{.2}Nb_{.2}W_{.04}Mo_{.03}Cr_{.02})C$ [31] and their size can range from 1 to 100μm.

During heat treatment and service, MC carbides tend to decompose to produce other carbides such as $M_{23}C_6$ and/or M_6C through reactions such as: $MC + \gamma \leftrightarrow M_{23}C_6 + \gamma'$ and $MC + \gamma \leftrightarrow M_6C + \gamma'$. In $M_{23}C_6$ carbides, "M" is usually Cr, but it can be replaced by Fe, and to a smaller extent by W, Mo or Co. They form during lower-temperature heat treatments and during service in the temperature range 760 to 980^0C and precipitate on the grain boundaries with a complex cubic structure [25]. They are usually irregular discontinuous blocky particles, although plates and regular geometric forms have been

also observed [1]. $M_{23}C_6$ carbides can also precipitate from soluble carbon residual in the matrix when cast ingot cools through its solvus range (1000^oC – 1050^oC). M_6C carbides form at temperatures in the range of 815 to 980^oC and have a complex cubic structure. They are similar to the $M_{23}C_6$ carbides and form when the Mo and/or W content are more than 6 to 8 at %.

Grain boundary carbides, when properly formed, have positive influence on the grain boundary properties. A chain of discrete globular $M_{23}C_6$ carbides optimizes creep rupture life by preventing grain boundary sliding at higher temperatures while concurrently providing sufficient ductility for stress relaxation to occur without premature failure [19]. Contrarily, carbides precipitation as a continuous grain-boundary film severely degrades mechanical properties. Also, carbides can tie up certain elements that would otherwise promote phase instability during service.

Apart from MC type carbides and γ-γ' eutectic, other secondary phases including sulphocarbides, borides along with other terminal solidification microconstituents are also found in IN 738 superalloy.

2.2.2.5 Sulphocarbides

Though sulphur is usually present in nickel-base superalloys in trace amounts, it has been found to strongly segregate to grain boundaries resulting in severe grain boundary segregation [47-49]. However, the presence of elements such as Ti, Zr, Nb, Hf, and La which have low solubilities in the matrix and high affinity for sulphur has been found to mitigate this effect through the formation of a variety of sulphur-rich intermetallic phases [50] referred to as sulphocarbides.

2.2.2.6 Borides and other Terminal Solidification Microconstituents

Borides are hard refractory particles that are observed at grain boundaries but their volume fraction is significantly smaller than that of carbides. Boron, generally present to the extent of 50 to 500 ppm, segregates at grain boundaries to form borides. Borides commonly found in superalloys are of the type M_3B_2, with a tetragonal unit cell [30]. It has been found recently that, under certain heat-treatment conditions, M_5B_3 borides also form in superalloys [51].

Hoffelner et al [26], by X-ray diffraction analysis, identified M_3B_2 type borides and M_2SC sulphocarbides in IN 738 after heat treatments. Ojo et al [22] identified some intermetallic phases precipitated very close to γ-γ' eutectic islands during solidification of cast IN 738. These phases, which were first observed by Ojo et al and termed as terminal solidification products, were identified by EDS analysis as Cr-Mo rich particles, Ni-Zr rich particles and Ni-Ti rich particles. TEM diffraction pattern analysis suggested that the Cr-Mo rich particles were M_3B_2 type borides with tetragonal crystal structure. The Ni-Zr rich and Ni-Ti rich particles were suggested to be based on Ni_5Zr and Ni_3Ti respectively. Egbewande et al [23] also observed the formation of sulphur and carbon rich Ti-Zr-Nb phase close to γ-γ' eutectic, and other terminal solidification constituents.

2.3 Fusion Welding Processes and Welding-Related Problems

Welding is one of the most important processes in the fabrication and repair of parts and /or assemblies including appliances, building structures, machines, and automotive, aerospace components and so on. Welding has been described as a process for joining metals and other materials by applying heat, pressure or both, with or without filler metal, to produce a localized union through fusion or recrystallization across the interface [52].

Welding can be generally classified as fusion welding and solid state joining processes. Since only laser-arc hybrid fusion welding process was used in this study only fusion welding processes are described here.

2.3.1 Fusion welding Techniques

In fusion welding, a metallurgical bond/joint is produced between/among components through melting and resolidification of either base alloys of the components to be joined or base alloys plus filler metal [30]. In cases where a filler material is required, the filler could have either the same nominal composition as the base alloy or a composition compatible with the chemistry of the components being joined both environmentally and mechanically. Melting during fusion welding is achieved by the use of a heat source which may be provided by a chemical flame, an arc, a laser or an electron beam. The various fusion welding processes are classified into three major categories based on the type and power density of the heat source. These include:

1. Gas welding
2. Arc welding
3. High energy beam welding

2.3.1.1 Gas Welding

In gas welding, metals are joined by heating them with a flame caused by the reaction between a fuel gas and oxygen. Oxyacetylene welding is the most commonly used gas welding process due to its high flame temperature [53]. A schematic diagram of the process is provided in Figure 2-2 [53]. The oxyacetylene welding process equipment is simple, portable and inexpensive, making it convenient for maintenance and repair applications. However, the very low welding speed and the rather high total heat input

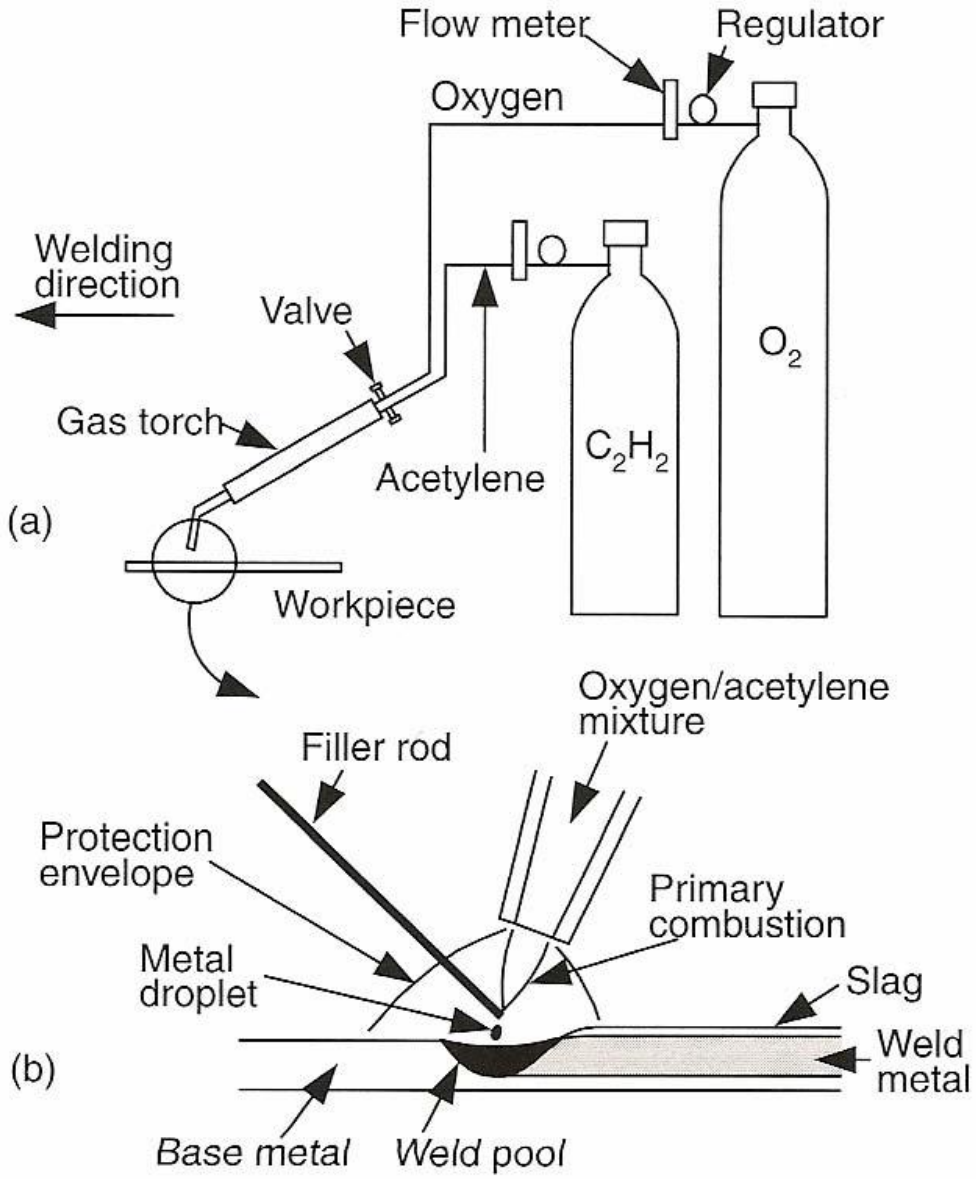

Figure 2 - 2: Oxyacetylene welding: a) overall process, b) welding area enlarged

Source: *S. Kuo, Welding Metallurgy, 2nd ed., John Wiley & Sons Inc., Hoboken, 2003. Reprinted with permission from Global Rights Dept., John Wiley and Sons, Inc. (5 June, 2013).*

per unit length of the weld due to low power density result in large heat-affected zones (HAZ) and severe distortion. Oxyacetylene welding process is not recommended for welding reactive metals such as titanium and zirconium because of its limited protection power.

2.3.1.2 Arc Welding

Arc welding uses an arc, struck between an electrode and the workpiece, to generate heat that melts the filler (which could sometimes be the electrode) and the base metal. A molten pool is produced under the protection of an inert gas blanket. The pool solidifies as the heat source retreats from the area, and a solidified weld nugget is formed along with a heat-affected zone (HAZ). The HAZ extends from the interface of the previously molten metal to a distance in the metal being joined where the temperature reached in the welding process becomes sufficiently low that no metallurgical changes occur. Arc welding processes include [53]: shielded metal arc welding (SMAW), gas tungsten arc welding (GTAW), plasma arc welding (PAW), gas metal arc welding (GMAW), flux cored arc welding (FCAW), and submerged arc welding (SAW). Arc welding processes are discussed further in section 2.4.

2.3.1.3 High Energy Beam Welding

The two key high-energy-beam welding processes are electron beam welding and laser beam welding. They possess very high power density, which results from the concentration of high energy beam in to a very small beam diameter.

Electron beam welding: Electron beam welding is a process that melts and joins metals by bombarding the joint to be welded with an intense beam of high-voltage electrons

[53]. The process converts part of the kinetic energy of the electrons to thermal energy as the electrons impact and penetrate into the workpiece, which causes the weld-seam interface to melt and produce the desired weld joint coalescence. Figure 2-3 [53] shows a schematic of the electron beam welding process. The cathode of the electron beam gun is a negatively charged filament, which emits electrons when heated up to its thermionic emission temperature. The electrons are accelerated by the electric field between a negatively charged bias and the anode, passing through the hole in the anode, and then focused by an electromagnetic coil to a point at the workpiece surface. Typical beam currents and accelerating voltage vary over the ranges 50-1000mA and 30-175kV, respectively. A vapour hole (referred to as key hole) can form when a metal is vaporized by an electron beam of very high intensity. The electron beam can be focused to diameters in the range 0.3-0.8mm, resulting in power density as high as $10^{10}W/m^2$. This very high power density makes it possible to vaporize the material and produce deep penetrating keyhole and hence weld, which is a notable advantage in welding thick workpieces. The total heat input per unit length of the weld in electron beam welding is much lower than that of arc welding. Joints that require multiple-pass arc welding can be welded in a single pass at a higher welding speed with electron beam. This results in a very narrow heat-affected zone and little distortion. Electron beam welding can also be used for joining reactive and refractory metals in vacuum, and also some dissimilar metals. A limitation of the process is the high installation and operation cost due to the requirements of high vacuum (10^{-3}-10^{-6} torr) and X-ray shielding. The process is also time-consuming due to the long set-up and evacuation time.

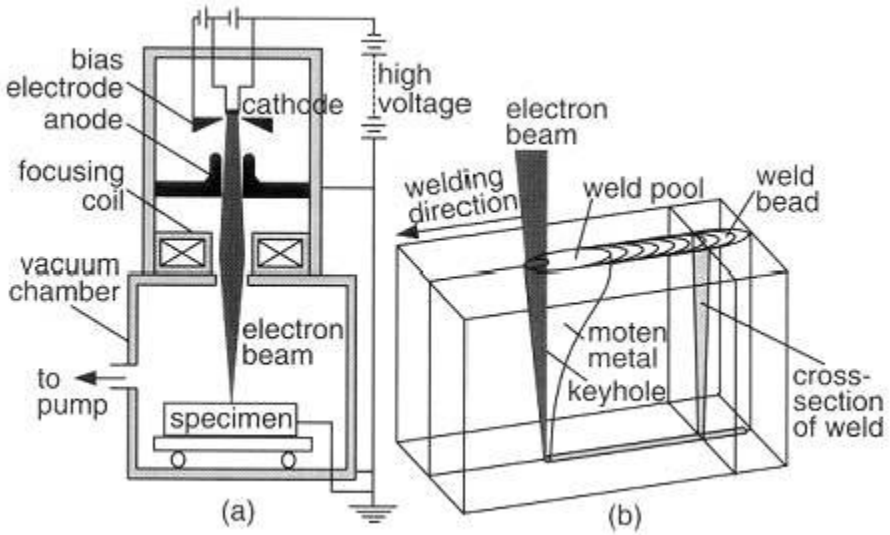

Figure 2 - 3: Electron Beam Welding: a) process; b) keyhole

Source: *S. Kuo, Welding Metallurgy, 2nd ed., John Wiley & Sons Inc., Hoboken, 2003. Reprinted with permission from Global Rights Dept., John Wiley and Sons, Inc. (5 June, 2013).*

Certain weldability problems occur during the application of fusion welding processes in the joining of various materials. These weldability problems are discussed next. Laser beam welding is discussed in details in section 2.4.

2.3.2 Weldability Problems in Fusion Welding

Problems associated with fusion welding processes are usually in the form of weld defects and cracking. A general description of weld defects and the distribution of residual stresses during welding will be presented first, followed by a discussion on two major types of cracking that are common to fusion welding processes.

2.3.2.1 Weld Defects and Discontinuities in Fusion Welding

Weld defects include cracks and fissures, gas porosities, inclusions, incomplete fusion and others. Cracks and fissures refer to discontinuities that are produced by local rupture. The general types of cracks include: (a) transverse cracks in the base metal perpendicular to the welding direction; (b) longitudinal cracks in the base metal parallel to the welding direction; (c) microcracks (microfissures) or macrocracks in the weld metal; (d) centerline longitudinal weld-metal cracks; (e) crater cracks; and (f) start cracks or bridging cracks. Transverse cracks usually result from external contamination or a base metal with poor weldability. Longitudinal cracks are caused by the combination of a strong weld metal and weak, low-ductility base metal. Weld-metal microfissuring can result from contamination or impurities in the weld metal that lower weldability of the metal. Centreline longitudinal cracking is caused by concave beads or a very deep, narrow weld bead. Crater cracking occurs when the arc is extinguished over a relatively large weld pool; and the resulting concave crater is prone to shrinkage cracking. Bridging cracks occur in highly stressed joints where good penetration is not achieved at the arc

initiation point. Reduction in base-metal cracking can be achieved by reducing heat input and depositing small beads, which result in lower residual stresses.

Gas porosities describe gas pockets or voids in the weld metal. Typical causes of gas porosity include improper shielding, moisture, incorrect amperage or a long arc length. Inclusions are usually slag, oxides, or other non-metallic solids entrapped in the weld metal between adjacent beads or between the weld and the parent metal. Gas-metal and slag-metal reactions can produce gas porosity and inclusions, respectively, in the weld metal and affect the weld metal properties.

Incomplete fusion can be caused by incomplete coalescence of some portion of the filler metal with the base metal. It can also feature between weld beads in case of multi-pass welds. It is a two dimensional flaw that occurs when insufficient heat is absorbed by the underlying metal from the weld, causing incomplete melting at the interfaces of the weld and the base metal after successive passes. Incomplete fusion is characterized by discontinuities which are usually elongated in the direction of welding with either sharp or rounded edges, depending on the conditions of formation. Lack of penetration is also a weld defect, caused by incorrect welding technique or by improper root gap, which occurs when the weld metal has not penetrated to the bottom of the weld joint. Other weld defects include (i) undercut: a groove melted into the base metal adjacent to the toe, cap or root of the weld metal and left unfilled by the weld metal, which act as a stress raiser and cause fatigue problems; (ii) Overlap: a protrusion of the weld metal beyond the toe, face or root of the weld; (iii) shrinkage voids: a cavity-type imperfection that forms by shrinkage during solidification; (iv) Arc Strikes: imperfections resulting from localized remelting of metal surface, caused by inadvertent contact between an electrode

and the metal surface; (v) underfill: a depression on the face of the weld or root surface extending below the surface of the adjacent base metal. Some of the various weld defects and discontinuities are schematically represented in Figures 2-4 to 2-7 [54].

2.3.2.2 Distribution of Stresses Generated During Fusion Welding

A relationship exists between the temperature reached during welding and the mechanical behaviour of different regions of the welded joint. The thermal cycling experienced by the material usually results in thermal stresses being generated within both the fusion and heat-affected (HAZ) zones of fusion welds. Consequently, residual stresses and distortions of different magnitudes are experienced by different regions in the vicinity of the weld. This can be traced to the fact that different sections of the material in a weld experience different rates of expansion and contraction due to the temperature dependence of the section's elastic modulus and yield strength [55].

The changes in temperature and the resulting stresses during a bead-on-plate weld of a thin plate, made along the x-axis, are schematically represented by figure 2-8 [52, 56]. Figure 2-8 (b) shows the temperature gradients along several sections (A-A, B-B, C-C and D-D) through the weld bead path. Figure 2-8 (c) shows the distribution of normal stress in the x-direction. Ahead of the welding arc (section A-A), the slope of the temperature gradient across the weld (along y) is almost zero, and the corresponding stresses are also almost zero. Along section B-B, where the metal is molten as indicated by the ellipse near O, the slope of the temperature gradient becomes very steep. Away from the arc (in the HAZ), the stress is compressive because the expansion of the metal surrounding the weld pool is restrained by the base metal. Due to high temperatures in these areas, a situation occurs in which stresses in these areas are as high as the yield

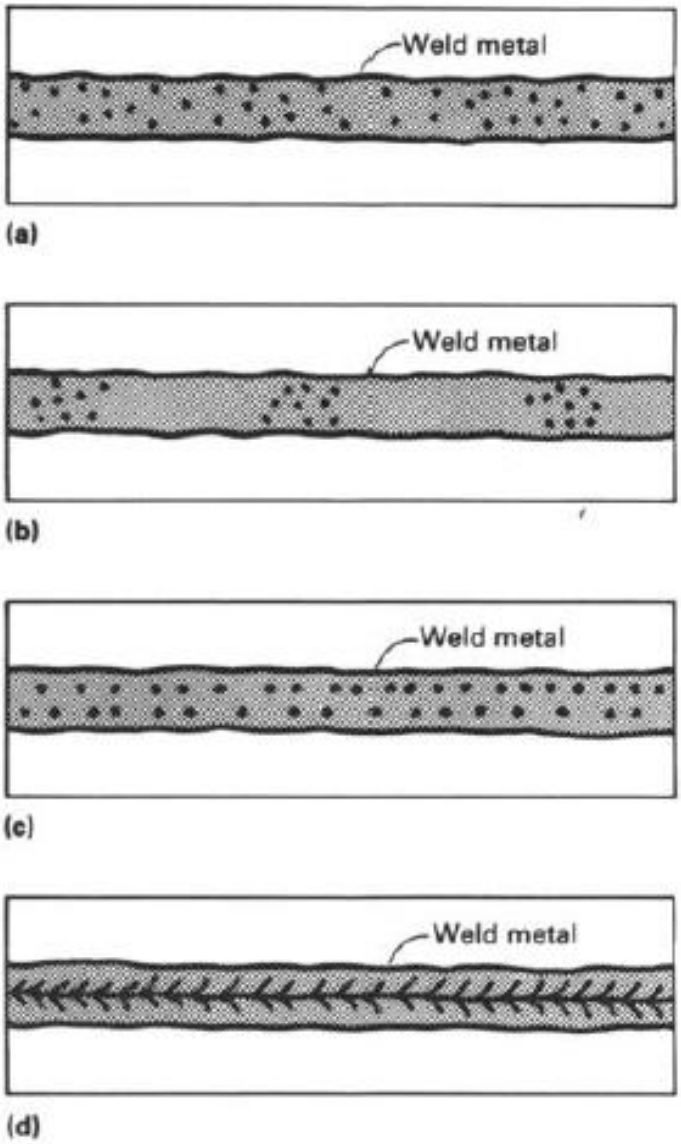

Figure 2 - 4: Types of gas porosity commonly found in weld metals (a) Uniformly scattered porosity (b) Cluster porosity (c) Linear porosity (d) Elongated porosity

Source: *ASM Handbook Volume 6: Welding, Brazing and Soldering,*

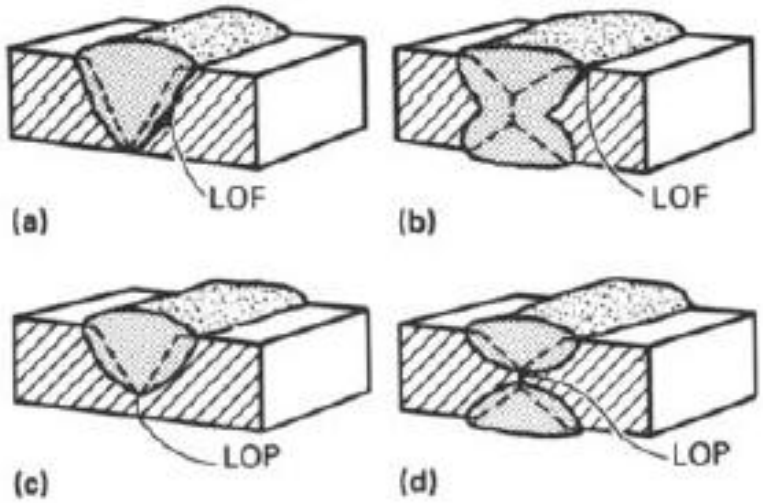

Figure 2 - 5: Lack of fusion in (a) a single-V-groove weld and (b) double-V-groove weld. Lack of penetration in (c) a single-V-groove weld and (d) a double-V-groove weld

Source: *ASM Handbook Volume 6: Welding, Brazing and Soldering,*

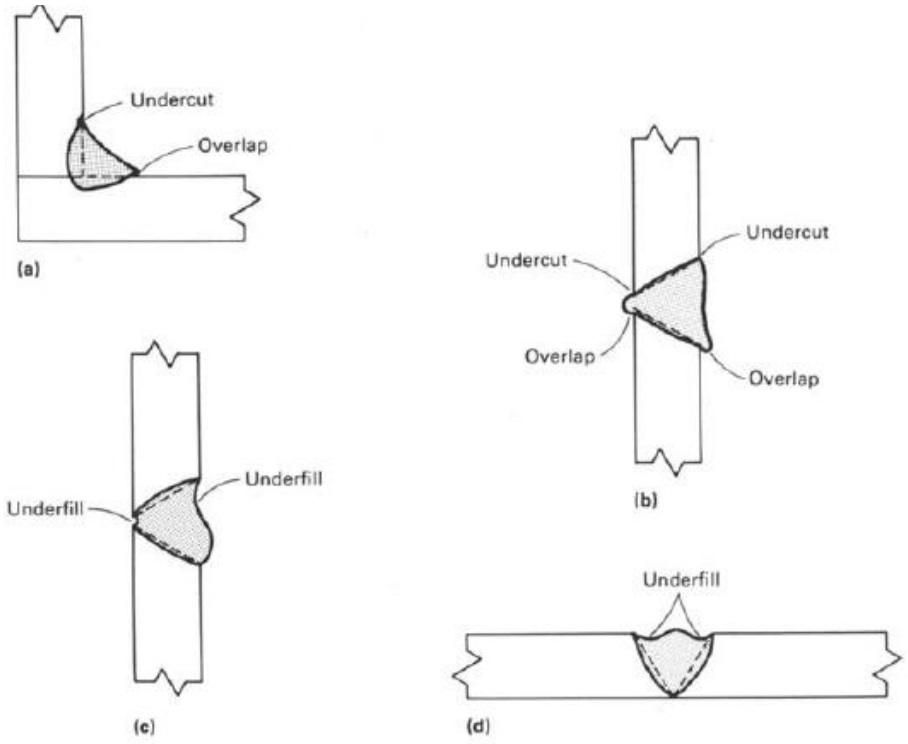

Figure 2 - 6: Weld discontinuities affecting weld shape and contour. (a) Undercut and overlapping in a fillet weld. (b) Undercut and overlapping in a groove weld. (c) and (d) Underfill in groove welds

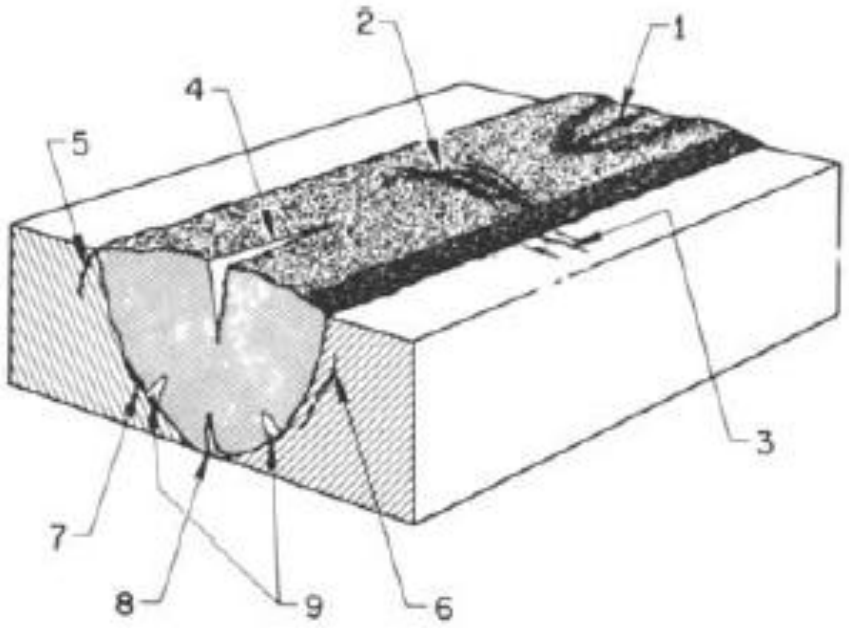

Figure 2 - 7: Identification of cracks according to location in weld and base metal. 1, crater crack in weld metal; 2, transverse crack in weld metal; 3, transverse crack in HAZ; 4, longitudinal crack in weld metal; 5, toe crack in base metal; 6, underbead crack in base metal; 7, fusion-line crack; 8, root crack in weld metal; 9, hat crack in weld metal

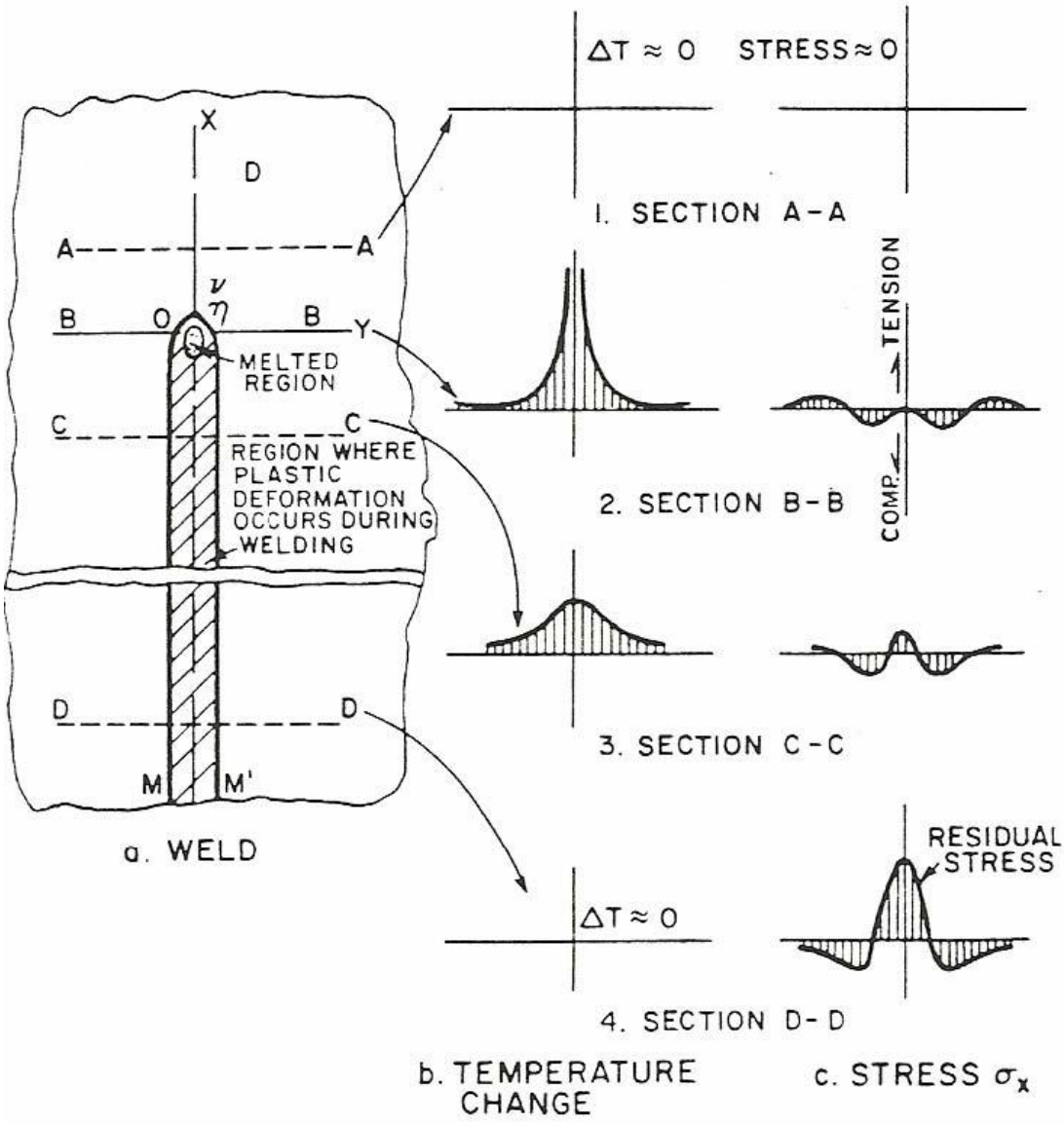

Figure 2 - 8: Schematic representation of changes in temperature and stresses during welding: (a) Weld (b) Temperature changes (c) Stress distribution

Source: *K. Masubuchi, Analysis of Welded Structures, 1980, ISBN 0-08-0261299. Reprinted with permission from the author, Koichi Masubuchi (30 June, 2013)*

stress of the base metal at the corresponding temperature. Therefore, the magnitude of compressive stress passes through a maximum with increasing distance or with decreasing temperature from the weld. However, tensile stresses occur in regions far away from the welding arc. Somewhat behind the welding arc (C-C), the temperature gradient slope becomes less steep since the weld-metal and the base-metal have cooled. As they shrink during cooling, tensile stresses are generated in regions in, and adjacent to, the weld while the stresses become compressive as the distance from the weld increases. Along section D-D, some longer distance behind the welding arc, the temperature gradient slope approaches zero again and high tensile stresses exist in, and adjacent to, the weld while compressive stresses exist in areas away from the weld.

The development of tensile stresses in the fusion and heat-affected (HAZ) zones of fusion welds during weld cooling plays an important role in weld cracking. This is a major mechanical factor that contributes significantly to cracking during conventional fusion welding of superalloys. Apart from on-cooling tensile stresses, other metallurgical factors necessary for cracking are equally important. Cracking in welded materials generally occurs in the fusion zone (solidification cracking) and/or in the heat-affected zone (HAZ Cracking). These are discussed next.

2.3.2.3 Solidification Cracking

Solidification cracking, which is observed frequently in castings and ingots, can also occur in weld deposits of fusion welds during cooling. It occurs predominantly at the weld centerline or between columnar grains that form on solidification of the weld metal. Solidification cracking is a type of cracking that occurs during the terminal stage of solidification, when the tensile stresses developed across adjacent grains exceed the

strength of the almost completely solidified weld metal [57-59]. During solidification, the weld metal tends to contract because of both solidification shrinkage and thermal contraction. Though the base metal also contracts, it does not contract as much as the weld metal because it is neither melted nor heated as much as the weld metal on the average. The contraction of the solidifying metal can therefore be hindered by the base metal, especially if the workpiece is constrained and cannot contract freely. Consequently, tensile stresses develop in the solidifying weld metal. A point is reached when the semi-solid material can no longer accommodate the thermal shrinkage strains associated with weld solidification and cooling. In order to relieve the accumulating strains, cracks form at susceptible sites such as solidification grain boundaries and interdendritic regions, which are at least partially wetted [60].

The factors affecting solidification cracking susceptibility of weld metals can be either metallurgical or mechanical in nature. Some of the metallurgical factors include:

a. The solidification temperature range: the wider the solidification (freezing) temperature range, the larger the S+L region in the weld metal or mushy zone and thus the larger the area that is weak and susceptible to solidification cracking. The larger S+L region can result from the presence of undesirable impurities such as sulphur and phosphorus, or intentionally added alloying elements [53]

b. The amount and distribution of liquid at the terminal stage of solidification: maximum crack susceptibility occurs somewhere between the composition of a pure metal and the composition of a highly alloyed metal. A pure metal is not susceptible to cracking because there is no low-melting-point eutectic present at the grain

boundary to cause solidification cracking. In highly alloyed material, on the other hand, the eutectic liquid between the grains can be abundant enough to heal incipient cracks. Somewhere in between these composition levels, however, the amount of liquid between grains can be just large enough to form a thin, continuous intergranular film to make the materials susceptible to solidification cracking but without extra liquid for healing the cracks [53].

c. The ductility of the solidifying weld metal: the less ductile a solidifying weld metal is, the more likely it will crack during solidification [53, 61]

d. The grain morphology of weld metal: Fine equiaxed grains are often less susceptible to solidification cracking than coarse columnar grains [61]. This has been attributed to the fact that fine equiaxed grains can deform to accommodate contraction strains more easily, that is, they are more ductile, than columnar grains. Liquid feeding and healing of incipient cracks can also be more effective in fine-grained material, and the grain boundary area is greater, which reduces the concentration of low-melting-point segregates at the grain boundaries.

The mechanical factors affecting solidification cracking include residual stresses and joint geometry. Though the metallurgical factors described earlier are very important for the occurrence of solidification cracking, no cracking can occur without the presence of tensile stresses acting on adjacent grains during solidification. The thermal cycle of the welding process always results in residual stresses in the weld metal. These stresses can be due to thermal contraction or solidification shrinkage or both. The severity of the stresses depends on the degree of restraint offered by the welded joint. Generally, the

thicker or stronger the plates being welded, the higher is the restraint. The higher is the restraint; greater is the magnitude of the residual stress.

The mechanism of solidification cracking can be illustrated with Figure 2-9 [62]. It is generally understood that the partitioning and rejection of alloying elements at the columnar grain boundaries and ahead of the advancing solid-liquid interface causes marked segregation. The segregates subsequently form low-melting phases or eutectics with the metal to produce highly wetting films at grain boundaries as illustrated. The alloying elements that are most-likely to segregate this way have characteristics including: low partition coefficients, ready formation of low-melting-point compounds or eutectics with the base alloy, and low wetting angle with the metal and thus possess the ability to spread along grain boundaries. As a result of these, the boundaries are weakened and cracks form under the influence of the tensile residual stresses that are generated during cooling of welds [55].

2.3.2.4 Heat-Affected Zone (HAZ) Cracking

Liquid formed on grain boundaries in the heat-affected zone (HAZ) during fusion welding can wet the grain boundaries and spread along them to form a continuous film. When this formation of continuous intergranular film is accompanied by sufficient tensile thermal stresses, cracks can form along the grain boundaries and extend into the fusion zone. Such cracking can be referred to as liquation cracking, hot cracking or microfissuring in the HAZ. Figure 2-10 [62] illustrates the formation of liquation cracks in a typical alloy. While the weld deposit is still liquid, compressive stresses tend to close up liquation cracks. However, the stresses (or strains) in the HAZ become tensile as the melt solidifies and these open up cracks [55].

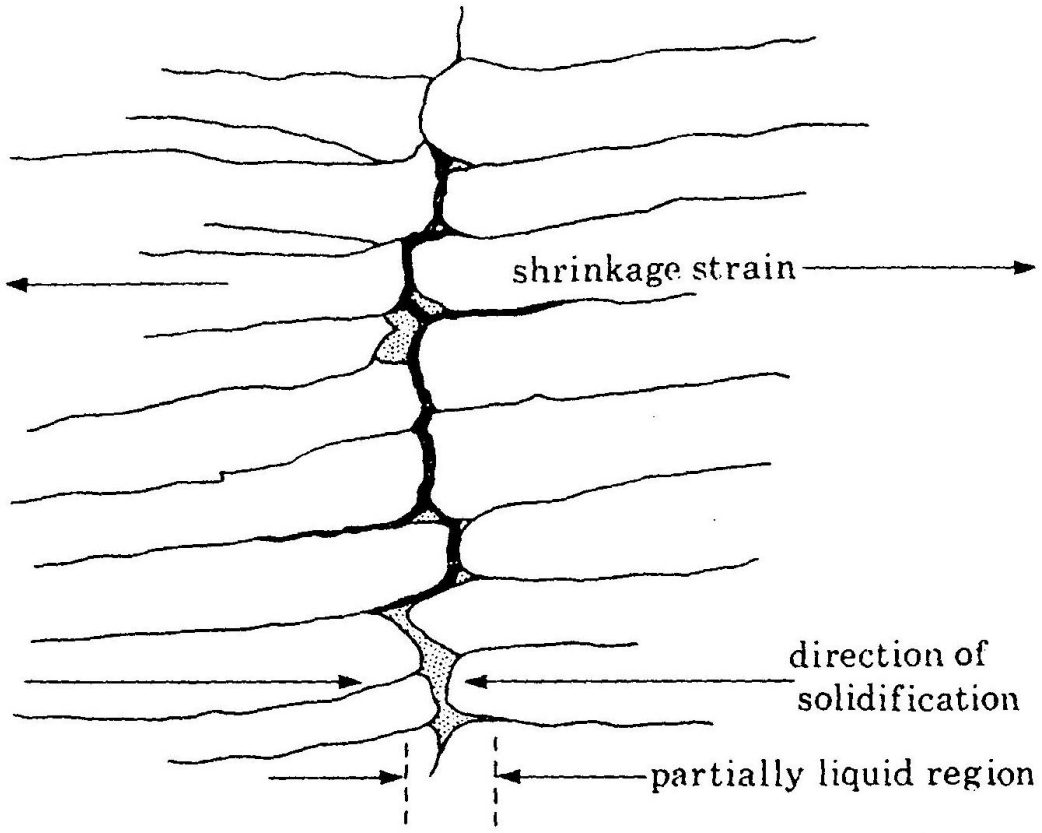

Figure 2 - 9: Schematic illustration of the mechanism of solidification cracking.

Source: *R.G. Baker, Philosophical Transactions of the Royal Society of London, Series A: Mathematical and Physical Sciences, Vol. 282 No 1307 (1976) pp.207-223. Reprinted with permission from The Royal Society (21 May, 2013)*

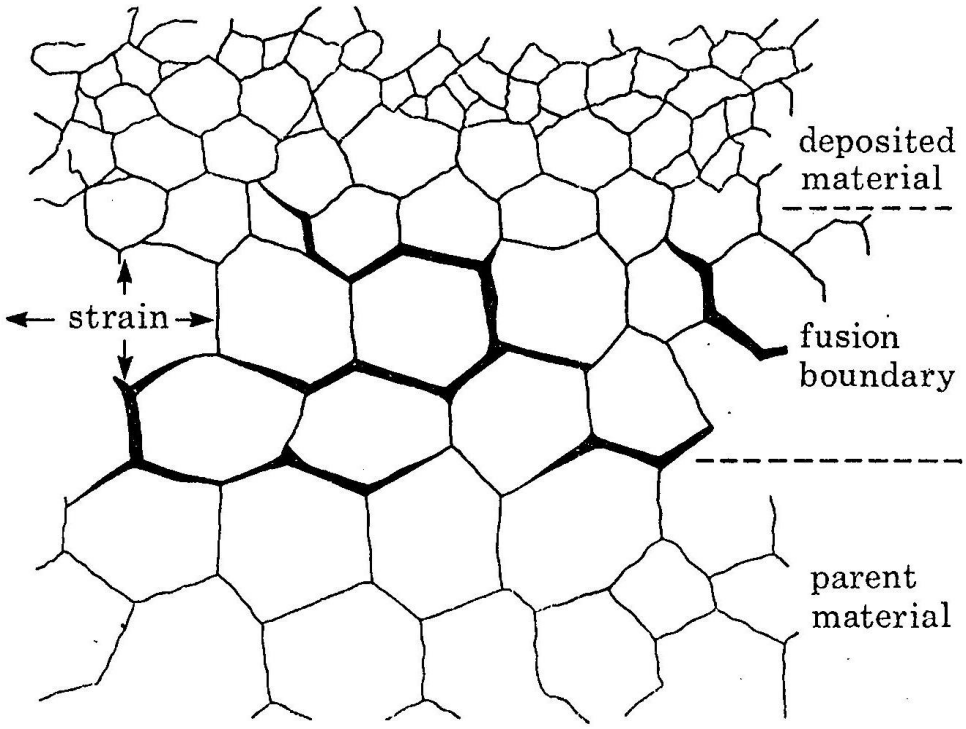

Figure 2 - 10: Schematic diagram illustrating liquation cracking

Source: *R.G. Baker, Philosophical Transactions of the Royal Society of London, Series A: Mathematical and Physical Sciences, Vol. 282 No 1307 (1976) pp.207-223. Reprinted with permission from The Royal Society (21 May, 2013)*

It is known that grain boundary liquation can occur by either supersolidus melting or by non-equilibrium sub-solidus melting. Non-equilibrium sub-solidus melting is particularly more harmful due to its ability to widen the temperature range over which a weldment remains liquid and thus increase the material's susceptibility to HAZ liquation cracking [63]. The sub-solidus melting can occur by two main mechanisms, namely:

1. Constitutional liquation of second phase particles.

2. Segregation of melting point suppressing elements on the grain boundaries during solidification and thermal processing and during pre-weld heat treatment.

2.3.2.4.1 Constitutional Liquation Mechanism

Constitutional liquation theory was first proposed and explained in the literature by Pepe and Savage in 1967, when they observed liquation of titanium sulphide particles in 18-Ni maraging steels [64]. When an alloy, having a certain volume fraction of an intermetallic particle A_xB_y at room temperature, is heated rapidly to temperatures equal to or above the eutectic transformation temperature, constitutional liquation of A_xB_y could occur if the particle survives to the eutectic temperature during heating. This theory has been subsequently used to explain non-equilibrium sub-solidus melting of second phases in different alloys during fusion welding, which is generally known to cause HAZ liquation cracking. Examples, as observed by different researchers, include the constitutional liquation of: M_3B_2 in Udimet 700 [65], Cr_7C_3 and Ti(CN) in Inconel 600 [66], TiS in 18-Ni maraging steel [64], TiC in austenitic alloy A286 [67], M_6C in Hasteloy X [65], MC Carbide and MNP Phosphides in Incoloy 903 [68], NbC and Laves phase in Inconel 718 [69], and MC Carbide in Allvac 718Plus® [70].

The Constitutional Liquation Theory

The constitutional liquation of a precipitate particle in a hypothetical binary alloy system can be illustrated by the constitutional phase diagram of figure 2-11 [64]. The alloy, of nominal composition C_o, when heated progressively from T_1 to T_4, exhibits different behavior for an infinitely slow heating rate and for an extremely rapid heating rate. At temperature T_1, the alloy of composition C_o consists of the intermetallic compound A_xB_y, distributed as a second-phase precipitate in the α solid solution. Under an equilibrium solidification condition corresponding to an infinitely slow heating rate, the solubility of B in the matrix increases as the temperature is increased. At T_2, the last remaining A_xB_y dissolves, converting the alloy to a homogeneous single phase solid solution of composition C_o. No further changes occur as the temperature further increases from T_2 to just below T_5. At T_5, which is the equilibrium solidus of the alloy, the first infinitesimal amount of liquid of composition corresponding to point c is formed. Therefore, under an equilibrium condition, the two phase alloy is gradually converted to a single phase alloy. It remains a single phase until the first melting occurs at the equilibrium solidus of the alloy.

The dissolution of A_xB_y under non-equilibrium solidification condition, which corresponds to an extremely rapid heating rate, significantly departs from that that occurs under equilibrium solidification. The disappearance of A_xB_y upon heating requires its dissociation and subsequently the accommodation of the excess component of B, which is liberated as additional solute in the surrounding matrix. The overall rate of dissolution of A_xB_y occurs at a finite rate, which may be limited by either or both of the dissociation or accommodation process step. As the heating rate is increased, a critical heating rate

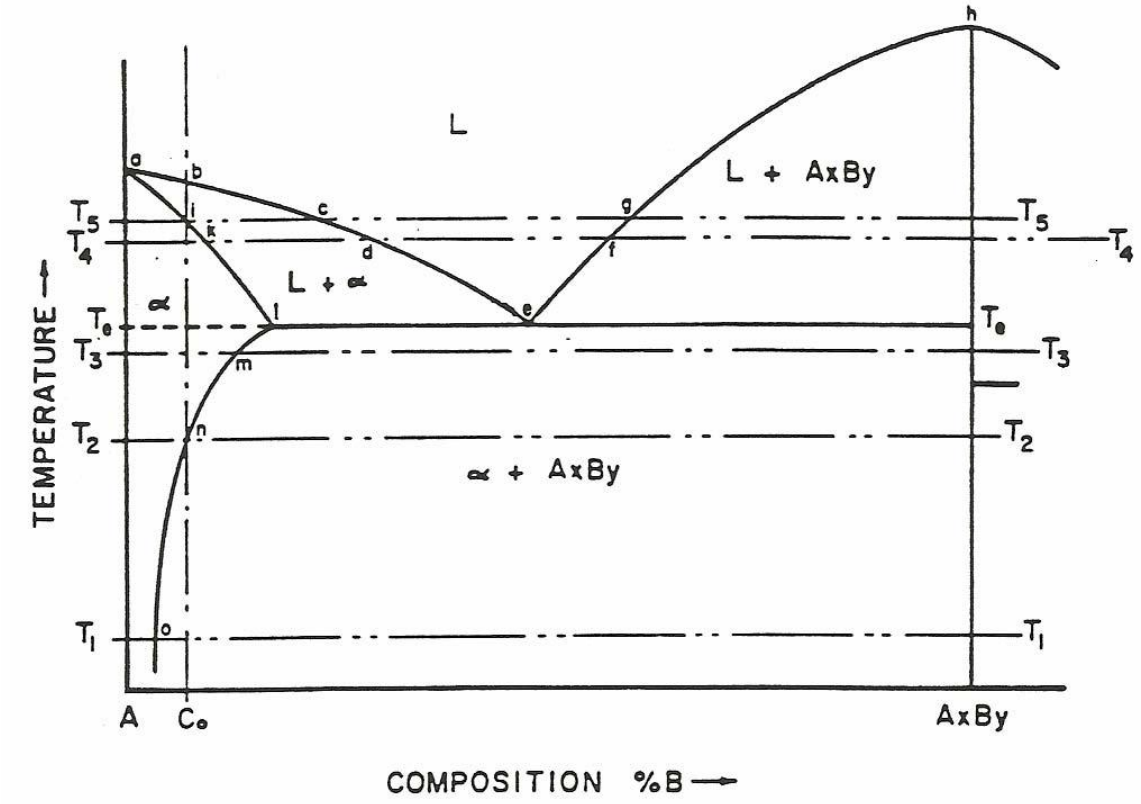

Figure 2 - 11: Schematic diagram of a portion of a hypothetical constitutional diagram for an alloy system exhibiting the behaviour necessary for constitutional liquation.

Source: *J.J. Pepe and W.F. Savage, Weld. J., Vo146 (No. 9), 1967, p 411-s. Reprinted with permission from the American Welding Society (2 August, 2013)*

will be reached above which the time required to raise the temperature to the equilibrium solidus temperature will be insufficient to achieve complete dissolution of A_xB_y. At this critical heating rate and all heating rates above it, the dissociation and diffusion process steps will occur at finite rates. The equilibrium structure of A_xB_y as a function of temperature is represented by the vertical line emanating from C_o in figure 2-11. Since the system would be striving to maintain equilibrium, any departure from an equilibrium structure due to rapid heating results in solute redistribution. For a spherical A_xB_y precipitate and a heating rate above the critical heating rate, the changes expected in the vicinity of A_xB_y during heating to temperatures of T_3, T_e and T_4, respectively, can be illustrated by figures 2-12a to 2-12c. During heating to T_3, A_xB_y dissociates since at T_3, A_xB_y is unstable with respect to a single phase solid solution of composition C_o. A_xB_y shrinks somewhat from its original volume to a smaller volume as represented by dashed and solid circles, respectively, in figure 2-12a. The B atoms liberated diffuse into the adjacent α matrix. However, figure 2-11 shows that A_xB_y must be in contact with the matrix of composition m if the two phases are to co-exist. It is therefore necessary that a concentration gradient exist in the α matrix, such that a maximum concentration value, m, exists at the A_xB_y phase interface, which decreases toward the original matrix composition, o, at the interior of the α phase. In order to maintain a material balance, the area of the double cross-hatched region of figure 2-12a must be equal to the area of the single cross-hatched region. The concentration gradient slope would be dependent on:

1. The heating rate: the faster the heating rate is, the steeper the concentration gradient

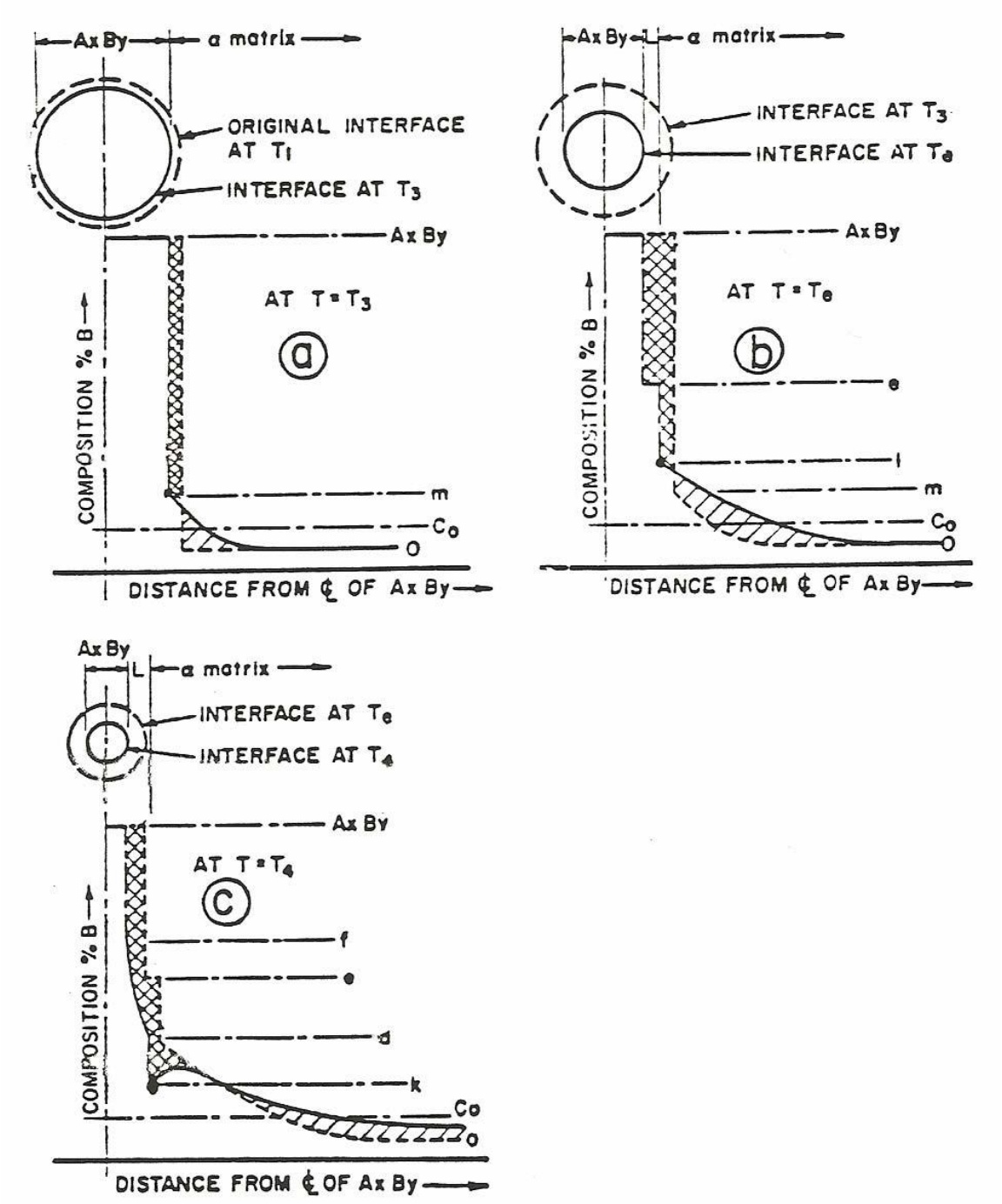

Figure 2 - 12: Schematic representation of the concentration gradients at various temperatures during formation of constitutional liquation

Source: *J.J. Pepe and W.F. Savage, Weld. J., Vo146 (No. 9), 1967, p 411-s. Reprinted with permission from the American Welding Society (2 August, 2013)*

2. The diffusivity of solute: the faster the diffusivity of solutes, the shallower the concentration gradient

3. The relative ease with which the solute atoms are accommodated by each successive single phase region in the diffusion couple

A_xB_y continues to dissociate during heating from T_3 to T_e, the particle size continues to decrease as represented in figure 2-12b, where the dashed and solid circles represent the location of A_xB_y interface at T_3 and T_e, respectively. At the eutectic temperature, T_e, the composition corresponding to point e permits the formation of a single phase liquid at the A_xB_y interface, thus, the undissociated portion of A_xB_y is surrounded by a liquid phase of composition e, which, in turn, is surrounded by the α matrix. Figure 2-12b shows the solute distribution in the three phases co-existing at temperature T_e. On further heating to T_4, additional time is allowed for the dissociation of A_xB_y. The expected solute distribution at T_4 is shown by figure 2-12c. Upon heating above T_e, the equilibrium solubility of α phase decreases along the solidus line "akl". Therefore at T_4, the concentration of the solute in solid solution and the liquid film in contact with one another correspond to k and d, respectively. Each particle of A_xB_y remaining undissolved at T_4 is surrounded by a liquid film of variable composition ranging from "f" at the A_xB_y interface to "d" at the matrix interface. This causes localized melting under non-equilibrium heating rates at temperatures between T_e and T_5, a phenomenon termed as constitutional liquation. Therefore, constitutional liquation occurs under rapid heating and results in the formation of solute-rich liquid pools at temperatures well below the equilibrium solidus of the alloy [64]. Interactions between these liquated regions and the

grain boundaries during fusion welding could establish a microstructure that is sensitive to intergranular liquation cracking.

2.3.2.4.2 Grain Boundary Segregation Mechanism

Grain boundary segregation is another mechanism for grain boundary liquation. It occurs by the segregation of melting point suppressant elements to grain boundaries, which reduces the melting temperature of the grain boundary material relative to the surrounding matrix. For grain boundary liquation cracking to occur by this mechanism, grain boundary segregation must take place first. Non-equilibrium sub-solidus grain boundary melting then occurs in the HAZ during welding at temperatures which are above the reduced melting temperature of the grain boundary material [63]. The effect of segregation of solutes and the close relationship between segregation and the weldability of nickel-based superalloys, where segregation was found to alter the liquid wettability of grain boundaries, has been studied [71]. The presence of solutes in the grain boundary liquid was observed to have lowered the solidification range of the liquid and contributed to HAZ microfissuring.

Grain Boundary Segregation Theory

Segregation of impurities on grain boundaries before welding can be induced by either equilibrium segregation [72-75] or non-equilibrium segregation [76-80]. Equilibrium grain boundary segregation occurs by the movement of solutes from the bulk of the alloy to grain boundaries when the material is held at a sufficiently high temperature that can promote an appreciable diffusion of solutes. The solute atoms are absorbed to reduce the interfacial free energy of the loosely packed grain boundary region. Impurity atoms can also segregate from the bulk alloy to other loosely packed sites such as free surfaces,

phase boundaries, stacking faults and precipitate/matrix interfaces. The driving force for equilibrium grain boundary segregation is a reduction in the grain boundary free energy. As the temperature of the isothermal heat treatments increases, the level of segregation decreases. Equilibrium grain boundary segregation is restricted to a few atoms layers of the grain boundary and the total amount is usually of the order of a few monolayers.

Non-equilibrium segregation occurs during cooling from the thermal treatment temperature. In addition to the equilibrium concentration of vacancies generated and distributed during elevated temperature heat treatment, some vacancy-solute complexes can also form as a result of positive binding energy between the solute atom and vacancy. The diffusion coefficient of the solute-vacancy complex exceeds that of the solute alone. During cooling to lower temperatures, supersaturation of vacancy concentration occurs in the matrix, and the grain boundaries can act as sinks for vacancies. A concentration gradient of vacancies develops near the grain boundaries and vacancies within diffusion range of the grain tend to migrate to the grain boundaries. Vacancy diffusion towards the grain boundaries tends to drag solute-vacancy complexes towards the boundaries, producing a solute-rich grain boundary region. This process is thermodynamically driven by the decrease in free energy associated with the annihilation of excess vacancies at the grain boundary sinks [81]. The degree of non-equilibrium segregation has been found to depend on the starting temperature, cooling rate, bulk concentration of solutes and the binding energy between solute atoms and vacancies [82-85]. An increase in thermal treatment temperature increases equilibrium concentration of vacancies and the degree of segregation increases. If sufficient time is not available for the diffusion of complexes to grain boundaries to occur when the cooling rate is high, the degree of segregation will be

reduced. On the other hand, if the cooling rate is very slow, causing a gradient in concentration of solute atoms between the grain boundary and the grain interior, the segregated solute atoms may diffuse back to the grain interiors, thereby eliminating segregation [71].

2.3.3 Weldability Testing

As discussed earlier, welding processes usually have effects on the properties and characteristics of materials. These characteristics include base-metal and weld metal ductility and cracking susceptibility, weld penetration and weld shape [86]. Weldability testing is used to evaluate the properties and characteristics that developed in materials during welding. Weldability tests are intended to evaluate actual service conditions through the responses of the base material to different welding conditions or simulated welding conditions. Some of the weldability testing methods are described next.

2.3.3.1 Self-Restraint Tests

These tests utilize the restraint within the specimen, without external loading, to cause cracking in the weld or base metal [86]. The specimen used for testing is designed to produce variable restraint on the weld joint, resulting in cracking. An example of self-restraint test is the Lehigh Restraint Test for hot and cold cracks, which is illustrated in Figure 2-13. The test is used to compare qualitatively the degree of restraint at which cracking occurs in welds during cooling. Lehigh test uses a plate with slots machined into the sides and ends. A single pass weld is produced along a groove that is previously machined along the centerline of the plate. The restraint from the plate and slots produces various levels of cracking in the weld. The level of restraint is altered by changing the length of the slots [87, 88]. The restraint is measured as 2x, where x is the distance from

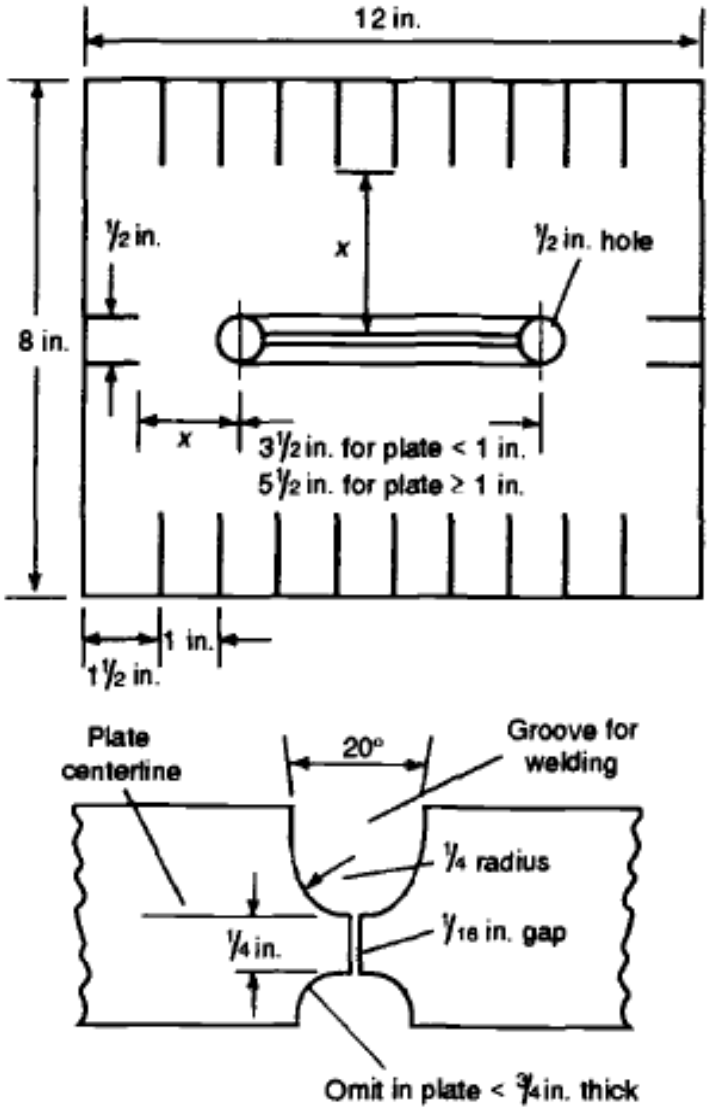

Figure 2 - 13: Schematic showing slotted plate specifications for Lehigh restraint test

Source: *R.D. Stout, S.S. Tor, L.J. McGeady and G.E. Doan, Weld. J., Vo1 26 (No. 11), 1947, p 673-s. Reprinted with permission from the American Welding Society (2 August, 2013)*

the centerline of the weld groove to the bottom of the slots, as shown in Figure 2-13. Several samples with different lengths of slots are usually welded. A threshold level of restraint is determined as the width that is just sufficient to cause cracking.

2.3.3.2 Externally Loaded Tests

These tests involve the application of an external load to the specimen during welding. The externally applied load is usually varied to alter the stress state and thus the severity of cracking in the specimen [86]. An example of externally loaded tests is the Varestraint Test (Hot Crack Test), which was developed at Rensselaer Polytechnic Institute [89] and is the most common test used to evaluate hot crack sensitivity. In Varestraint (variable restraint) test, one end of a rectangular bar (typically 205 by 50 by 6.4 mm) is firmly mounted in fixed position while the opposite end is attached to a hydraulic or pneumatic plunger (Figure 2-14). A weld (usually GTA weld) is produced on the top side of the plate along its longitudinal centerline, beginning at the unsupported end and moving towards the fixed end. When the arc reaches a pre-determined location over a die block, the plate is bent to conform to the radius of the die block. This bending induces an augmented longitudinal strain on the welded surface of the specimen. In order to characterize the strain level at which cracking begins in a material, various die blocks with different radii can be used. For material evaluation, however, a single die block of known radius, which will produce cracking in all samples, is used. Hot cracks usually form along the edge of the weld pool and in the HAZ. The mean values of total crack length, number of cracks, or maximum crack length in duplicate samples of each material are used as a quantitative means of evaluating base metal weldability [87].

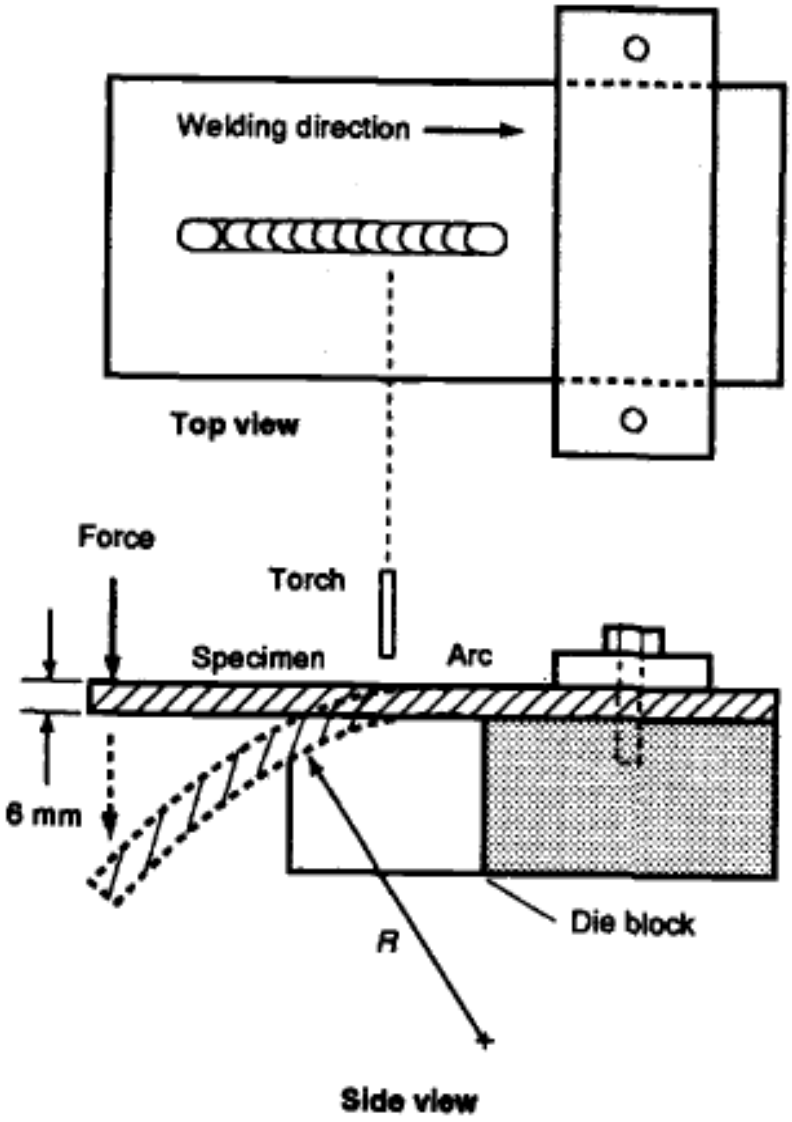

Figure 2 - 14: Set up and sample specifications for Varestraint test

Source: *W.F. Savage and C.D. Lundin, Weld. J., Vo1 44 (No. 10), 1965, p 433-s. Reprinted with permission from the American Welding Society (2 August, 2013)*

2.3.3.3 Gleeble Testing

The Gleeble is a thermomechanical device that has been used in a wide range of applications involving study of a variety of materials problems [86]. The Gleeble has a long and proven history in the study of research-level metallurgical phenomena and also for production-level materials testing to predict service behavior. Applications of Gleeble testing include studies of hot ductility [90, 91], mechanical properties of the weld HAZ [92, 93], continuous cooling transformation diagrams [94, 95], stress relief cracking [96], precipitation kinetics [97], basic weldability [98, 99], strain age cracking [100], constitutional liquation [22, 24, 64], and so on. The applications of Gleeble testing is also not limited to welding, but can be used in the evaluation of other material properties such as thermomechanical fatigue and other forms of thermomechanical testing.

A Schematic diagram showing the components of the Gleeble is shown in Figure 2-15 [101]. The Gleeble system has a full computer interface. It is readily programmed to provide reference signals for closed loop control of both thermal and mechanical operations. The flow of low frequency alternating current in the specimen is used to accomplish heating at rates up to 20,000^{o}C/s. A fine wire thermocouple percussion welded to the specimen surface provides the feedback signal necessary for closed-loop control. The Gleeble can be used to simulate very small, hard-to-study regions in weldments by generating large volumes of microstructure.

2.3.3.4 Measurement of Total Crack Length

The weldability of a metallic material can also be assessed by the measurement of total crack length in experimental specimens [102]. In this method, the experimental specimens are welded under the same condition (materials preparation and welding

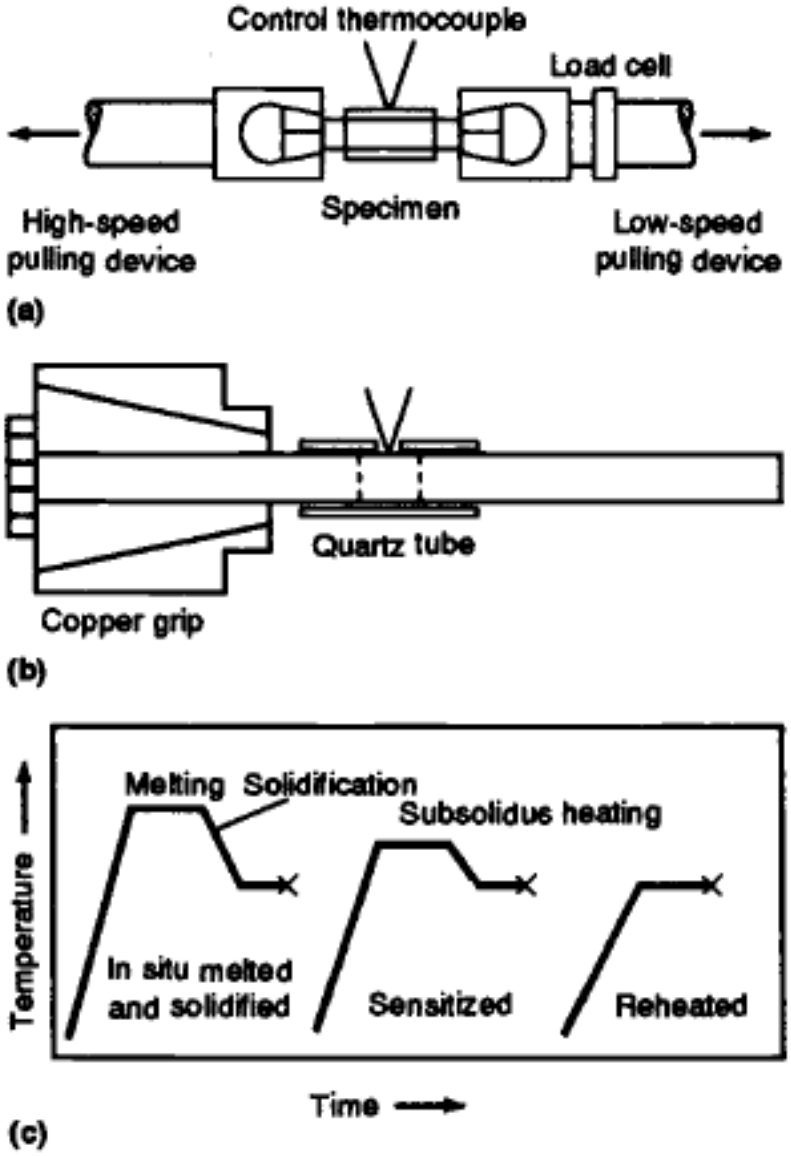

Figure 2 - 15: Gleeble test method. (a) Primary components (b) Close-up view of resistance heater (c) Programmed thermal cycle

Source: *Industrial Heating, Vol. 53 (No 12) Dec. 1986, p.28. Reprinted with permission from Industrial Heating (31 July, 2013)*

parameters) required for the actual weldments. The specimens are then sectioned transverse to the welding direction. The total crack length in each section of the specimen is determined by direct microscopic measurements. Cracking susceptibility in the welded material can be evaluated using the total crack length in two ways. Firstly, the total crack lengths (TCLs) obtained from different specimens can be compared to assess weldability. For this method to be valid, it is required that the specimens are welded using the same set of welding parameters, which is expected to produce approximately the same total area of the HAZ. The crack length in a transverse section of the specimen can be given as

$$L = \sum_{n=1,2..}^{k} l_n \ldots\ldots\ldots\ldots\ldots\ldots\ldots\ldots\ldots\ldots (2-3)$$

where l is the length of individual crack in a section and n is the number of cracks in a section. For statistical correctness, the welded specimens are usually sectioned into about 10 pieces or more and the sum of L values from each section is calculated to determine the TCL. The TCL is given as

$$TCL = \sum_{i=1}^{10} L_i \ldots\ldots\ldots\ldots\ldots\ldots\ldots\ldots\ldots\ldots (2-4)$$

Secondly, if the specimens are welded using different sets of welding parameters or under different welding conditions, the calculation of cracking index (CI) may be required. The CI is a measure of the total crack length normalized with the total area of the HAZ, given by

$$CI = \sum_{i=1}^{10} L_i \Big/ A_T \ldots\ldots\ldots\ldots\ldots\ldots\ldots\ldots\ldots\ldots (2-5)$$

A_T is the total area of the HAZ, measured from all the sections. The CI provides a quantitative assessment of the weldability of a material in terms of the crack length per unit area. Other measurements that can be derived from the TCL measurement include number of cracks, maximum crack length (MCL), average total crack length (ATCL), etc.

Advancements in welding research and continuous, rigorous effort in solving major weldability problems in materials led to the invention of laser-arc hybrid welding. This relatively new development is discussed in details in the next section.

2.4 The Emergence of Laser-Arc Hybrid Welding

Laser-arc hybrid welding is a relatively new joining technology in comparison with other conventional fusion welding processes. It combines the best characteristics of laser welding with those of conventional arc welding processes [15]. Laser welding and arc welding have been used separately for various industrial applications, and both processes possess their specific advantages and limitations. A major idea behind the combination of these two welding processes in laser-arc hybrid welding process is the successful integration of the advantages of both. Laser-arc hybrid welding is also acknowledged to have been designed to overcome problems such as cracking, porosity and brittle phase formation, which are usually encountered during both laser and arc welding [10]. In laser-arc hybrid welding, a laser beam interacts in the same molten pool as the molten pool created by a secondary heat source (in this case, an electric arc) [11]. Both laser beam and arc simultaneously act on the welding zone, and each affects and complements the other [12]. This synergistic effect of laser beam and arc can result in quality advantage, shorter fabrication times, higher productivity and improved cost efficiency [103, 104].

A review of laser-arc hybrid welding process revealed that this method has been known since 1970s [103, 105]. The laser-arc hybrid welding concept was first introduced by Steen et al [7-9], who performed experiments that combined CO_2 laser beam with tungsten inert-gas (TIG) for welding and cutting materials [13]. These first attempts, whereby an electric arc is rooted into exactly the same location on a work piece surface at which a laser beam strikes [7, 9], were made at the Department of Metallurgy and Materials Science, Imperial College of Science and Technology, London. According to Bagger and Olsen [11], although the experiments performed by Steen et al revealed several advantages over other processes, their results did not immediately encourage extensive activities and the development of the process progressed relatively slowly. One of the suggested reasons for this slow development is that laser welding process itself was yet to be developed into an industrially viable process [11]. However, the development of reliable high power lasers in 1980s and the wider industrial acceptance in the 1990s resulted in matured, economic and user friendly laser welding process [11]. In the 1990s, developments in welding research led to the reintroduction of laser-arc hybrid welding, with the combination of high power lasers as the primary heat source and an electric arc as the secondary heat source. Laser-arc hybrid welding also gained industrial acceptance in the 1990s, and several combinations of heat sources and different process arrangements were examined [13]. At present, laser-arc hybrid welding is making an important impact in the welding industry and is now being used for manufacturing components and assemblies in a variety of industrial applications. Some leading global manufacturers in developed countries, such as USA, Germany and UK, are now adopting this fast-growing technology in actual daily production.

2.4.1 Laser Beam Welding

2.4.1.1 The Laser Beam Welding Process

Lasers have been used in joining materials by impinging the heat obtained from the amplification of concentrated coherent light beam on the surfaces to be joined [30]. The beam is usually focused by optical elements (mirrors or lenses) to a small spot size to produce a controlled high power density, which melts the metal and, in case of deep penetration welds, vaporizes some of it. A fusion zone forms which on solidification results in a weld joint. The two major laser technologies, which were invented in the 1960s, are: (1) the solid-state Nd:YAG laser, with emission of light energy at a wavelength of 1064 nm, and (2) the CO_2 laser, with emission at a wavelength of 10.6 μm. The first commercially available lasers were low power pulsed Nd:YAG systems and 100 W CO_2 lasers. Nowadays, up to 8 kW continuous wave Nd:YAG and up to 20 kW off-the-shelf CO_2 lasers are commercially available [106]. In a solid-state laser, a single crystal such as yttrium-aluminum-garnet (YAG) is doped with small concentrations of transition elements or rare earth elements like neodymium. Selective excitation of the electrons of the dopant element can occur upon exposure to high-intensity flash lamps, which subsequently produces laser beams when the excited electrons return to their normal energy states. CO_2 laser, which produces higher power than solid-state laser, is a gas laser produced from the mixture of CO_2, N_2 and He. The gas mixture is continuously excited by electrodes connected to the power supply, producing a laser beam. Nd:YAG and CO_2 lasers have been the two main types of industrial lasers used at high powers for deep penetration.

The major difference between Nd:YAG and CO_2 lasers, in terms of materials processing, is the difference in the wavelength of light emitted [107]. Nd:YAG lasers produce light of 1.06 μm wavelength that can be transmitted to the workpiece by fibre optical cable. However, CO_2 produces light of 10.64 μm wavelength that must be transmitted to the workpiece by reflective and transmissive optical systems, which are more cumbersome, making CO_2 laser less flexible [107]. Fibre laser, which belongs to the large group of solid state laser, was recently developed. It consists of a glass fibre doped with Ytterbium and optically pumped by diodes, which delivers the beam with wavelength of 1070 +/- 5nm [108]. Both solid-state laser and gas laser have been combined with arc welding processes in laser-arc hybrid welding.

The emitted electromagnetic (nearly monochromatic) laser light is usually concentrated to very small (few hundreds of micrometer diameter) spot sizes on the material. In a review work by Mahle and Beyer [109], it was suggested that the most important factors that determine the intensity of the spot at the surface of the material being welded (or processed) are the available optical output power P_L, the wavelength λ of the emitted radiation and the beam parameter product BPP (a measure of beam focusability). For the case of a circular beam with radius w_o, the average value of the intensity, $I_{L,o}$ is defined as:

$$I_{L,o} = \frac{P_L}{A_{L,o}} = \frac{P_L}{\pi w_o^{\,2}} \qquad (2-6)$$

$A_{L,o}$ is the cross-sectional area of the beam. w_o is a function of the focal length of the lens used for focussing, the diameter of the initial beam before focusing and the focusability

parameter BPP. A detailed treatment of w_o for both Gaussian (diffraction-limited) and non-Gaussian (actual) beam is available in the literature [109]

2.4.1.2 Laser-Material Interaction

When a laser beam interacts with the elastically bound electrons in a material, it induces vibration of the electrons. Some of the incident energy of the laser beam is absorbed in the material by the bound electrons and some is reflected by free electrons. The portion of the energy absorbed is determined by the type of material, wavelength of the beam, temperature, surface condition and angle of incidence [106]. The induced vibration of bound electrons in the constrained lattice structure is transmitted through the material and observed as heat. The supply of an amount of heat energy that can effectively overcome mechanical strength in the material bonds results in melting of the material. Welding occurs when the heat source used to melt a common region between two work pieces is retracted and the molten zone is allowed to cool and solidify [106]. There are two modes of laser welding; namely conduction mode and keyhole mode. In conduction mode welding, the heat produced by the laser beam is controlled to allow melting without any significant evaporation. This can be achieved by operating the laser beam out of focus, which creates a balance between the heat produced in the material and the heat conducted away from the interaction spot. When the irradiance of the laser beam is high, the heat produced can be sufficient to break atomic bonds, resulting in vaporization. A still higher intensity can cause electrons to be removed from the vaporized metal atoms and from gases in the interaction zone, resulting in plasma generation. The high temperature vapour and plasma will tend to expand, thus generating a recoil force that pushes on the surrounding molten material, creating a keyhole.

Keyhole welding favours much higher penetration compared with conduction mode welding due to additional opportunities for laser absorption through multiple reflections in the keyhole. The temperature of vapour and plasma in the keyhole can be extremely high, approximately 2000 K for Nd:YAG and 6000 – 10,000 K for CO_2 welding [110]. Illustrations of conduction mode and keyhole mode welding are provided in Figure 2-16 [109]. Conventionally, laser beam welding is carried out without filler alloys. The weld zone and adjacent regions are usually shielded from the atmosphere by a blanket of inert gas. Argon, helium or mixtures of the two gases are typically used.

2.4.1.3 Benefits of Laser Beam Welding

Laser welding is capable of joining materials in applications with limited accessibility such as welding of gears, applications that require high welding speed such as longitudinal seams on pipes, and applications that require precisely controlled heat input such as components for electronics [111]. The major benefit of using laser welding lies in its high power density. This enables high welding speeds with deep penetration, and narrow fusion and heat-affected zones [10, 18]. In laser welding, the ratio of the depth of penetration to the weld width is high [112]. Also, the resultant low heat input welds produce low residual stresses and very little structural distortion, such that the effect of heat on the material is minimal, while achieving high welding speed at the same time [10, 18, 112]. Single pass welding of materials with thick sections is possible [10]. The process is also suitable for welding dissimilar parts that vary greatly in mass and size. Vacuum and X-ray shielding are generally not required.

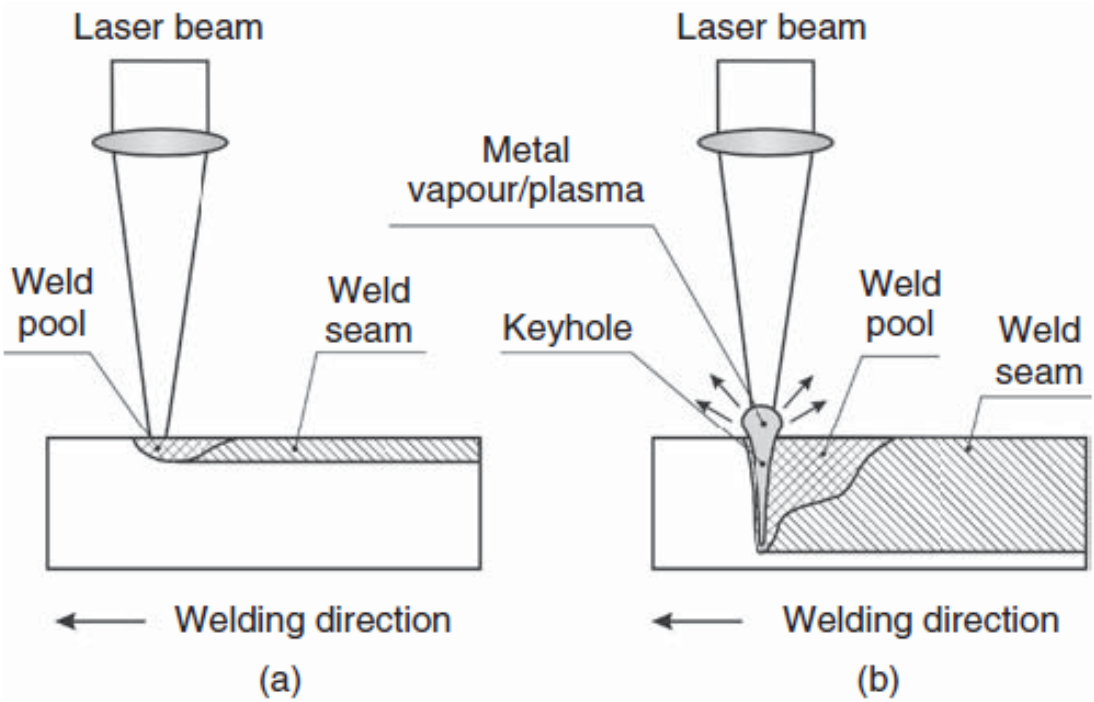

Figure 2 - 16: Schematic diagrams of (a) conduction mode laser beam welding, and (b) keyhole mode laser beam welding

Source: *Hybrid Laser-Arc Welding, Edited by Flemming Ove Olsen, Copyright 2009, ISBN 978-1-84569-652-8. Reprinted with permission from Woodhead Publishing Limited (14 May, 2013)*

2.4.1.4 Shortcomings of Laser beam Welding

The limitations of laser welding include high tooling and operating cost, high requirements for part positioning and clamping, high welding speeds leading to high solidification rates and subsequent porosity and cracking [11, 13]. Keyhole instability and formation of brittle phases also affect the weld quality [10]. The ability of laser welding process to bridge root openings is low as a consequence of its small focus diameter [103, 113]. The inability to bridge wide gaps necessitates precision assembly of parts, which is usually difficult to attain in production [90]. Another major drawback in the use of laser beam welding is the very high reflectivity of a laser beam by the metal surface, which reduces the amount of penetrating beam. This makes it difficult to join highly reflective materials such as aluminum, copper and gold by laser welding [11]. The low energy efficiency of lasers can also be considered as a disadvantage, although recent advancements have led to the invention of fibre lasers and direct diode lasers that offer up to 30 % (or higher) wall plug efficiency [109].

2.4.2 Description of Arc Welding Processes

As mentioned earlier, arc welding uses an arc that is struck between an electrode and the workpiece, to generate heat that melts the filler (which could sometimes be the electrode) and the base metal. This produces a molten pool under the protection of an inert gas blanket. As the heat source retreats from the molten pool area, the pool solidifies, forming a weld bead and a heat-affected zone (HAZ) adjacent to the weld bead. In principle, arc welding is based on an electric gas discharge under atmospheric pressure conditions between two open terminals, namely the welding electrode and the work piece. The gaseous zone between the welding electrode and the work piece is partially

ionized, resulting in the generation of visible plasma arc, which closes the welding current circuit and ensures continuous transfer of electrical energy between the electrode and the work piece. Current is transferred by the flow of electrons from the negatively charged cathode to the positively charged anode. Both positive and negative polarities can be applied depending on the work piece material and the amount of heat input required. Arc welding is still the most applied welding heat source, with gas metal arc welding (GMAW) and tungsten inert gas (TIG) welding being especially very popular [109].

Gas Metal Arc Welding (GMAW)

GMAW joins metals by using a high temperature ionized column of gas (or plasma) that spans between a consumable electrode and the work piece. The diameter of the electrode is typically between 0.89 and 1.6 mm. The arc temperature, which is usually in the order of 6600^{o}C, is sustained by high current (between 100 and 450 A) that is provided by a low potential (15 to 35 V) welding power supply. A typical GMAW welding set-up is illustrated in Figure 2-17 [106]. The electrical voltage and current are provided by the power supply. The current is fed through electrical cables to the contact tip, which is connected to the consumable filler wire. The electrical circuit is completed by connecting the work piece to the other lead from the power supply. The filler wire is fed into the welding torch by means of a wire feeder. The shielding gas is also fed coaxially through the torch around the contact tip. The welding torch can be either manually operated or connected to a robot. The various welding modes available in GMAW include short circuit, globular, spray and pulsed spray transfer modes.

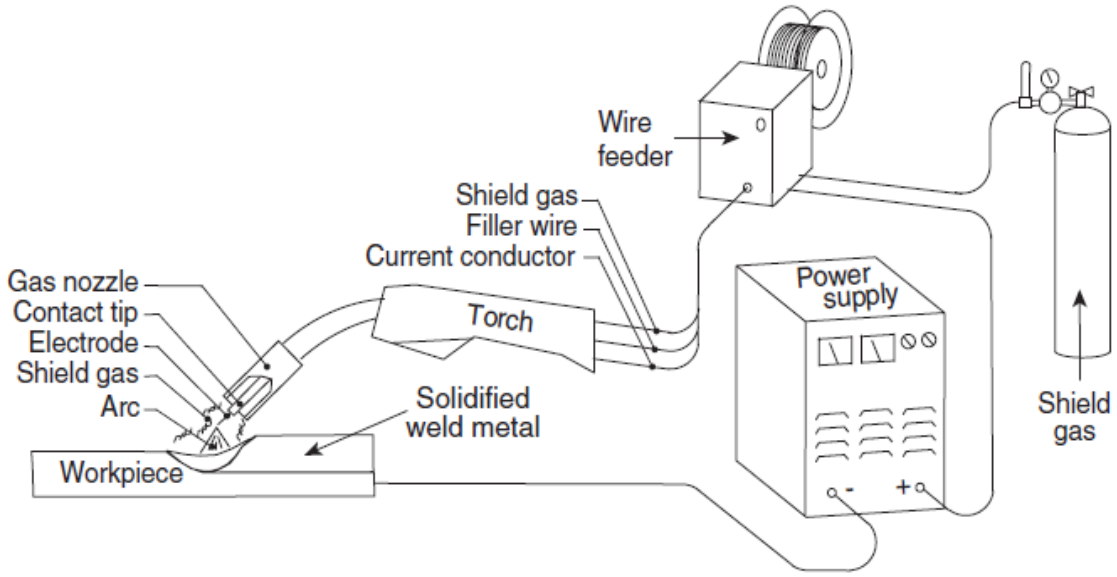

Figure 2 - 17: Schematic of a typical GMAW set-up

Source: *Hybrid Laser-Arc Welding, Edited by Flemming Ove Olsen, Copyright 2009, ISBN 978-1-84569-652-8. Reprinted with permission from Woodhead Publishing Limited (14 May, 2013)*

Tungsten Inert Gas (TIG) Welding

In TIG, which is also usually called Gas Tungsten Arc Welding (GTAW), the heat is produced between non-consumable tungsten electrode and the metal work piece [53]. The electrode, weld pool, arc and adjacent heated work areas of the work piece are protected from atmospheric contamination by a gaseous shield, which is provided by a stream of gas (usually an inert gas) or a mixture of gases. The torch holding the tungsten electrode is connected to the shielding gas cylinder as well as one terminal of the power source, with the tungsten electrode in contact with a water-cooled copper tube. TIG is an all-position process and is especially well-adapted to the welding of thin metals, often as thin as 0.15mm (0.005in).

2.4.2.1 Benefits of Arc Welding Processes

Conventional arc welding processes are highly efficient, low cost energy processes, with the ability to bridge relatively large gaps [11, 18]. In arc welding, it is easily possible to include filler wire [105], which should be carefully chosen based on metallurgical requirement. The selection of filler alloys of certain compositions can assist in achieving desired metallurgical properties by supplying alloying elements that may be lost through volatilization [109]. Addition of fillers can also aid in accommodating joint gaps. The low cooling rates, due to lower welding speed and higher heat input, prevents the formation of brittle phases[10, 11], and in some cases, minimizes or eliminates HAZ cracking. It is also possible to weld highly reflective materials such as Aluminum and Gold [11]. Arc welding processes, such as GMAW, can be easily automated and can be adapted to joining a wide variety of metals.

2.4.2.2 Shortcomings of Arc Welding Processes

Arc welding is characterized by a wide fusion zone. The high heat input per unit length results in high residual stresses and distortion, especially in welding that requires high deposition rates. Productivity is reduced due to the low welding speed. The propensity for solidification cracking could be high. Single pass welding of thick materials is usually difficult to achieve due to the shallow fusion zone and reduced penetration [10]. Therefore, multi-pass welding is usually required. The requirement for multi-pass welding makes the process time consuming [114]. Multi-pass welding also results in much higher heat input and excessive consumption of filler alloys. Another limitation is the possible erratic or inconsistent arc ignition which leads to the destabilization of the arc [115]. Improper parameter selection can result in spatter.

Laser-arc hybrid welding is a combination of laser welding and arc welding, where there is simultaneous interaction of the two heat sources. The benefits of the synergistic interaction between a laser beam and an electric arc during laser-arc hybrid welding cannot be overemphasized. The most important aspect of laser-arc hybrid welding is the integration of the advantages of laser and arc welding processes, and this is discussed next.

2.4.3 The Basic Principle of Laser-Arc Hybrid Welding

The basis for laser-arc hybrid welding is the fact that two different heat sources – laser beam and electric arc – can be instantaneously combined. The different combinations that have been used in laser-arc hybrid welding include: Laser + GMAW (MIG/MAG), Laser + GTAW (TIG), Laser + PAW, where the laser beam could be CO_2 laser, Nd:YAG laser, fibre laser, etc [11, 112, 113]. It is generally accepted that the laser beam acts as the

primary heat source while the electric arc augments the laser beam as the secondary heat source in laser-arc hybrid welding [7-9, 11, 13]. Contrary to this accepted concept, heat source combinations where the arc acts as the primary heat source are referred to as laser-augmented or laser-supported arc welding processes.

During laser-arc hybrid welding, the laser beam is focused to obtain very high intensities (10^6 W/cm^2 or greater). The energy flow density of the freely burning arc can also be more than 10^4 W/cm^2. As soon as the laser beam hits the surface of the material, the surface is heated on this spot to vaporization temperature, forming a vapour cavity in the weld metal due to escaping metal vapour. The arc also provides additional heat at the upper weld region. A schematic drawing of laser-arc hybrid welding process is presented in Figure 2-18 [109]. For certain reflective materials such as aluminum and copper, the initial reflectance on the surface must be overcome [12, 103]. After vaporization temperature has been reached, the vapour cavity is formed and nearly all radiation energy from the laser and the energy from the arc can be put into the workpiece. The energy required to ensure that nearly all radiation and arc energy are put into the workpiece depends on the absorption of laser radiation, while the absorption of laser radiation is determined by temperature. However, vaporization takes place not only from the surface of the workpiece, but also from the welding wire, such that more metal vapour is available. This facilitates the input of laser radiation and prevents process dropout [8, 85-88].

In laser-arc hybrid welding, both the laser beam and arc act simultaneously in the same process zone, leading to an increase in weld penetration and welding speed, compared to each single process. This is in contrast to the sequential arrangement whereby two

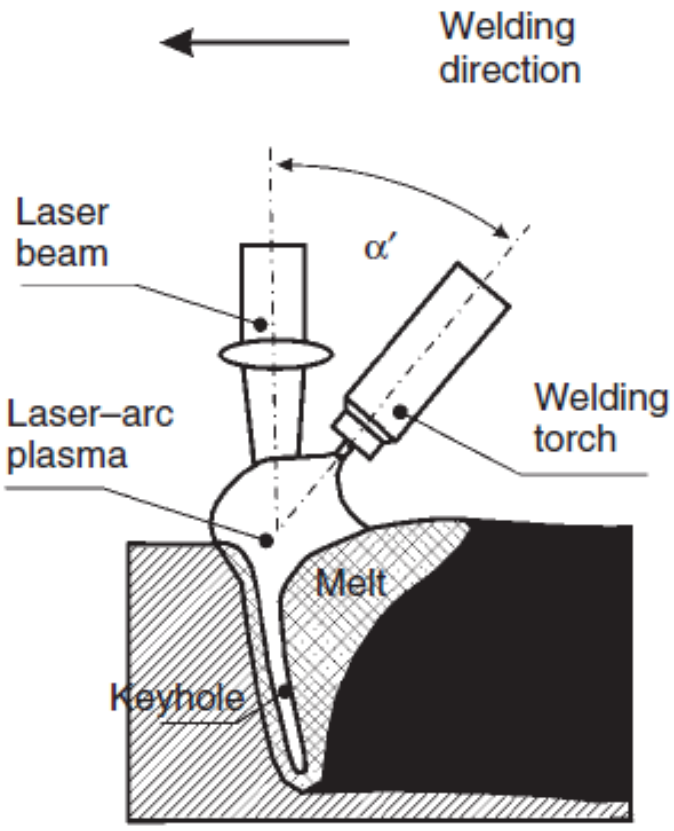

Figure 2 - 18: Schematic illustration of laser-arc hybrid welding

Source: *Hybrid Laser-Arc Welding, Edited by Flemming Ove Olsen, Copyright 2009, ISBN 978-1-84569-652-8. Reprinted with permission from Woodhead Publishing Limited (14 May, 2013)*

separate welding processes take place successively. The character of the overall process may be determined either by the laser or the arc, depending on the ratio of the two power inputs [103]. Laser-arc hybrid welding has several advantages over laser welding process and arc welding process, and these are discussed next.

2.4.4 Advantages of Laser-Arc Hybrid Welding

Laser-arc hybrid welding integrates the best attributes of both laser welding and arc welding processes, and has also addressed their limitations. The weld pool is usually larger than laser welds and deeper than arc welds made with the same laser and arc welding parameters [13]. The process is well-adapted to the welding of thick sections.

In comparison to laser welding, it has been reported that laser-arc hybrid welding is characterized by higher process stability, higher bridgeability, increased welding speed, deeper penetration, increased weldable material thickness, reduced cracking and porosity susceptibility, and lower capital investment cost due to savings in laser energy [11, 13, 103]. Full penetration depths at gaps larger than 1mm was realized in a 6mm steel using a 2kW CO_2 and 2.7kW MAG [116]. A very deep penetration of 16 mm was achieved in the laser-MAG hybrid welding of pipeline steel by 10.5 kW laser power at a welding speed of 1.2 m/min, without centerline pores or cracking as determined by X-ray testing [108]. An increase in welding speed by a combination of laser beam and arc, compared to laser beam alone, during the joining of various materials has been reported [8]. For a 0.6mm stainless steel, 50% increase in weld penetration was reported when a 400W CO_2 laser was combined with an arc in PALW (Plasma arc augmented laser welding) [117]. Porosity was reduced significantly in AA5083 aluminum alloy by combining 12kW CO_2 laser with 3kW MAG [118]. A complete elimination of cracks and penetration of 6-8mm

were achieved in 10mm A6061 aluminum alloy by combining a 3.5kW Nd:YAG with a TIG torch [119].

Compared to arc welding, the reported advantages of laser-arc hybrid welding include: higher welding speed, lower heat input per unit length, lower residual stresses and distortions, better mechanical properties, deeper penetration at higher welding speed, narrower weld joint, greater process stability, and very smooth transition between weld and base material [10, 15, 103, 104]. The ability of laser-arc hybrid welding to produce deeper penetration weld has been demonstrated in Laser-TIG welding of a Magnesium alloy [120]. It has been demonstrated that less total heat input is required to produce a particular weld penetration in hybrid laser gas metal arc welding compared to GMAW process alone, as shown in Figure 2-19 [121]. Steen [7], in his earlier experiment on the effect of adding a laser to an electric arc on the arc current-voltage relationship using mild steel, also demonstrated that an unstable arc can be stabilized by a laser beam.

Overall, the important advantages of laser-arc hybrid welding can be summarized as:

1. Increased welding speed
2. Increased weld penetration
3. Improved gap and misalignment tolerance
4. Enhanced process stability
5. Reduced cracking and porosity
6. Single pass welding of thick sections
7. Enhanced overall weld quality

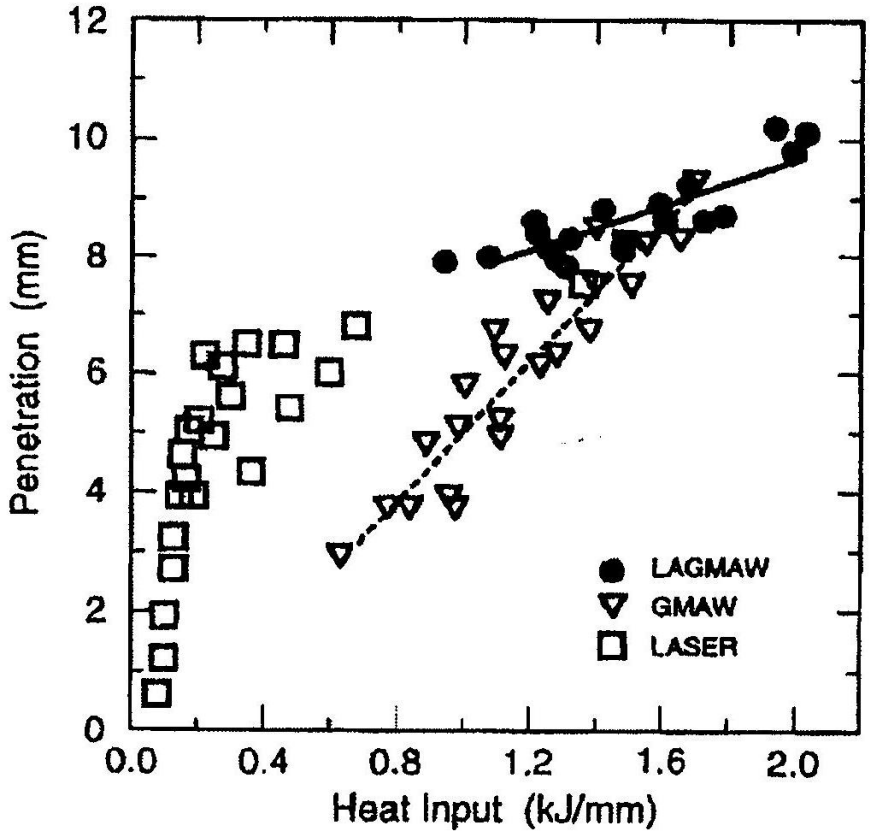

Figure 2 - 19: Penetration depth at different heat input levels for CO_2 laser, GMAW and hybrid LAGMAW process

Source: *C.V. Hyatt, K.H. Magee, J.F. Porter, V.E. Merchant and J.R. Matthews: Weld. J., (2001) pp.163s-172s. Reprinted with permission from the American Welding Society (2 August, 2013)*

2.4.5 Parameters in Laser-Arc Hybrid Welding

In addition to welding parameters which are related to laser welding and arc welding as individual processes, a number of parameters are also associated with laser-arc hybrid welding. The parameters of laser-arc hybrid welding include [11, 113, 122, 123]:

- Type of laser (Nd:YAG or CO_2)
- Type of arc (MIG-MAG, TIG or Plasma)
- Relative positions of laser and arc
- Laser power
- Arc power (arc voltage and current)
- Ordering of the process (laser or arc first?)
- Laser focal point position
- Angle (or inclination) of electrode
- Shielding gas type
- Shielding gas flow rate
- Welding speed
- Welding wire type
- Welding wire diameter
- Wire stick-out
- Welding wire feed speed
- Root opening tolerance

All these parameters influence the overall quality of the laser-arc hybrid welded joint. In the next sub-section, some reported effects of welding parameters during laser-arc hybrid welding of various materials are discussed.

2.4.6 Effect of Welding Parameters

Welding parameters play important roles in determining the characteristics and quality of a welded joint. The depth of penetration during laser-arc hybrid welding has been observed to be influenced by the distance between laser and arc, laser focal position, welding speed and laser power. It has been suggested, based on reports in the literature [11, 115, 118, 119, 123, 124-126], that an ideal relative distance between the laser and arc is about 1-3mm. For example, the deepest weld penetration was obtained in a stainless steel alloy when the distance between the sources was about 2-4 mm [122]. In laser-arc hybrid welding in which a 1.8kW Nd:YAG laser was coupled with a TIG torch, it was reported that the penetration was deeper and the bead width narrower for greater relative distance between laser and arc (>2mm) when TIG beam is positioned before the laser beam, but the penetration is deepest for a relative distance of 1-2 mm and shallower at distances greater than 2mm when YAG laser beam is positioned before the TIG arc (Figure 2-20 [125]). Positioning the arc point of interaction in the laser point of interaction has been reported to result in reduced penetration [115]. In type 304 stainless steel, it has been demonstrated that an increase in laser power produced an increase in weld penetration depth [125].

Process ordering was also found to influence weld characteristics. It has been observed that an increase in penetration of 10% could be obtained if a MAG source is placed after the laser [118]. The laser focal point position in laser-arc hybrid welding is not usually the same as that of pure laser due to the large curvature of the molten pool created by the arc [11]. The choice of this focal point position depends on the type of laser, laser power, arc power, and the material [116, 121, 125].

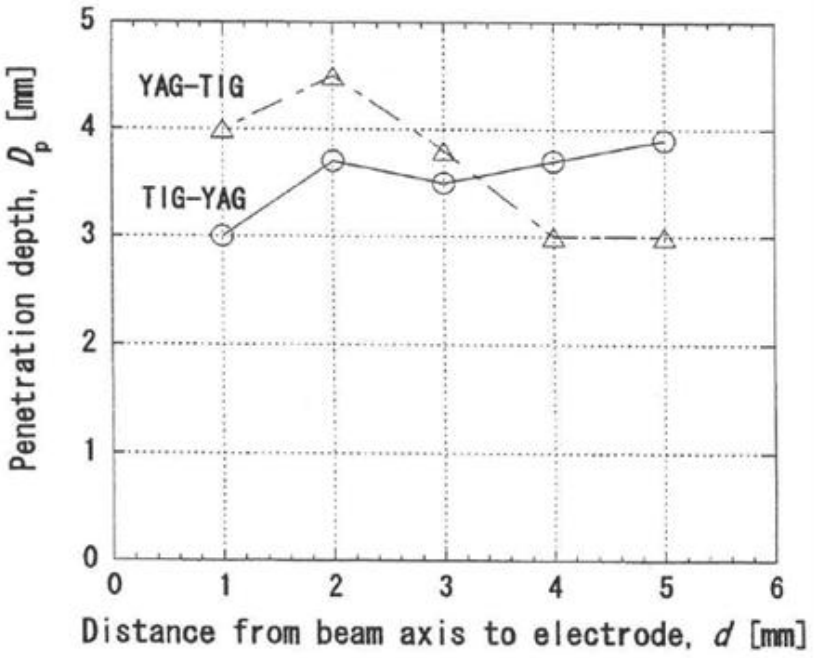

Figure 2 - 20: Influence of distance on penetration depths in laser-arc hybrid welding of Type 304 SS

Source : *Y. Naito, S. Katayama and A. Matsunawa: First International Symposium on High-Power Laser Macroprocessing – Proceedings of SPIE, Vol. 4831 (2003) pp. 357. Reprinted with permission from The International Society for Optical Engineering (23 May, 2013) and one of the Authors, Seiji Katayama (4 June, 2013).*

The maximum welding speed possible for a particular laser power has been shown to increase with increased arc current [127]. Increase in welding speed, in turn, has been observed to reduce the depth of penetration [125, 127]. The depths of penetration obtained during Nd:YAG/TIG hybrid welding process at different welding speeds is presented in Figure 2-21 [125]. Porosity was also found to reduce with increasing arc current, and was almost absent at 240A, for a YAG-MIG hybrid welding of type A5052 aluminum alloy [128]. An increased arc voltage has been also reported to result in an increased bridgeability [122].

The type of shielding gas for laser-arc hybrid welding depends on the type of laser, whether CO_2 laser whereby plasma absorption takes place, or Nd:YAG laser where plasma absorption is not a major concern [11]. Figure 2-22 [129] shows that under the same conditions, the penetration depth of hybrid CO_2 laser-TIG welded stainless steel with low He content in the shielding gas is shallow, but the penetration depth increased with increasing He content in the He-Ar mixture. It was observed that when the He content is greater than 50%, the 3 mm stainless steel is fully penetrated. It has also been reported that the penetration and geometry of weld beads depended on the volume of oxygen in ambient air during laser-arc hybrid welding of steel with low S content [128]. The effect of the type and composition of filler materials on mechanical properties in laser-arc hybrid welding of high strength steels has been also studied and reported [104].

2.4.7 Industrial Application of Laser-Arc Hybrid Welding

The laser-arc hybrid welding process is currently being used in production. It is making an important impact in the medium and heavy section, as well as thin sheet, welding industries [16, 17], with the goal of achieving a higher product quality while the

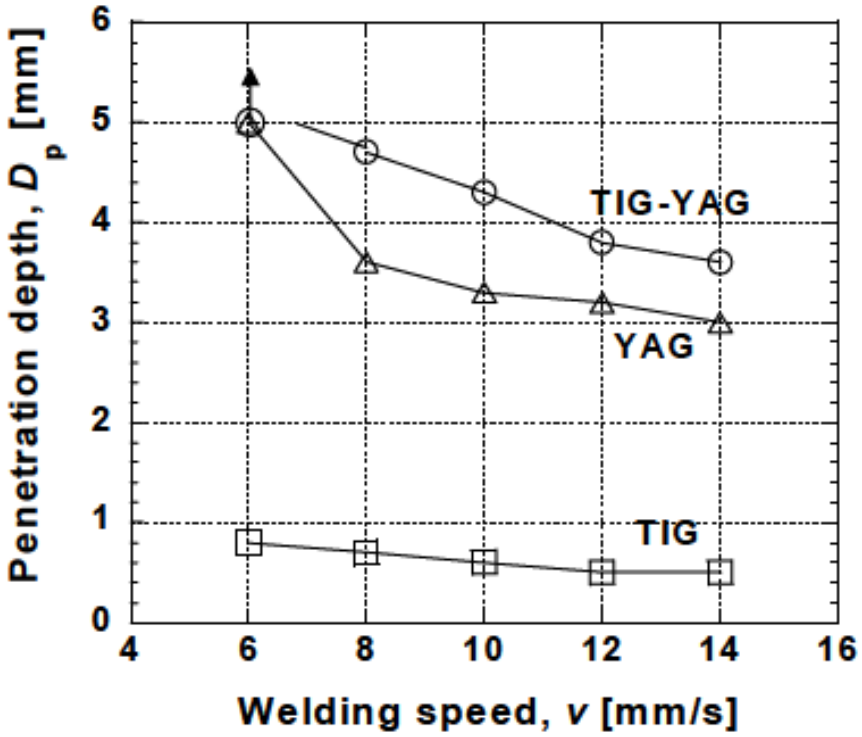

Figure 2 - 21: Influence of welding speed on penetration depth in laser-arc hybrid welding of Type 304 SS

Source : *Y. Naito, S. Katayama and A. Matsunawa: First International Symposium on High-Power Laser Macroprocessing – Proceedings of SPIE, Vol. 4831 (2003) pp. 357. Reprinted with permission from The International Society for Optical Engineering (23 May, 2013) and one of the Authors, Seiji Katayama (4 June, 2013).*

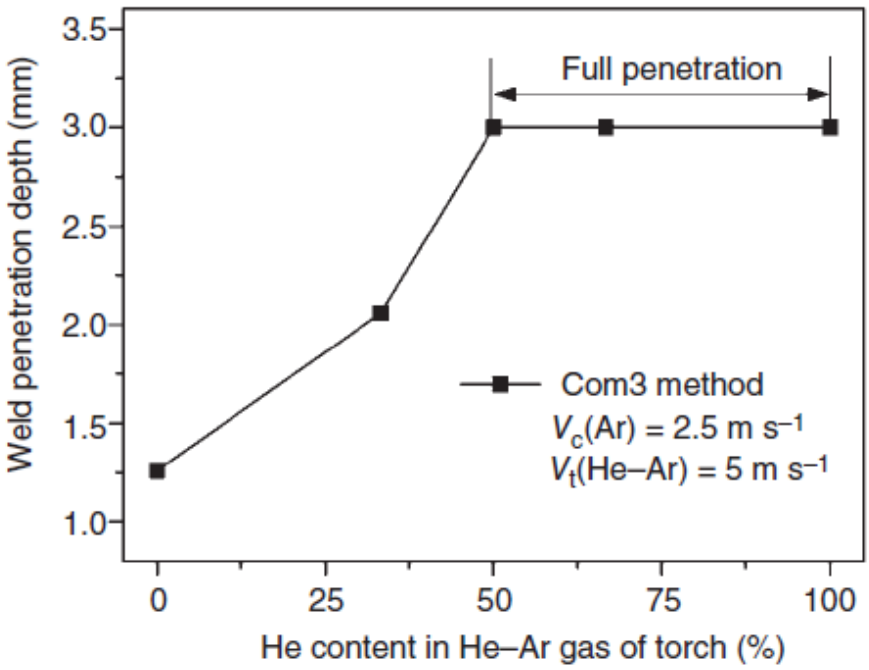

Figure 2 - 22: Effect of He content in He-Ar shielding gas on penetration depth of CO_2 laser-TIG hybrid welded 3 mm thickness 316L stainless steel plate.

Source: *Hybrid Laser-Arc Welding, Edited by Flemming Ove Olsen, Copyright 2009, ISBN 978-1-84569-652-8. Reprinted with permission from Woodhead Publishing Limited (14 May, 2013)*

performance is concurrently being improved. According to Pilarczyk et al [112], the first industrial applications of laser-arc hybrid welding were car bodies made of aluminum plates, using Nd:YAG/MIG, and steels, using laser CO_2/MIG. It is also being claimed that the first Laser/MIG-MAG hybrid welding system in serial operation was put in operation by Fraunhofer ILT for welding oil tanks in year 2000 [130]. Some current applications of laser-arc hybrid welding are discussed.

2.4.7.1 Automotive Applications

Leading global manufacturers that use laser-arc hybrid welding in automobile production include Volkswagen, Daimler (maker of Mercedes Benz vehicles) and Audi [12, 131]. The motivations for these companies in adopting this joining technique include: high weld quality and reliability, perfect fitting on the car body, light weight potential, good metallurgical properties, and reduced cycle time. Higher gap bridging ability, in comparison to laser welding alone, is another major advantage [11].

The strategy of Volkswagen is to have the highest amount of laser weldments in the automotive industry [103]. One of Volkswagen's applications of laser-arc hybrid welding is in manufacturing the Phaeton model (previously called Concept D1). All doors of this car model are laser-arc hybrid welded. Volkswagen's requirement included a high degree of stiffness in the door structure, which also required a good combination of sheet, cast, and extruded materials. Aluminum was the preferred and used material (due to low weight), and without laser-arc hybrid welding, use of big and heavy aluminum cast materials would have been necessary. The Phaeton door consists of 7 gas metal arc, 11 laser, and 48 laser-arc hybrid weldments, making a 4980mm total length of welds on the door [103]. The welds are mainly fillet seams on lap joints and butt seams.

For power train production at Daimler, an axle component type 204 from the Daimler Chrysler C-Class was welded by laser-arc hybrid welding at 4.5 m/min speed and 9.0 m/mm wire feed rate [74]. Figure 2-23 [131] shows a laser hybrid welded axle components at Daimler. Also, laser-arc hybrid welding is employed in joining the lateral roof frame of Audi A8, which is equipped with various functional sheets [74]. Each vehicle comprises of a total of 4.5 m of weld seams (Figure 2-24 [131]).

2.4.7.2 Shipbuilding and Railway Applications

Laser-arc hybrid welding has also found applications in shipbuilding and railway industries. While the automobile industry is a high volume industry, the ship building industry is characterized by several kilometers of welding in a single ship [11]. In 2001, the shipyard Meyer Werft in Papenburg, Germany, invested in a technically ambitious panel manufacturing line, which is equipped with a total of four high power (12 kW) laser hybrid welding machines [132]. Butt welds were made from 20 m long and 4 m wide steel plates to form deck panels, up to 20 m by 20 m. Figure 2-25 [132] shows the first laser welded sandwich panels produced at Meyer Werft. By 2002, all flat sections for the ships produced at Meyer Werft came from a new pre-manufacturing workshop where laser hybrid welding had been integrated. It was estimated that the amount of laser hybrid welds in a large cruise ship was approximately 50% of the total weld length, which may be of the order of 400 km [132], the majority of the plates being in the order of 5 – 8 mm in thickness.

Aker Yard, Finland builds cruise ships and ferries, and has three shipyards in Finland. Aker Yard implemented laser hybrid welding, where a 6 kW fibre laser was integrated into the existing panel production line in December 2006. This reduced the total cost of

(a)

(b)

Figure 2 - 23: An axle component from the Daimler C-Class.

Source: *Hybrid Laser-Arc Welding, Edited by Flemming Ove Olsen, Copyright 2009, ISBN 978-1-84569-652-8. Reprinted with permission from Woodhead Publishing Limited (14 May, 2013)*

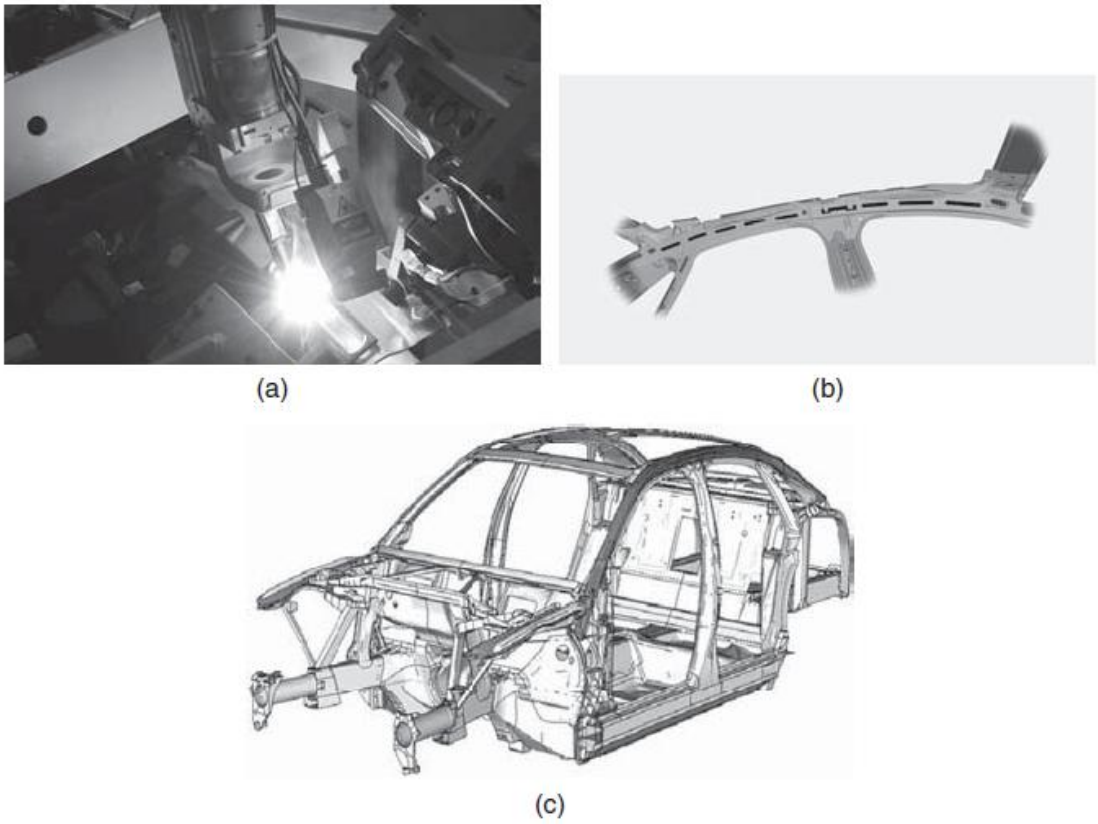

Figure 2 - 24: Laser hybrid welding at Audi. The OEM applies the laser hybrid welding process for 4.5 m of weld seams in the roof area of the new A8 and thus achieves higher welding speeds and stronger seams.

Source: *Hybrid Laser-Arc Welding, Edited by Flemming Ove Olsen, Copyright 2009, ISBN 978-1-84569-652-8. Reprinted with permission from Woodhead Publishing Limited (14 May, 2013)*

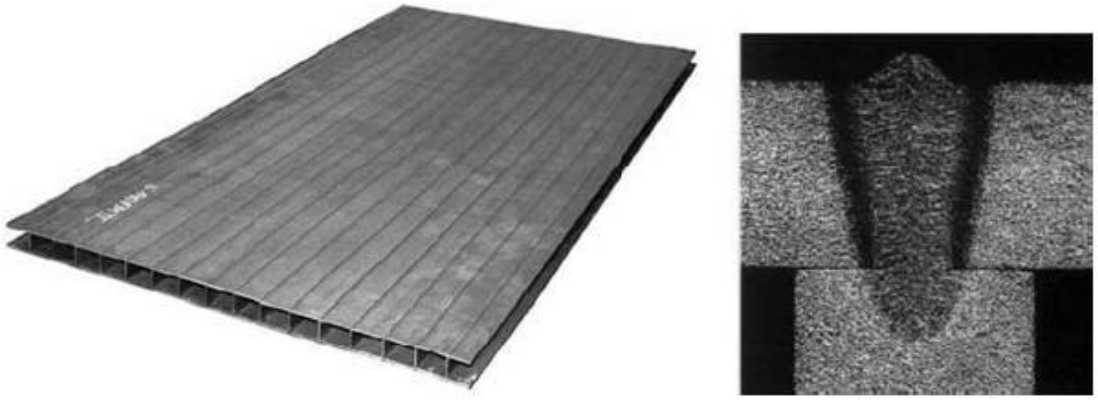

Figure 2 - 25: The first laser welded sandwich panels produced at Meyer Werft, Germany

Source: *Hybrid Laser-Arc Welding, Edited by Flemming Ove Olsen, Copyright 2009, ISBN 978-1-84569-652-8. Reprinted with permission from Woodhead Publishing Limited (14 May, 2013)*

investment. An overview of the installation and the various elements are provided in Figure 2-26 [132]. Also, the Laser Fabricated Ship Structures program of the U.S. Office of Naval Research developed a laser-arc hybrid welding technology for the production of T-beams from high strength plates at high welding speeds with very low distortion [15]. The U.S. shipyard established a two-year payback threshold for economic justification of capital purchases on laser-arc hybrid welding [15]. Many other shipbuilding companies have adopted laser-arc hybrid welding in production. These include Blohm & Voss, Fincantieri, Odense Steel Shipyards, amongst others [132].

In year 2000 Cloos Schweiβtechnik in Haiger, Germany, introduced a hybrid burner that can be operated by a robot for railway applications [17]. This laser-arc hybrid technology, developed by Cloos, is being used by Alstom Reichshoffen in Alsace, France. The equipment consists of a laser-arc hybrid head with a rotating burner axle that was built onto a welding robot and a seam monitor, with a laser sensor, which guarantees the quality of the weld seams on the side walls of the train cars.

2.4.7.3 Other Applications

Aside from automobile, shipbuilding and railway applications, laser-arc hybrid welding is used also in the construction of bridges, pipelines, earthmoving equipment, lifting equipment and cranes [15, 111]. It is useful for joining components in transport, petrochemical and mineral processing industries [18]. These components include pressure vessels, autoclaves and container panels. In addition, laser hybrid welding technology has been successfully applied in the joining of bicycle structures that are made of magnesium alloys (Figure 2-27 [133]).

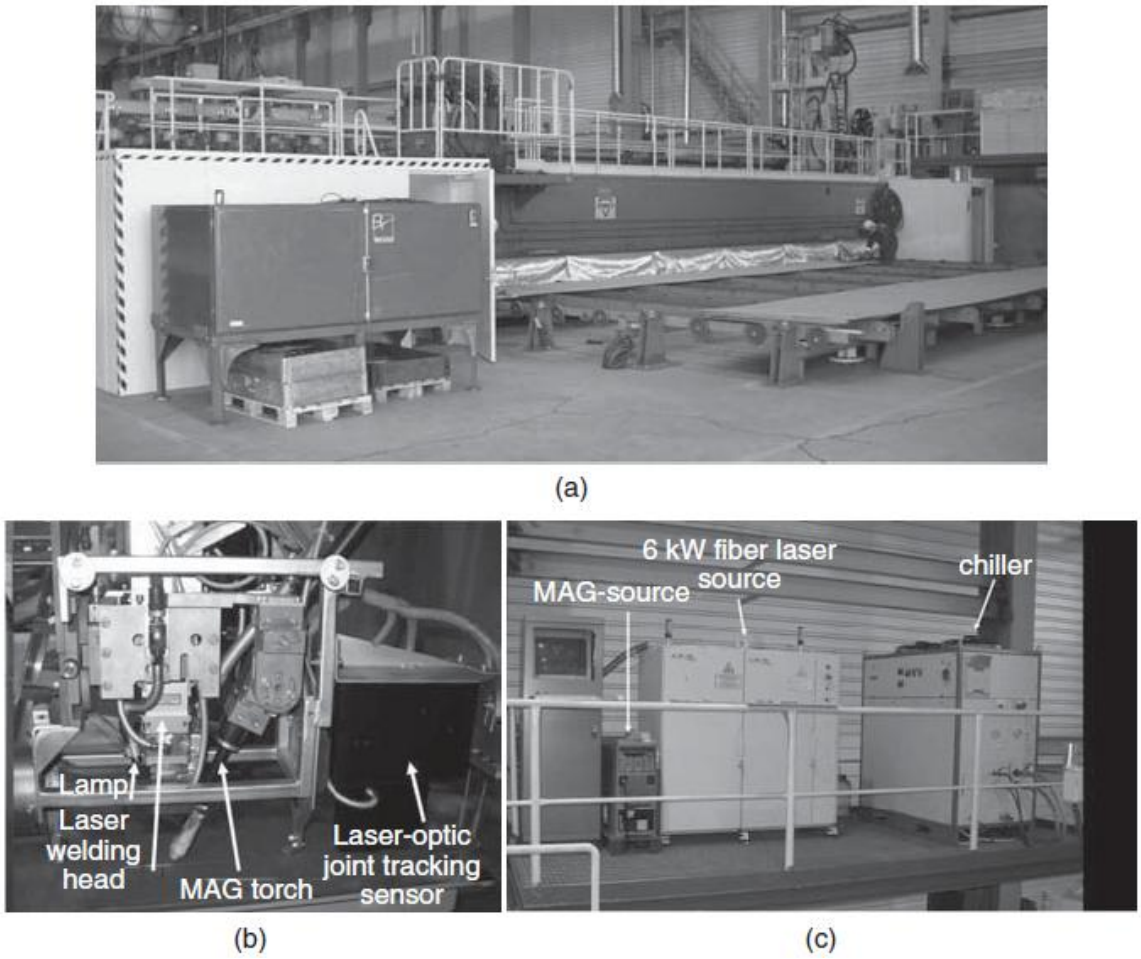

Figure 2 - 26: (a) An overview of installation, (b) the laser head and (c) the laser source and MAG power supply for the laser hybrid welding set up at Aker Yard

Source: *Hybrid Laser-Arc Welding, Edited by Flemming Ove Olsen, Copyright 2009, ISBN 978-1-84569-652-8. Reprinted with permission from Woodhead Publishing Limited (14 May, 2013)*

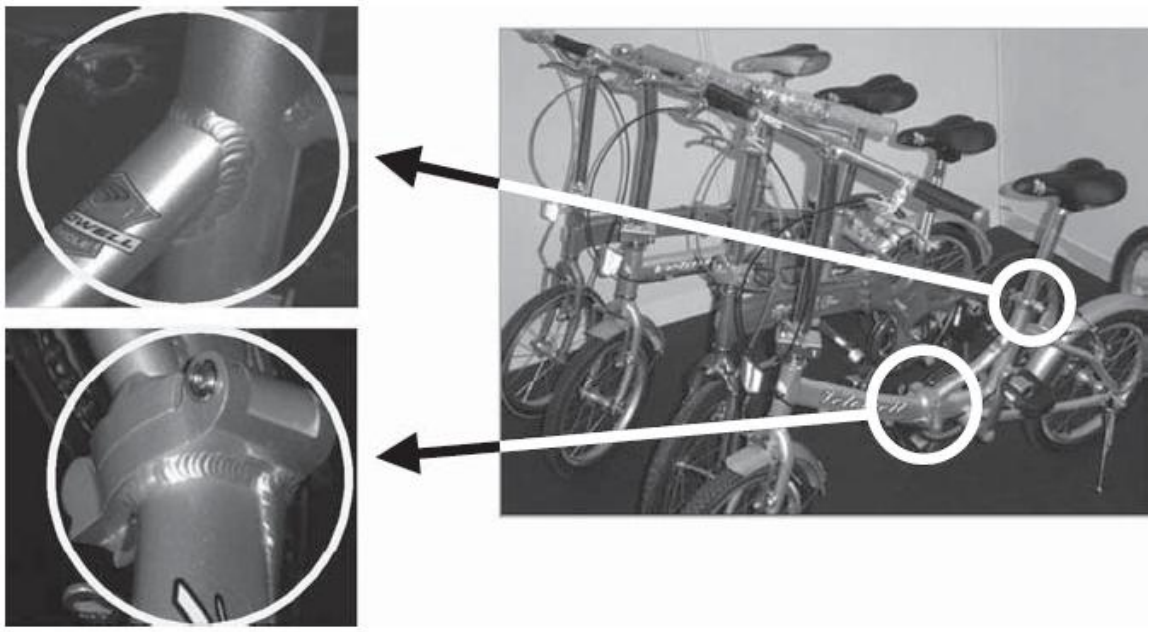

Figure 2 - 27: Laser hybrid welded magnesium alloy bicycle

Source: *Hybrid Laser-Arc Welding, Edited by Flemming Ove Olsen, Copyright 2009, ISBN 978-1-84569-652-8. Reprinted with permission from Woodhead Publishing Limited (14 May, 2013)*

Another important aspect of the application of laser-arc hybrid welding relates to the types of materials that are currently being welded by the process. A review of previous works revealed that the process has been applied to the joining of different iron based materials including stainless steels [113, 122, 125, 128], mild steel [7, 127], high strength steels [104, 113] and other types of steels [130, 134]. Laser-arc hybrid welding process has also found wide a application in the welding of aluminum and aluminum alloys [112, 130, 135], which are particularly used in the manufacturing of automobile parts. Laser-arc hybrid welding of various types of aluminum alloys has been reported. Although the process has also been applied to the joining of magnesium alloys [120], titanium and tin plates [8], very limited information exists about the joining of these materials using laser-arc hybrid welding.

2.4.8 The Current State of Laser-Arc Hybrid Welding

In the previous sections the principle, benefits, parameters and applications of laser-arc hybrid welding were reviewed. On the basis of this review, it is evident that laser-arc hybrid welding, though useful in a wide range of industries, is only largely used in applications where steels and aluminum alloys are the principal materials. Also, the currently available information shows that a substantial amount of work is required in the optimization of the welding process for steel and aluminum, especially considering the fact that several combinations of the process parameters are possible. In addition to the existence of several process parameters, different secondary heat sources can also be combined with laser in a variety of process arrangements, depending on the specific joining assignment [13]. Currently, most of the relevant welding parameters are experimentally determined; confirming that process optimization for each material

requires a substantial level of practical experience [13]. It has been suggested that expanding the application of laser-arc hybrid welding in the joining of important materials will require considerable research, rigorous characterization and cost analysis [10]. Some of the areas, which have not been given much attention, toward which research effort on laser-arc hybrid welding is currently being tailored include: the understanding of optimum welding parameters for various materials; study of microstructural behavior of materials during welding; evaluation of weld properties. Also, the correlation of pre-weld microstructural characteristics of materials with materials weldability and the role of filler alloys of various compositions during laser-arc hybrid welding are critical in the joining of crack-sensitive materials, such as nickel-base superalloys. However, these have received less attention.

2.4.9 Scope and Objective of the Present Work

At present, there is limited data on the joining of superalloys by laser-arc hybrid welding. The process is rarely applied to the joining of materials that are especially developed for high temperature applications including rocket engines, and aero and land based gas turbines. The fabrication of new turbine components and the repair of service damaged components, such as turbine blades, discs and vanes, require highly efficient welding processes. Laser welding and arc welding processes have been, and are still being, used as individual joining processes for these applications. However, information on the synergistic effect that can be produced by a combination of these processes in laser-arc hybrid welding of turbine components is not yet available. As mentioned earlier, laser-arc hybrid welding has been mainly applied to joining steels and aluminum alloys. This process is yet to be commercially applied to several other materials such as nickel base

superalloys, cobalt-base superalloys and titanium alloys. This review of literature suggests that there exist vast opportunities that are yet to be explored based on the current state of laser-arc hybrid welding. However, the mere application of laser-arc hybrid welding does not guarantee the elimination of the inherent weldability problem encountered during fusion welding of precipitation strengthened nickel-base superalloys, which is the heat-affected zone (HAZ) liquation cracking.

This research was initiated to perform a systematic and comprehensive study of the cracking susceptibility of nickel-base IN 738 superalloy welds made by laser-arc hybrid welding process, and how to minimize it by using a combination of

A. pre-weld microstructural modification through thermal treatment
B. the application of various welding filler alloys

The results of investigations performed to achieve this objective are presented in chapter 4 of this dissertation.

CHAPTER 3

MATERIALS AND EXPERIMENTAL PROCEDURE

3.1 Materials Preparation

Cast IN 738 LC (low carbon) was received in the form of plates having dimensions of 150 mm × 50 mm × 10 mm from PCC Airfoils, Ohio, USA. The chemical composition of the as-received alloy in weight percent is listed in Table 3-1. Pairs of welding coupons of dimensions approximately 75 mm x 20 mm x 5 mm were machined from the cast plates by using a Hansvedt model DS-2 traveling wire electro-discharge machine (EDM). The coupons were given the heat treatments listed in Table 3-2. The heat treatment designated SHT is "solution heat treatment," which is the generally used pre-weld heat treatment for IN 738 superalloy. UMT (University of Manitoba heat treatment) and NUMT (New University of Manitoba heat treatments) are pre-weld heat treatments developed by the research group of Chaturvedi and Ojo to minimize cracking in IN 738 superalloy. Heat-treated coupons were surface ground by using 120 grit size SiC papers to remove surface oxides that formed on the coupons during heat treatment. The pairs of welding coupons were butt-welded by laser-arc hybrid welding technique. Five different filler alloys, namely IN 625, FM 92, IN 718, HY 282 and Rene 41 superalloys were used during welding. The compositions of the filler alloys, which were received in the form wire spools of 0.9 mm in diameter, are also included alongside the composition of the cast IN 738 base alloy in Table 3-1.

The laser-arc hybrid welds were sectioned transverse to the welding direction using the Hansvedt model DS-2 traveling wire electro-discharge machine (EDM). 10 sections were made from each of the butt welds. These were then prepared by standard metallographic

Table 3 - 1: Chemical compositions of the base alloy and filler alloys (weight percent)

Element	IN 738	Rene 41	HY 282	FM 92	IN 718	IN 625
C	0.11	0.07	0.059	0.04	0.05	0.01
Cr	16.09	18.75	19.49	16.54	17.3	21.95
Co	8.5	10.34	10.34	-	0.03	-
W	2.6	-	0.01	-	-	-
Mo	1.77	9.24	8.76	-	2.97	9.02
Nb	0.91		0.1	-	5.08	2.29
Fe	0.087	2.76	0.39	6.19	20.13	0.63
Al	3.33	1.49	1.5	-	0.5	0.26
Ti	3.44	3.15	2.21	3.02	0.94	0.20
Ta	1.77	-	0.01	-	-	1.06
Zr	0.033	-	-	-	-	-
B	0.01	0.006	0.005	-	0.004	-
Mn	-	0.04	0.03	2.16	0.03	0.03
Si	-	0.04	0.05	0.05	0.05	0.05
Ni	Bal	Bal	Bal	Bal	Bal	Bal

Table 3 - 2: A list of heat treatments used

Heat Treatments	
1120^{o}C / 2 h / AC	(SHT)
1120^{o}C / 2 h / AC + 1025^{o}C / 16 h / WQ	(UMT)
1120^{o}C / 2 h / WQ + 1120^{o}C / 24 h / FC	(NUMT)
1120^{o}C / 2 h / FC	
1120^{o}C / 4 h / FC	
1120^{o}C / 8 h / FC	
1120^{o}C / 12 h / FC	
1120^{o}C / 16 h / FC	
1120^{o}C / 24 h / FC	
1025^{o}C / 2 h / FC	
1180^{o}C / 2 h / FC	
1120^{o}C / 2 h / AC + 845^{o}C / 24 h / AC	(PWHT)*

AC = air-cooled, WQ = water-quenched, FC = furnace-cooled

*PWHT is the post-weld heat treatment

procedures for microstructural examination and etched electrolytically in 12 mL H_3PO_4 + 40 mL HNO_3 + 48 mL H_2SO_4 solution at 6 volts for 5 seconds. Specimens selected for electron backscattered diffraction (EBSD) -based analysis were chemo-mechanically polished by using colloidal silica solution to a surface finish of about 0.05 μm prior to analysis.

Cylindrical rods, 15 mm in length by 6 mm in diameter, for Gleeble simulation, were machined from heat-treated plates using the wire EDM. The surfaces of these specimens were also ground in order to remove surface oxides. Thermocouples were spot-welded on each of these cylindrical specimens at the axial centre for temperature control and measurement during Gleeble simulation. All simulated materials were sectioned in the radial direction at the location of the thermocouples, using the wire EDM. These were then prepared using standard metallographic techniques and electrolytically etched in 12 mL H_3PO_4 + 40 mL HNO_3 + 48 mL H_2SO_4 solution at 6 volts for 5 seconds.

3 mm diameter discs of 100 μm thickness were machined from the weld zones of selected welded coupons by the wire EDM for TEM analysis. The discs were dimpled and polished to achieve a thickness of 10 μm and surface finish of about 0.05 μm at the centre using a Gatan Model 656 Dimple Grinder. They were then ion-milled with Ar^+ for about 4 hours in a Gatan Duomill Model 691 Precision Ion Polishing System equipped with a liquid-nitrogen-cooled stage. Ion milling was started at 4.5 KeV (Ar^+) at 7 degrees glancing angle for 2 hours, and completed at 3 KeV (Ar^+) at 3 degrees glancing angle within another 2 hours.

3.2 Laser-Arc Hybrid Welding

Laser-Arc hybrid butt welding of the coupons was carried out by using a robotic fibre laser-GMAW hybrid welding system at the Centre for Aerospace Technology and Training (CATT), Standard Aero Limited, Winnipeg, Canada. The parameters used for welding are listed in Table 3-3.

3.3 Gleeble Simulation

Gleeble simulation of the thermal cycling experienced by the HAZ during welding was carried out by using a Gleeble 1500-D Thermo-Mechanical Simulation System. Simulations were performed by rapidly heating the specimens at a heating rate of $150^{o}C/s$ to temperatures ranging from $1120^{o}C$ to $1220^{o}C$ and held for different times ranging from 0.5 to 10 s, followed by air cooling.

3.4 Microscopy and Spectrometry (OM, SEM and EPMA)

The microstructures of the pre-weld, welded and Gleeble-simulated specimens were examined and analyzed by a ZEISS Axiovert 25 inverted reflected-light optical microscope (OM) equipped with a CLEMEX vision 3.0 image analyzer (Clemex Technologies Inc., Longueuil, Canada), a JEOL JSM 5900 scanning electron microscope (SEM) equipped with an Oxford (Oxford Instruments, Oxford, United Kingdom) ultrathin window energy-dispersive spectrometer (EDS) and Inca analyzing software. Further electron spectrometry of the weld fusion zone was carried out by using a CAMECA SX 100 Electron Probe Microanalyzer (EPMA).

Table 3 - 3: A list of the laser-arc hybrid welding process settings and parameters

Parameters	
Filler Wires	Rene 41 / HY 282 / IN 718 / FM 92 / IN 625
Wire Diameter	0.9 mm
Laser Power	4kW
Arc Voltage	21 V
Arc Current	52 A
Laser Focus	-2 mm
Process Ordering	Laser Leading
Relative Position of Laser and Arc	2 mm
Welding Speed	2 m/min
Wire Feed Speed	4 m/min
Trailing Gas / Flow Rate	Ar / 40 L per min
Torch Gas / Flow Rate	He / 25 L per min
Joint Gap	0.15 mm

3.5 Transmission Electron Microscopy

TEM was carried out by using a JEOL 2100 field emission gun high resolution scanning transmission electron microscope, equipped with an Oxford EDS, an electron energy loss spectrometer and a high-resolution electron microscopy image simulation software. The TEM was operated in both bright field and dark field modes. Electron energy loss spectroscopy (EELS) and selected area diffraction pattern (SADP) analysis were carried out on the TEM.

3.6 Electron Backscattered Diffraction (EBSD) Orientation Analysis

The grain structure of the fusion zone was studied by carrying out electron backscatter diffraction (EBSD) -based orientation analysis using an HKL Nordlys EBSD detector (developed by Oxford Instruments), which was attached to a Philips XL 30 Scanning Electron Microscope. The EBSD detector was equipped with Oxford Instrument HKL Technology Channel 5 suite of programs. Orientation mapping was carried out at a step size of 1.5 μm. The projection of randomly selected points on inverse pole figures (IPFs) was determined.

3.7 Thermodynamic Calculation

In order to study the solidification behaviour of the weld metal, theoretical temperature step thermodynamic calculation was performed using JMatPro [136], the materials property simulation package (developed by Sente Software Ltd., Surrey Technology Centre, Guildford, United Kingdom). Calculation was performed at a step of $5^{o}C$ for temperatures decreasing from $1400^{o}C$ to $800^{o}C$

3.8 Hardness Measurement

The hardness of the fusion zone of weldments was measured with a Buehler microhardness tester using a load of 300 g. The materials were polished to 1μm surface finish before hardness testing.

CHAPTER 4

RESULTS AND DISCUSSION

A detailed result and discussion on the study performed on laser-arc hybrid welding of IN 738 superalloy is presented in this chapter. The chapter is divided into four major sections. These are:

4.1. Microstructural Analysis of Laser-Arc Hybrid Welded Nickel-Base IN 738 Superalloy

4.2. Improvement in Laser-Arc Hybrid Weldability: The Development of a Practicable and More Effective Pre-Weld Thermal Processing Procedure

4.3. The Role of Filler Alloy Composition on Laser-Arc Hybrid Weldability

4.4. Post-Weld heat Treatment (PWHT) Behaviour of the Laser-Arc Hybrid Welded Material

4.1 Microstructural Analysis of Laser-Arc Hybrid Welded Nickel-Base IN 738 Superalloy

4.1.1 Introduction

In this section, the microstructural response of IN 738 superalloy to laser-arc hybrid welding is discussed in details. The microstructures of the pre-weld heat treated materials are discussed first, followed by fusion zone (FZ) microstructural characteristics. The HAZ microstructure is also discussed and a major factor that needs to be addressed in order to enhance the applicability of laser-arc hybrid welding for joining IN 738 superalloy is identified.

4.1.2 Microstructural Analysis of Pre-Weld Heat Treated Materials

Specimens of IN 738 superalloy were given SHT (1120^{o}C/ 2h/ air-cool), UMT (1120^{o}C/ 2h/ air-cool + 1025^{o}C/ 16h/ water quench) and NUMT (1120^{o}C/ 2h/ water quench + 1120^{o}C/ 24h/ / furnace cool) pre-weld heat treatments, as described in Section 3.1. SEM micrographs of the pre-weld SHT IN 738 superalloy (Figure 4-1a) show a bimodal distribution of the strengthening γ' precipitates, consisting of regular coarse primary γ' precipitates (with sizes ranging between 0.4 and 0.8 μm) and fine spherical secondary γ' precipitates (about 0.1 μm in diameter). MC carbides and γ-γ' eutectics, which usually form during casting of the alloy, were found to persist during the SHT treatment (Figure 4-1a). In addition to MC carbides, Zr-rich particles were also observed in the pre-weld material (Figures 4-1b, 4-1c and 4-1d). These Zr-rich particles, containing sulphur, have been previously identified as M_2SC sulphocarbides in IN 738 superalloy [26]. Further analysis of the pre-weld SHT material revealed the presence of Mo-Cr-W-rich borides, usually ahead of γ-γ' eutectics and along some grain boundaries in the interdendritic regions of the alloy (Figures 4-1b, 4-1e and 4-1f). Hard refractory Mo-Cr-W-rich borides formed as a result of boron segregation to grain boundaries during heat treatment and casting, and were observed in several nickel-base superalloys [135, 137].

A SEM micrograph of the pre-weld UMT material is presented in the Figure 4-2, showing a single-mode regular distribution of γ' phase with spherical shape and up to 0.8 μm in size. In addition to the spherical γ' precipitates, coarse γ' particles of larger size, up to about 2 μm, were also distributed along some grain boundaries. MC carbides and γ-γ' eutectics that formed during casting were observed to have persisted in the alloy during the solution heat treatment and aging of the UMT treated material. In addition to MC

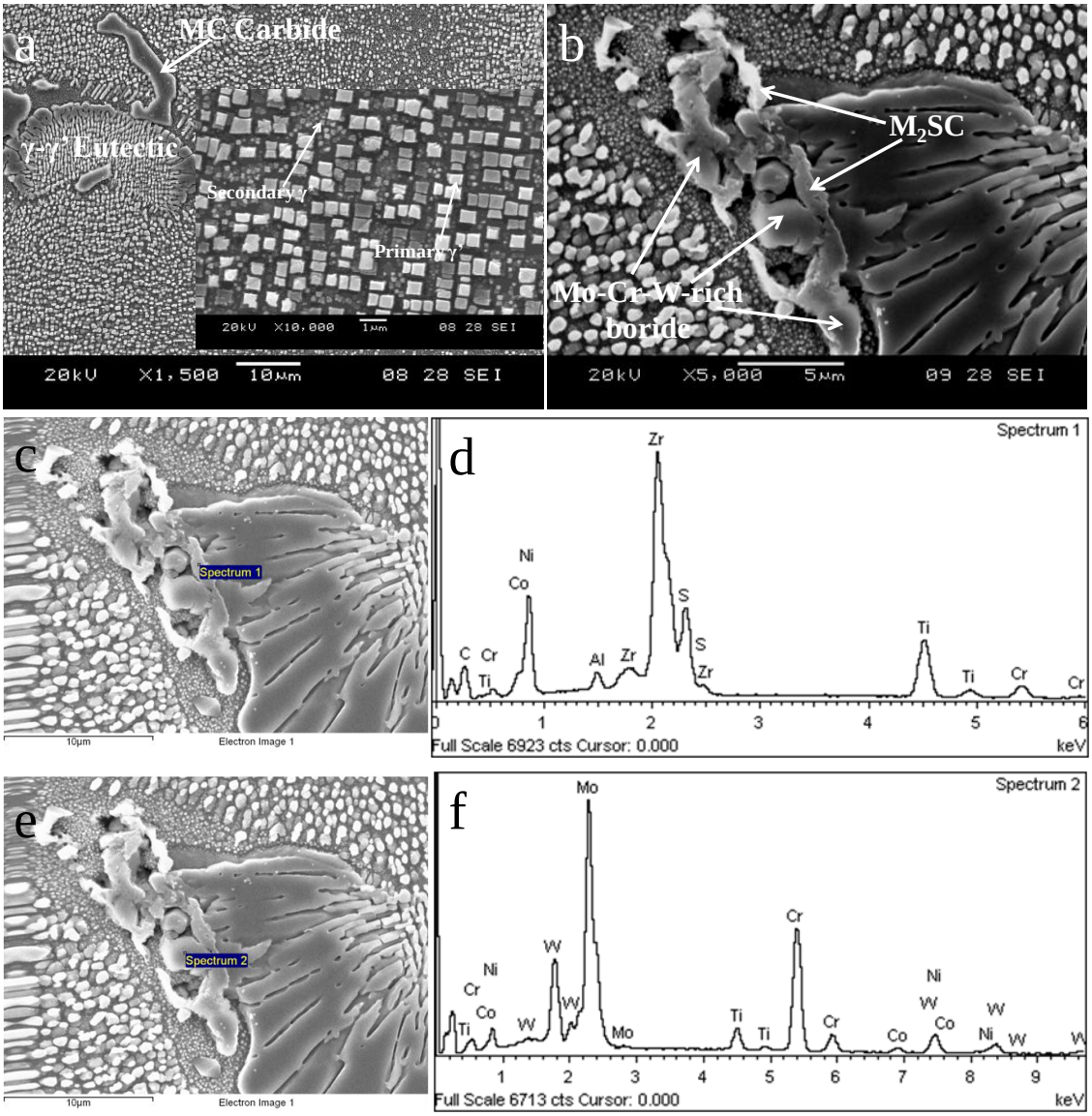

Figure 4 - 1: Microstructure of the pre-weld SHT IN 738 material, showing (a) and (b) secondary microconstituents, and SEM-EDS spectrum of (c) and (d) Zr-rich sulphocarbide, (e) and (f) Mo-Cr-W-rich boride

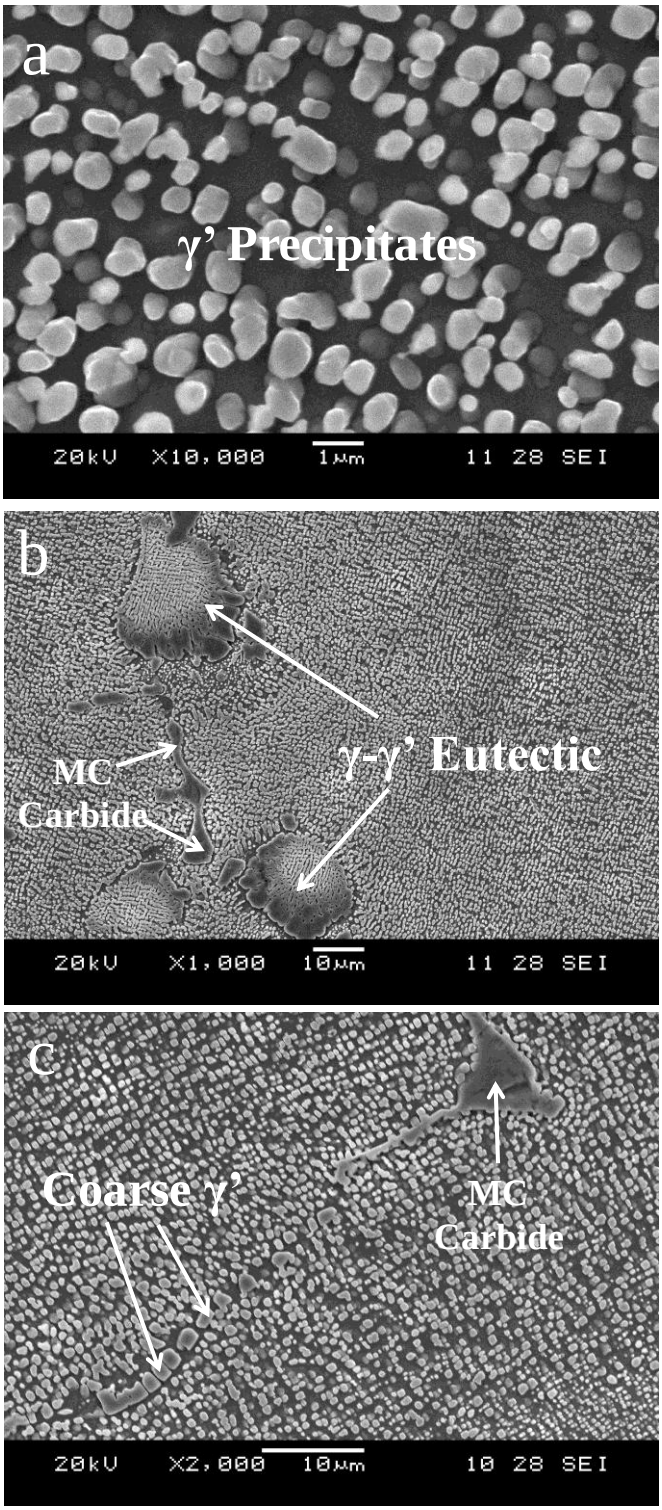

Figure 4 - 2: SEM micrographs of the pre-weld UMT-treated IN 738 superalloy, showing (a) spherical γ' precipitates (b) MC carbides and γ-γ' eutectic (c) coarse γ' precipitates

carbides, Zr-rich M_2SC sulphocarbides and borides were observed in the pre-weld UMT material (Figure 4-3). The NUMT material consisted of irregularly shaped primary γ' precipitates of sizes up to 1.2 μm and very fine secondary γ' precipitates distributed in the matrix γ phase (Figure 4-4). Coarse intergranular γ' precipitates, as well as MC carbides and γ-γ' eutectics were observed in the NUMT material.

4.1.3 General Overview of Laser-Arc Hybrid Welded Material

A general overview of the weld microstructure in the SHT-treated material is presented in the light-optical image of Figure 4-5a, showing two laser-arc hybrid butt-welded work pieces and the weld bead profile. An optical micrograph of SHT IN 738 material, bead-on-plate welded with fibre laser-beam using the same laser power, is also presented (Figure 4-5b). These figures show that laser-arc hybrid welding produced a desirable narrow weld profile in nickel-base IN 738 superalloy, similar to that usually obtained during laser beam welding. Laser-arc hybrid welding exhibited keyhole profile, as obtained in laser beam welding, and the penetration depth is strongly dependent on laser power. It has been suggested that the weld pool produced by laser-arc hybrid welding is wider than laser welds but deeper than arc welds made with the same laser and arc parameters, respectively [10]. Addition of arc to laser was also found to increase weld penetration for the same laser power [7-9]. This is consistent with observations in the present work in that the laser-arc hybrid welds were deeper than the fibre laser welds (Figure 4-5). In addition to the advantages of laser beam welding such as narrow welds, higher welding speed and deeper weld penetration that can be realized in laser-arc hybrid welding, it has also been reported that the combination of laser beam and arc results in

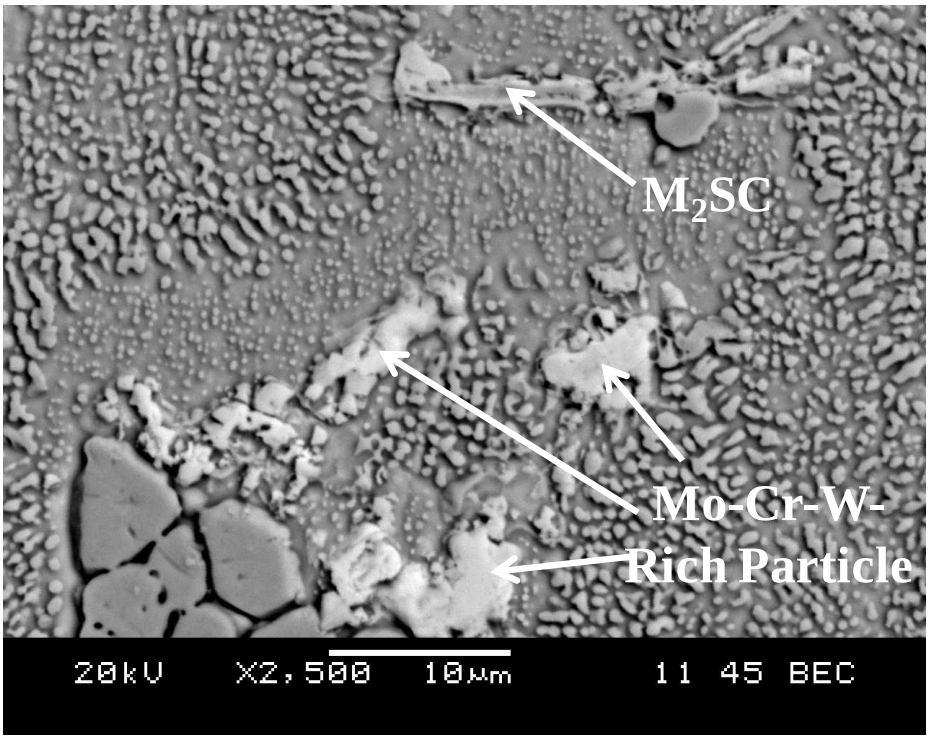

Figure 4 - 3: SEM micrograph M_2SC sulphocarbide and borides in the UMT-treated IN 738 superalloy

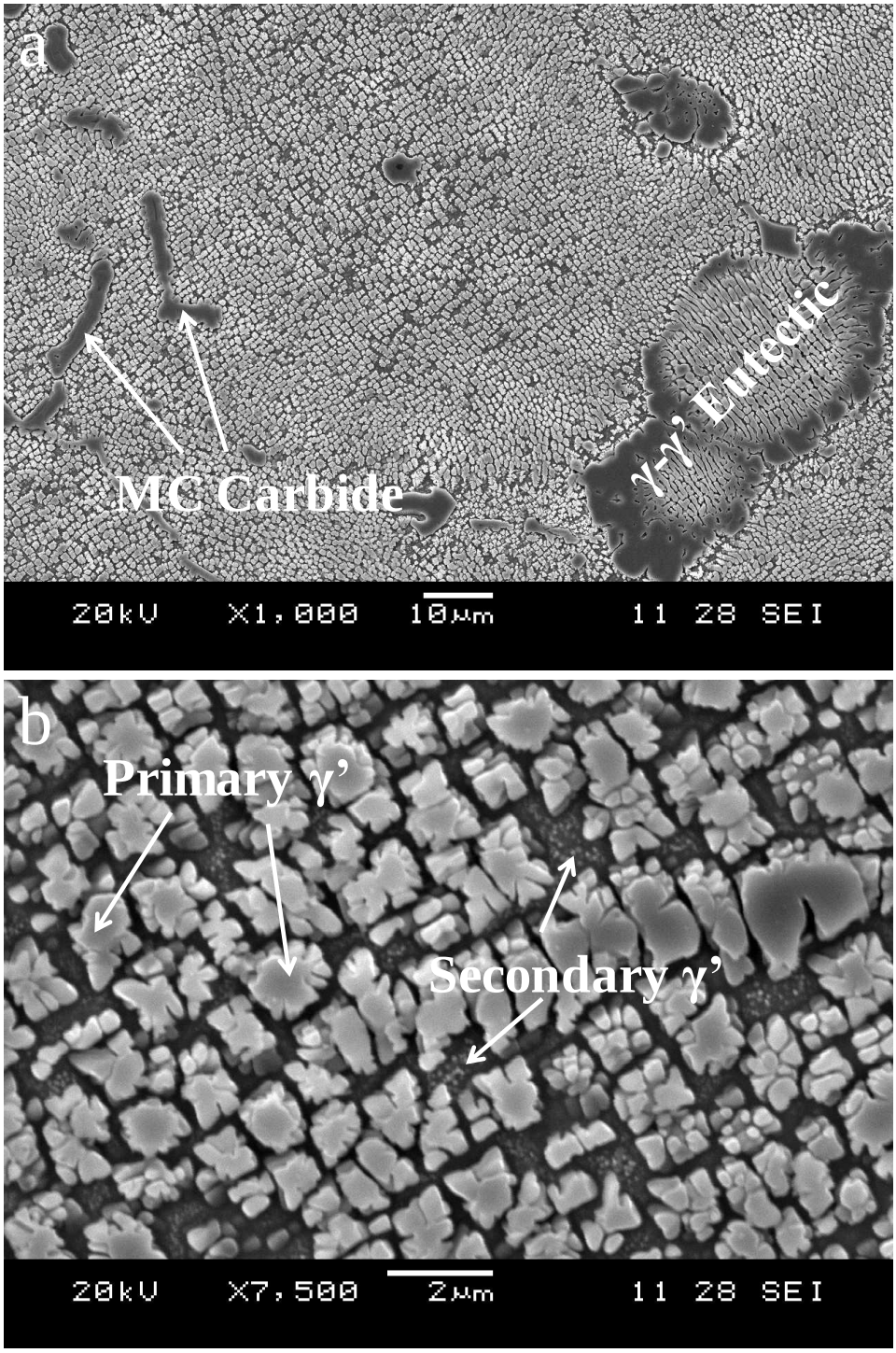

Figure 4 - 4: SEM micrographs showing various microconstituents in NUMT - treated IN 738 superalloy

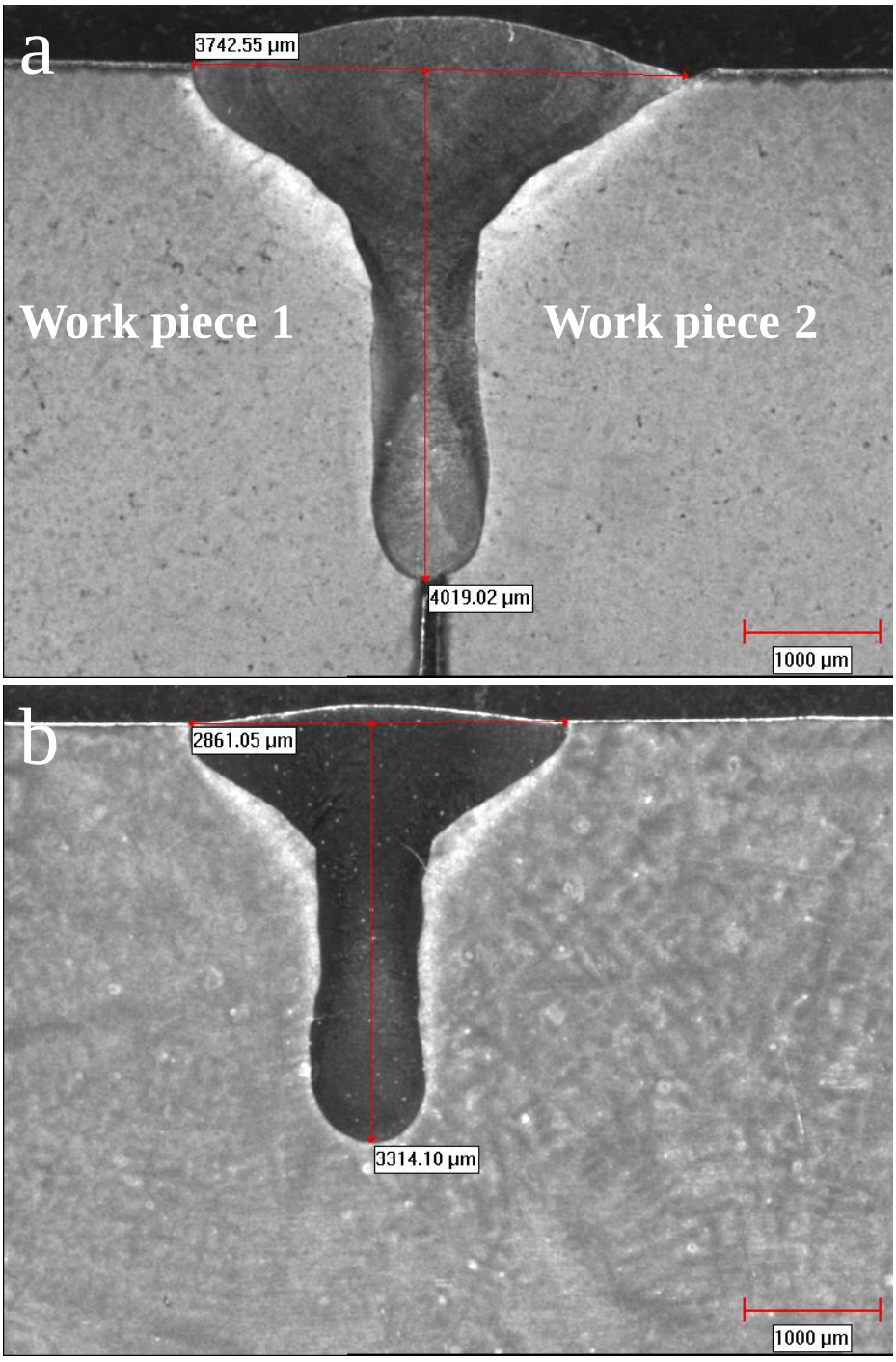

Figure 4 - 5: Light-optical images of weld profiles in SHT-treated IN 738 materials welded with the same laser power of 4kW (a) the laser-arc hybrid weld (b) bead-on-plate fibre laser weld. (Images are at the same magnification)

other advantages such as better gap bridgeability and better metallurgical properties due to welding wire addition [112, 138].

A general assessment of the laser-arc hybrid welds produced in IN 738 superalloy in the present work suggests that laser-arc hybrid welding has a great potential for improving the weldability of nickel-base superalloys. Nevertheless, safety demands on aero gas turbine components require the manufacturing of high quality welds during fabrication and repair of components. Properties and performance of materials during service are mainly controlled by the microstructure. Therefore, fusion zone (FZ) and heat-affected zone (HAZ) microstructures in the laser-arc hybrid welded IN 738 superalloy were studied and are discussed next.

4.1.4 Fusion Zone (FZ) Characteristics: Dendritic Microstructure, Elemental Partitioning and Secondary Microconstituents

An optical micrograph of the FZ of the laser-arc hybrid welded SHT-treated IN 738 superalloy that was welded with IN 718 filler alloy, showing the columnar dendritic microstructure of a region close to the fusion boundary, is presented in Figure 4-6. FZ solidification cracking was not observed in the weld metal. Previous studies have shown that higher cooling rates (shorter solidification time) in the FZ results in finer dendritic microstructure [139]. The results of the present work showed that the secondary dendrite arm spacing adjacent to the FZ boundary in the laser-arc hybrid welded IN 738 superalloy was 3.89 ± 0.41 μm. A relationship between the secondary dendrite arm spacing, d, and the cooling rate in the FZ has been expressed as [140]

$$d = KR^{n} \quad \text{.....(4-1)}$$

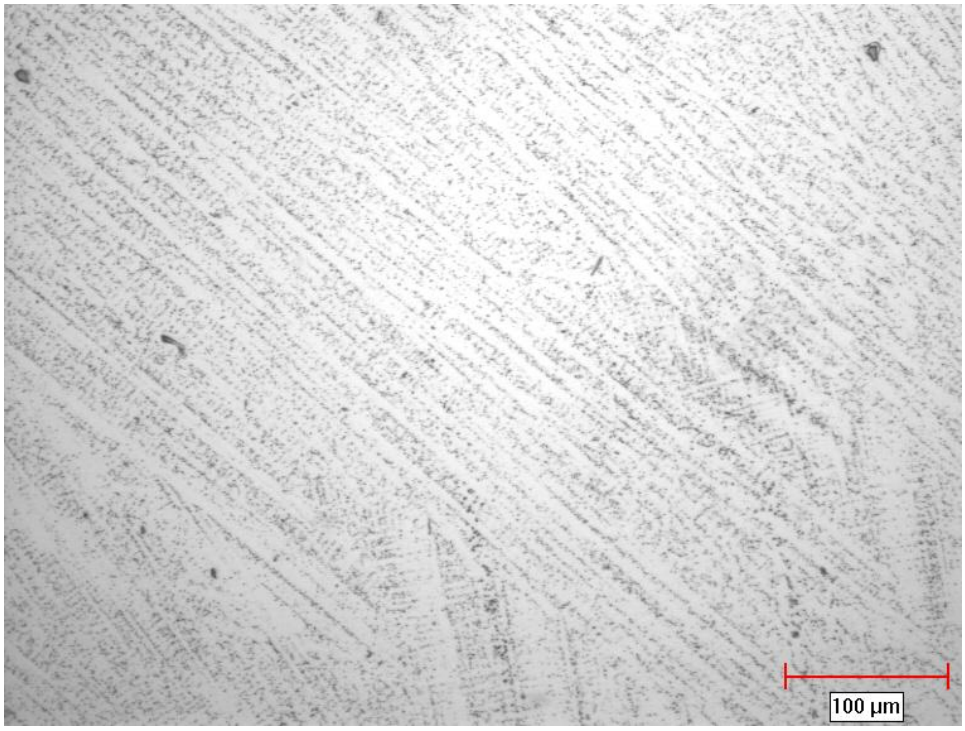

Figure 4 - 6: Light-optical image of the fusion zone

R is the cooling rate and K and n are constants, experimentally determined as 4.7×10^{-2} mm $K^{1/3}$ $S^{-1/3}$ and -0.4, respectively, for IN 738 superalloy [140]. Using this approach, the cooling rate within the FZ of the laser-arc hybrid welded IN 738 superalloy was estimated to be about 501^{o}C/s. A similar estimation for a bead-on-plate fibre laser welded IN 738 superalloy that was welded with the same laser power (4kW) showed that the cooling rate within the FZ was about 813^{o}C/s. The higher cooling rate and the relatively finer FZ dendritic microstructure in the laser welds, compared to the laser-arc hybrid welds, could be related to the amount of heat input during the two processes in that the total power for the hybrid weld was about 5kW due to the addition of about 1kW arc power. Nevertheless, the cooling rate of 501^{o}C/s within the FZ of the laser-arc hybrid welded IN 738 superalloy in the present work is significantly more rapid in comparison to the solidification rates of conventional investment cast and directionally solidified alloy ingots, which are usually below 5^{o}C/s [141]. A high solidification rate, such as experienced in the laser-arc hybrid weld, may be expected to lower the extent of microsegregation of solutes in the FZ. However, the results of the present work indicates that significant partitioning of various elements occurred between the dendrite core and interdendritic region of the FZ of the laser-arc hybrid welded IN 738 superalloy during welding, which is subsequently discussed.

The weld FZ has been considered as a small casting formed under special conditions including an intensely stirred pool of liquid, high temperature gradients and rapid solidification [142, 143]. The overall FZ microstructure is strongly dependent on the partitioning of various elemental components in the weld metal during solidification. A popular model, which has been used to describe solute redistribution during weld metal

solidification in fusion welded nickel-base superalloys and other materials, is the well-known Scheil's equation, given by [144]

$$C_s = kC_o[1 - f_s]^{(k-1)} \ldots\ldots\ldots\ldots\ldots\ldots\ldots\ldots (4-2)$$

where C_s is the solute concentration in the solid at the solid-liquid interface, k is the equilibrium partition coefficient, C_o is the nominal solute concentration (which, in this case, is the nominal concentration of the weld metal), and f_s is the fraction of solid. Rapid cooling rates during solidification of weld metal, such as those experienced in the present work, could limit the extent of solute back-diffusion. Additionally, solid-state diffusion of substitutional alloying elements in the solidified austenitic γ matrix can be considered negligible under conditions typical of fusion welding [145]. These effects of negligible solute back-diffusion and solid-state diffusion have been incorporated into Scheil's equation as derived from Brody and Fleming's equation [146]. Therefore, this equation can be conveniently used to estimate elemental partitioning coefficients in the weld metal. The fraction of solid, f_s is equal to zero under local equilibrium at the start of solidification. If undercooling at the dendrite tip is also neglected, the first dendrite solid that forms from the liquid will have a composition given by $C_s = kC_o$. Consequently, if the dendrite core composition in the weld metal, C_s and the nominal composition of the weld metal, C_o are known, then the initial partition coefficients at the start of solidification can be calculated. However, although C_s can be measured directly from the dendrite core region of the FZ, another approach will be required to determine C_o due to material mixing that resulted from the addition of IN 718 welding filler wire with a different nominal composition to the IN 738 base material in the weld metal.

Assuming a complete mixing of the base metal and the filler wire metal in the FZ and given the welding speed and wire feed speed from the welding parameters, it is possible to calculate the fraction of the total FZ volume that results from the consumption of the filler wire. If S_W and S_F are the welding speed and the filler wire feed speed, respectively, and L_W and L_F are the length of weld coupon traversed and the length of filler wire consumed, respectively, at a certain time t during welding, then $t = L_W / S_W = L_F / S_F$, which gives $L_F = S_F L_W / S_W$. The total volume of filler wire, V_F consumed during time t can be expressed as

$$V_F = \pi r^2 L_F = \frac{\pi r^2 S_F L_W}{S_W} \quad \text{.....(4-3)}$$

r is the radius of the filler wire. Similarly, the total volume of the weld metal, V_W at time t can be expressed as

$$V_W = AL_W \quad \text{.....(4-4)}$$

A is the cross-sectional area of the FZ measured in the plane transverse to the welding direction. Therefore, the fraction of the total weld metal volume that results from the consumption of the filler wire, can be calculated as

$$F = \frac{V_F}{V_w} = \frac{\pi r^2 S_F}{A S_W} \quad \text{.....(4-5)}$$

This fraction of the total weld metal volume and the nominal compositions of the base metal (IN 738 superalloy) and the filler metal (IN 718 superalloy) were used to estimate C_o. The values of C_s, C_o and k are presented in Table 4-1. The result showed that Ti, Ta,

Table 4 - 1: The measured values of C_s and the calculated values of C_o and k

	Ni	**Cr**	**Al**	**Ti**	**Co**	**Ta**	**Nb**	**Mo**	**W**	**Zr**	**Fe**
C_o	59.27	16.38	2.65	2.84	6.46	1.35	1.91	2.06	1.98	0.02	4.90
C_s	56.63	16.48	2.50	2.05	6.35	0.93	1.24	1.95	2.01	0.01	5.43
k	0.96	1.01	0.94	0.72	0.98	0.69	0.65	0.95	1.02	0.50	1.11
k*	1.03	0.98	0.92	0.69	1.09	0.74	0.52	0.87	1.13	0.13	-

Note: k* are equilibrium partition coefficient values from the work of Ojo et al. [147] and are included here for reference only.

Nb, Mo, Al and Zr, with $k < 1$ partitioned into interdendritic regions. Cr, Co and W with $k \approx 1$ were nearly evenly distributed between the dendrite core and the interdendritic region, while Fe partitioned into the dendrite core. A similar microsegregation pattern has been observed in the FZ of fusion welded IN 738 superalloy and other materials [143, 147-149]. Equilibrium partition coefficient values from the work of Ojo et al. on GTA welded IN 738 superalloy [147] are also included in Table 4-1 for reference purposes.

It should be noted that no attempt was made to determine the values of k for C and B due to the difficulty in quantifying low atomic number elements with sufficient accuracy. Also, extremely large acquisition times would be required to obtain statistically acceptable X-ray counts as a result of low nominal concentrations of these elements in the weld metal and small X-ray yield due to their low atomic number values. Nevertheless, it is important to discuss the partitioning behaviour of these elements due to the significant role they play in the formation of secondary microconstituents during solidification. The partition coefficient of C in alloys similar to IN 625 was determined to be approximately 0.2 [150]. Auger electron spectroscopy has also been used to experimentally confirm the partitioning of C into the interdendritic region [151]. Additionally, binary Ni-X phase diagrams suggests $k < 1$ for C and B in nickel [152]. Therefore, it is reasonable to assume that C and B partitioned into the interdendritic region during solidification of the weld metal in the present work. It should also be noted that, while partition coefficients are not necessarily constant during the entire solidification process, they are very useful in explaining the formation of secondary microconstituents in the interdendritic regions of the weld metal.

An SEM micrograph of the weld FZ microstructure in the laser-arc hybrid welded IN 738 superalloy is presented in Figure 4-7a, showing the nickel-base γ matrix phase and secondary solidification microconstituents. A higher magnification SEM image of the FZ revealed the presence of sub-micron size particles in the interdendritic regions (Figure 4-7b). SEM-EDS line scan across the interdendritic regions containing these particles (Figure 4-8) showed, qualitatively, the partitioning of C, Ti, Nb and Mo, which are known to be carbide formers in nickel-base superalloys, into the interdendritic regions. The significantly small size of these particles precludes their accurate quantitative analysis by either SEM-EDS or EPMA-WDS techniques due to the limitation imposed by the larger electron beam probe size and the resultant signal contributions from matrix elements. Therefore TEM analysis of these FZ particles was carried out. Figure 4-9a shows a bright field TEM image of an interdendritic particle, having a size of about 300 nm. Electron energy loss spectroscopy (EELS) spectrum in Figure 4-9b and selected area diffraction pattern (SADP), presented in Figures 4-9c, show that the particle is an MC-type carbide with a face-centred cubic (fcc) crystal structure and a lattice parameter of 0.446nm.

4.1.5 Fusion Zone (FZ) Characteristics: Grain Structure

It is generally known that the grain structure of the FZ can significantly affect its susceptibility to solidification cracking during welding [53]. In a system where nucleation of a grain occurs from a liquid which is in contact with a flat substrate, the energy barrier for the grain to nucleate on the substrate is given by [153]

$$\Delta G = \frac{4\pi\gamma_{LG}^3 T_m^2}{3(\Delta H_m \Delta T)^2}(2 - 3Cos\theta + Cos^3\theta) \quad \ldots\ldots(4-6)$$

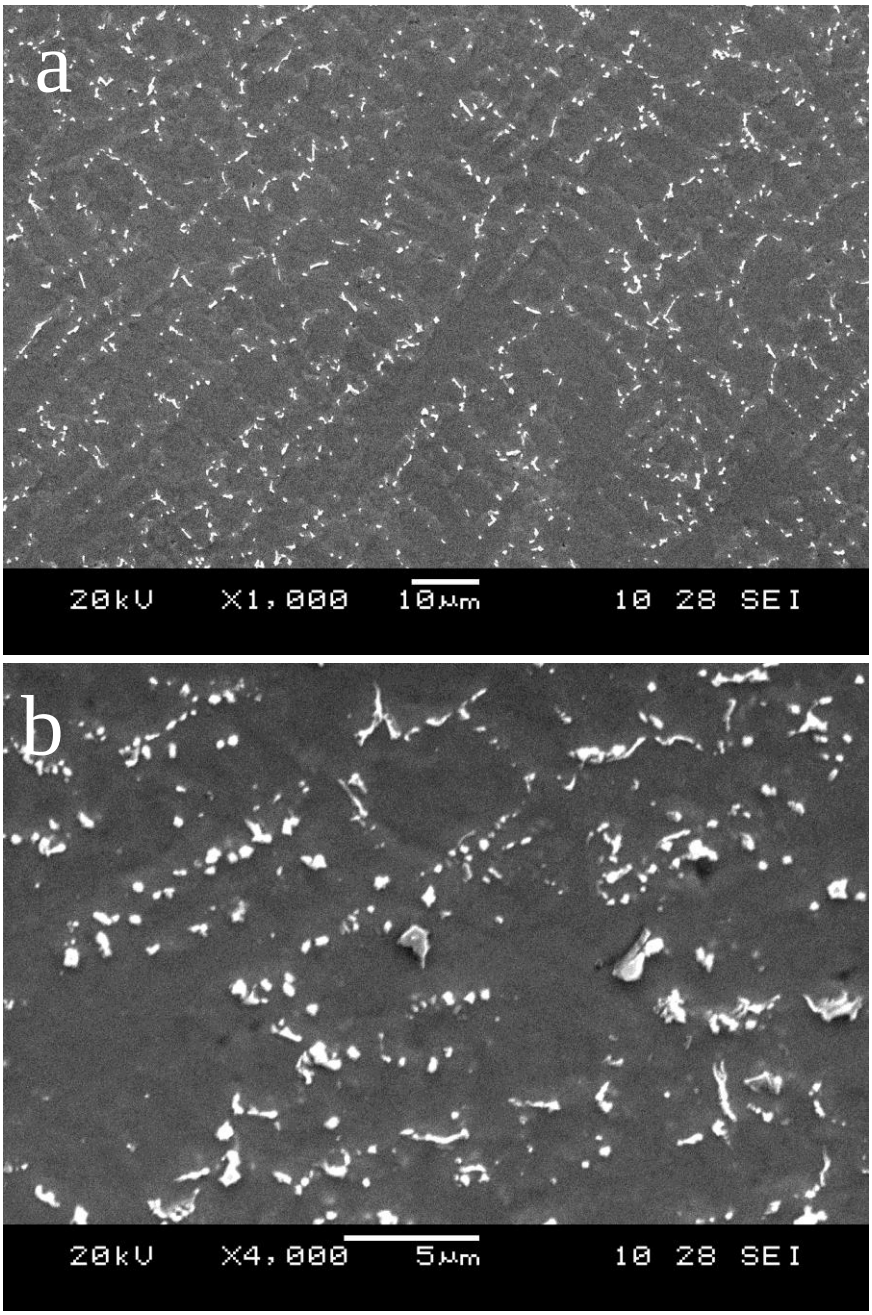

Figure 4 - 7: SEM images of the fusion zone of the laser-arc hybrid welded material that was SHT-treated

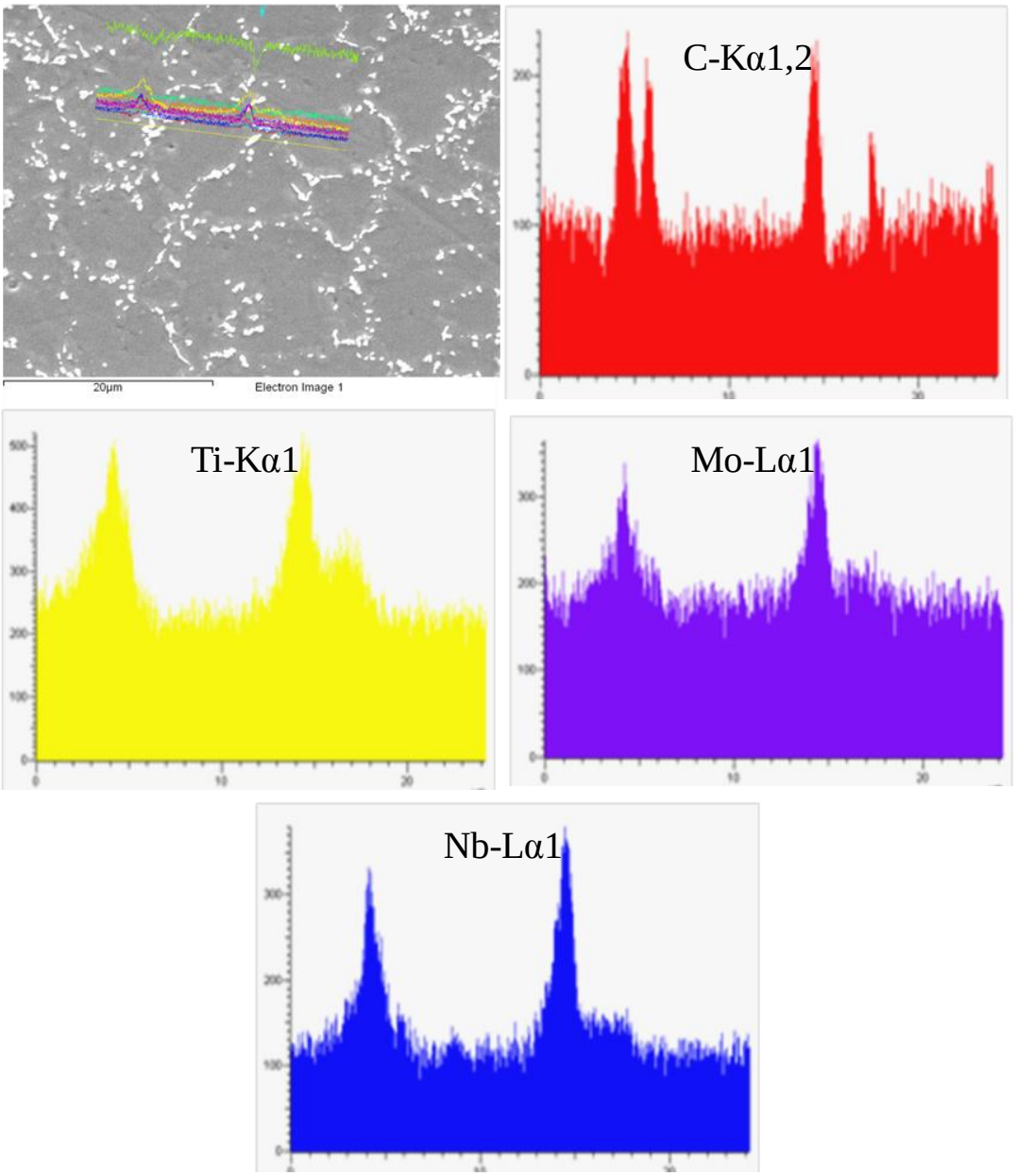

Figure 4 - 8: SEM-EDS line scan across the interdendritic regions in the fusion zone

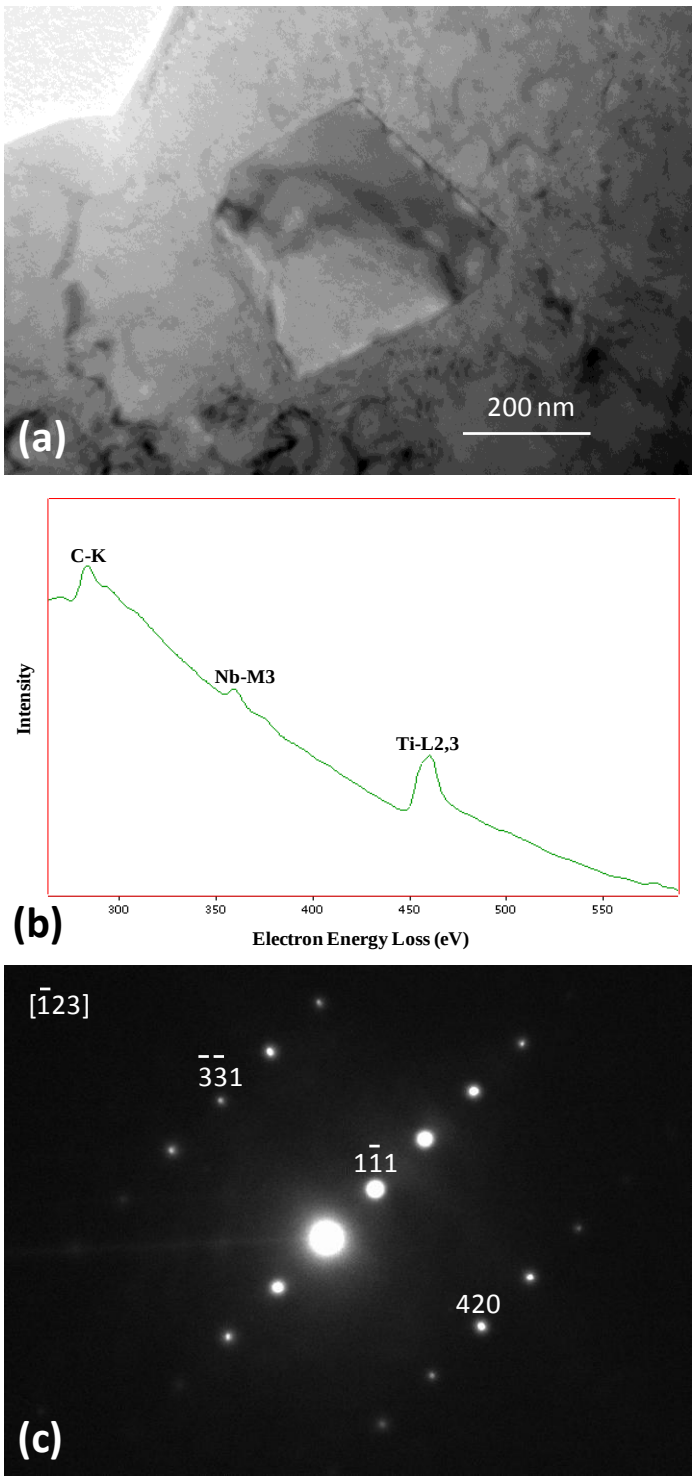

Figure 4 - 9: (a) TEM bright field image of MC-type carbide (b) EELS spectrum of the carbide (c) TEM-SADP

T_m is the equilibrium melting temperature, ΔH_m is the latent heat of melting, ΔT is the undercooling below T_m, θ is the contact angle. The geometry of the process is schematically presented (Figure 4-10), where the parameters γ_{LG}, γ_{LS} and γ_{GS} are the surface energies of the liquid-grain, liquid-substrate and grain-substrate interfaces, respectively. A complete wetting of the substrate by the liquid would result in zero contact angle ($\theta = 0$) and zero energy barrier ($\Delta G = 0$). During weld cooling, the base material at the fusion boundary acts as the substrate for nucleation. Complete wetting of the base material usually occurs, such that $\theta = 0$ and new grains nucleate easily from the liquid in contact with the substrate. If the base material and the material of the weld metal are structurally similar, atoms from the liquid can be arranged on the base material grains without any alteration in the crystallographic orientation of the substrate. Such an epitaxial nucleation results in grains with the same orientations in the base metal and the weld metal at the fusion boundary. The continuity of crystallographic orientation across fusion boundaries has been observed in some alloy systems [53, 154-156].

In the present work, epitaxial nucleation and growth of grains is expected to dominate the grain structure at the fusion boundary, since the crystal structure of the base material and the weld metal are the same and the condition for epitaxial nucleation of grains ($\theta = 0$) is fulfilled. Electron back-scattered diffraction (EBSD) - based crystallographic orientation analysis showed that grain formation at the fusion boundary was not completely characterized by epitaxial nucleation and growth, as expected. Figure 4-11a shows a SEM image of a fusion boundary in the laser-arc hybrid welded SHT-treated IN 738 superalloy with an inset whose EBSD-based grain map is presented in Figure 4-11b. Crystallographic orientation relationship between randomly selected points in the base

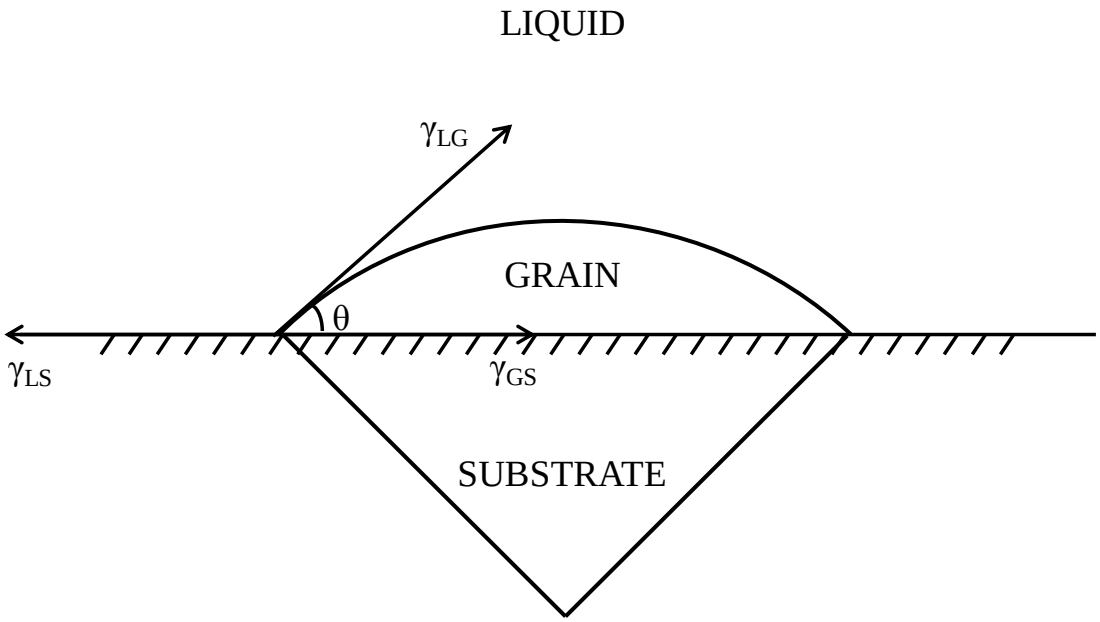

Figure 4 - 10: Schematic illustration of nucleation of a grain on a planar substrate from a liquid

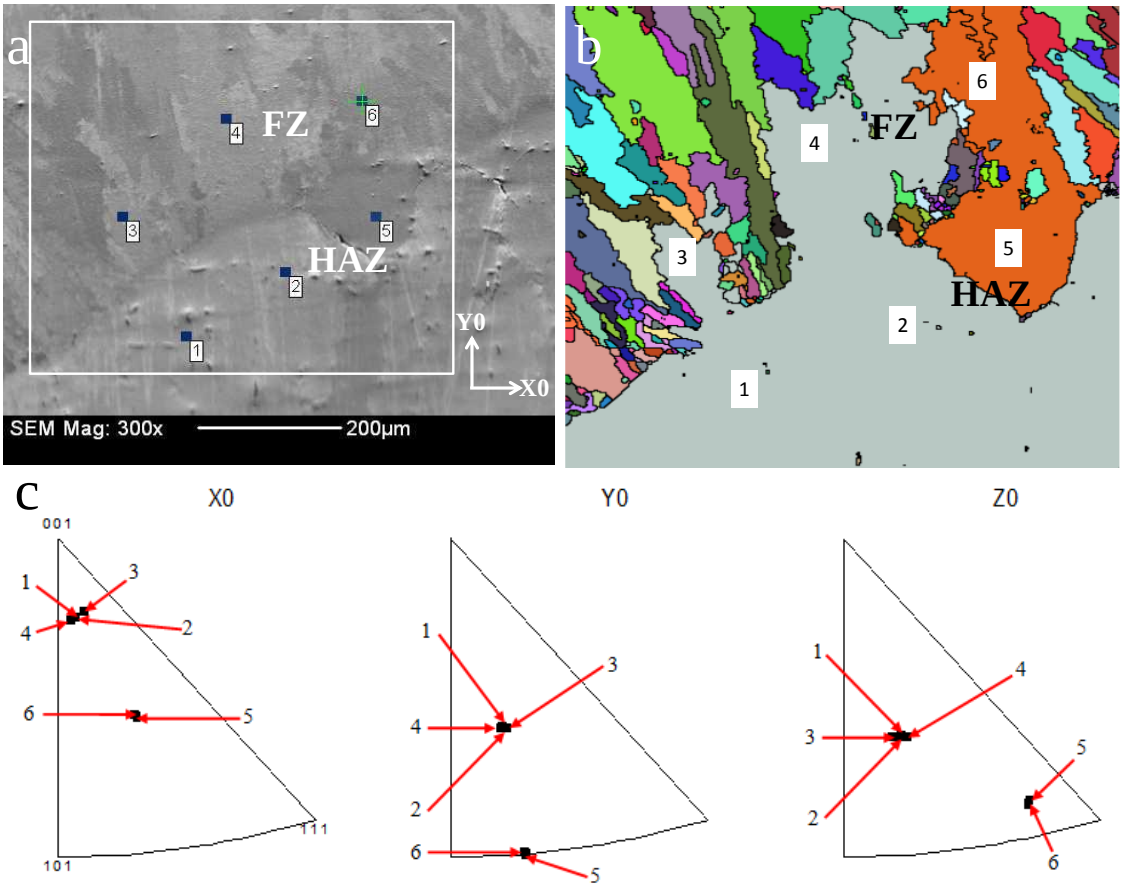

Figure 4 - 11: EBSD-based data, showing (a) forescatter SEM image of the fusion boundary, (b) a map of grains in random colours for the inset at the fusion boundary and (c) the projection of points 1-6 on inverse pole figures.

metal and the FZ was analysed by using stereographic projection of the inverse pole figures (IPF) along X0, Y0 and Z0 directions (Figure 4-11c). Here X0 and Y0 are orthogonal in the plane of the figure, as shown in Figure 4-11a, and Z0 is the direction perpendicular to the plane of the figure. Points 1, 2 and 5 are in the HAZ while points 3, 4 and 6 are in the FZ. Points 1 and 2 are in the same grain in the HAZ and point 5 is in another grain in the HAZ. Figures 4-11a and 4-11b show that the grains at points 3, 4 and 6 of the fusion zone have grown epitaxially on the grains of the HAZ. This is confirmed by Figure 4-11c which shows that points 1 and 2 (in the same grain in the HAZ) have approximately the same projection on the IPF as points 3 and 4 of the FZ for all the three directions X0, Y0 and Z0. Similarly, points 5 and 6 have the same projection on the IPF. The result also revealed that while some epitaxial nucleation of grains occurred at the fusion boundary, a significant number of grains nucleated at the boundary without any orientation relationship with the HAZ. In fact, grains that formed far away from the fusion boundary, especially at the weld centre in the upper weld region appeared equiaxed and without any orientation relationship with grains in the base metal (Figure 4-12). It has been suggested that, in principle, liquid convection in the weld pool can result in fragmentation of the dendrite tips in the mushy zone, which are then carried into the bulk weld pool [53]. The fragmented dendrites can act as nuclei for new grains if they are able to survive the temperature of the bulk weld pool, resulting in heterogeneous nucleation and growth of grains.

Additionally, some coarse MC carbides with sizes similar to the MC-type carbides of the base metal were also observed in the FZ (Figure 4-13). It is that either the particles were present in the pre-weld alloy but did not dissolve completely in the weld pool during

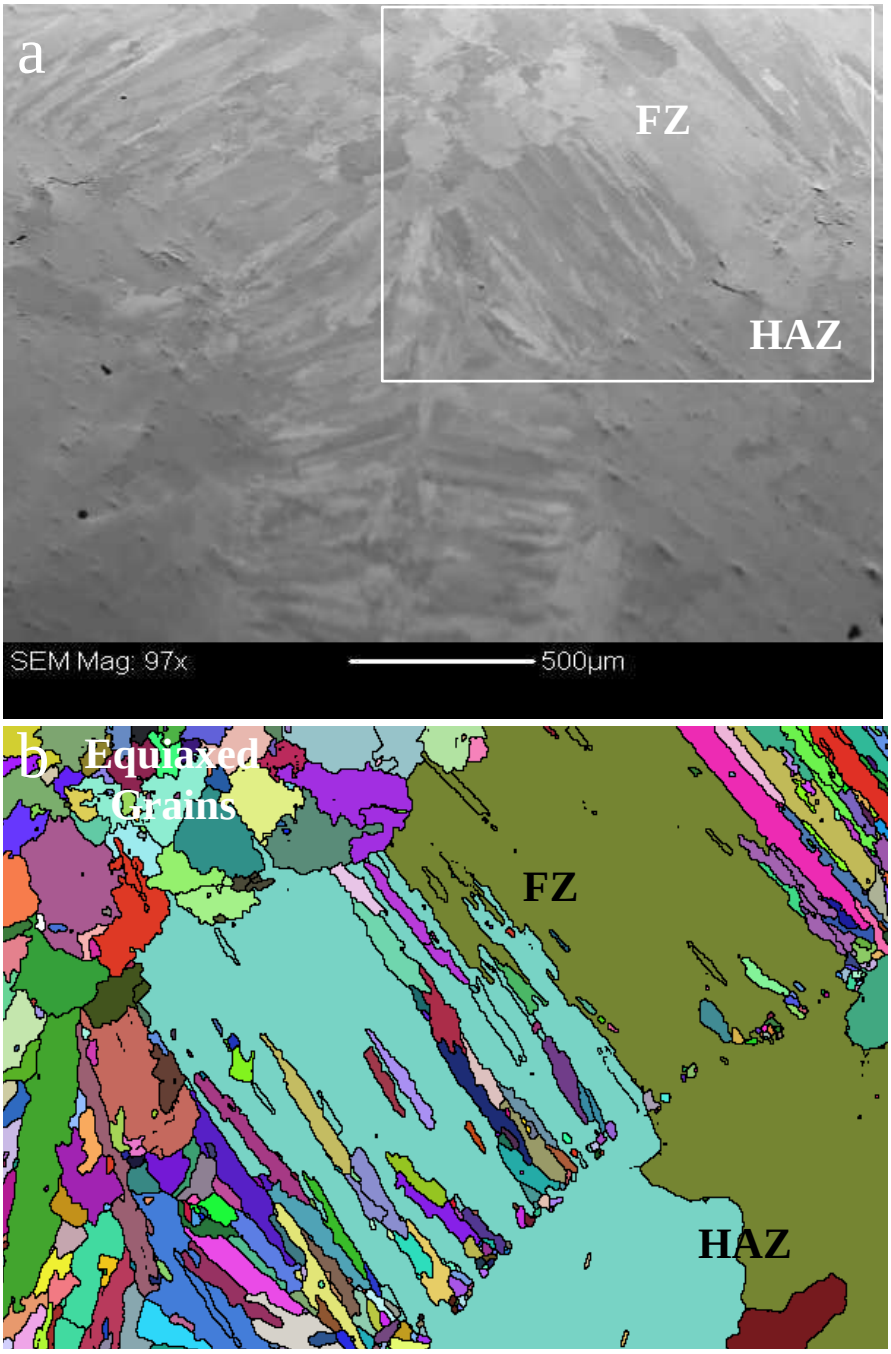

Figure 4 - 12: EBSD-based data, showing (a) low magnification forescatter SEM image of the fusion zone, (b) a map of grains in random colours for the inset in a.

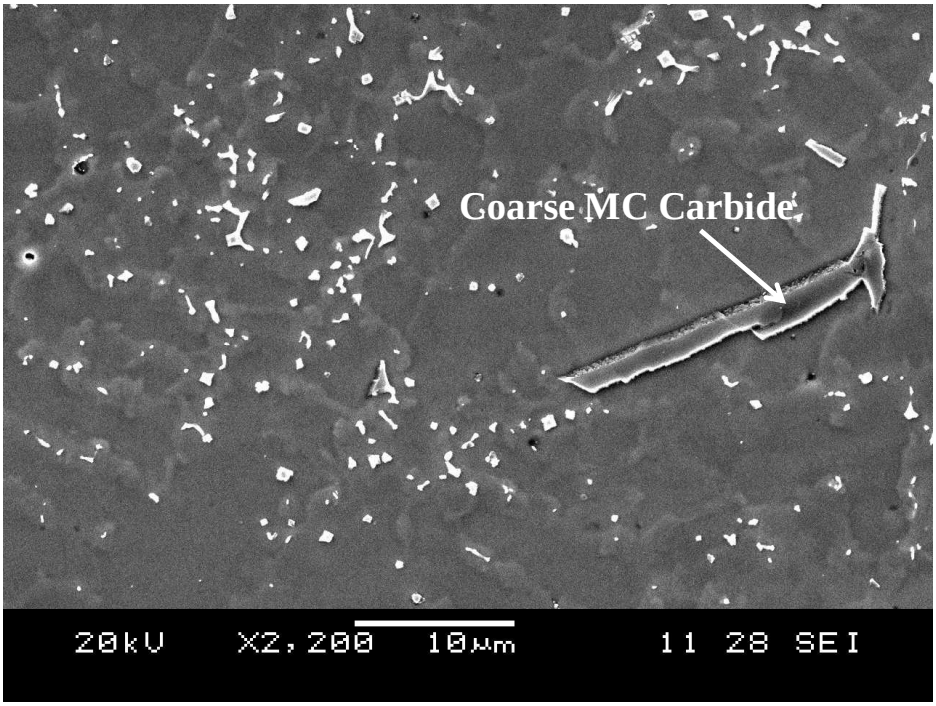

Figure 4 - 13: SEM image showing coarse MC carbide in the fusion zone

welding or the particles nucleated and grew from the weld pool prior to nucleation of the γ dendrite. Nevertheless, Differential Thermal Analysis (DTA) was used to establish that the solidification sequence of IN 738 superalloy starts by nucleation and growth of γ dendrite rather than MC carbides. It was reported that some primary MC-type carbides can be stable and remain in the melt above the liquidus temperature of the alloy, up to 1550^{o}C, for 5 - 10 minutes [157]. The primary MC carbides that persisted in the weld pool during solidification can also act as nucleation sites for new grains in the FZ. Also, fine equiaxed grains, such as observed at the upper weld centre region in Figure 4-12, are suggested to be often less susceptible to solidification cracking than coarse columnar grains [61]. Formation of fine equiaxed grains at the weld centre could have contributed to the absence of FZ centreline cracking in the alloy.

4.1.6 Microstructural Analysis of the Heat-Affected Zone (HAZ)

SEM microstructural analysis of the HAZ revealed the occurrence of intergranular cracks of varying sizes, up to about 350 – 400 μm, adjacent to the fusion zone. Figure 4-14a shows a typical crack in the HAZ. While no cracks occurred exclusively in the fusion zone, the cracks that originated at the grain boundaries in the HAZ extended, occasionally, into the fusion zone. Higher magnification SEM examination revealed the occurrence of cracks ahead of liquid film migration (LFM) at the grain boundaries, suggesting that intergranular liquation preceded cracking at these boundaries as shown in Figure 4-14b. Also, re-solidified products formed along the crack paths (Figures 4-14b and 4-15), which is a common characteristic of liquation cracking. The occurrence of HAZ intergranular liquation cracking usually requires the formation of a continuous

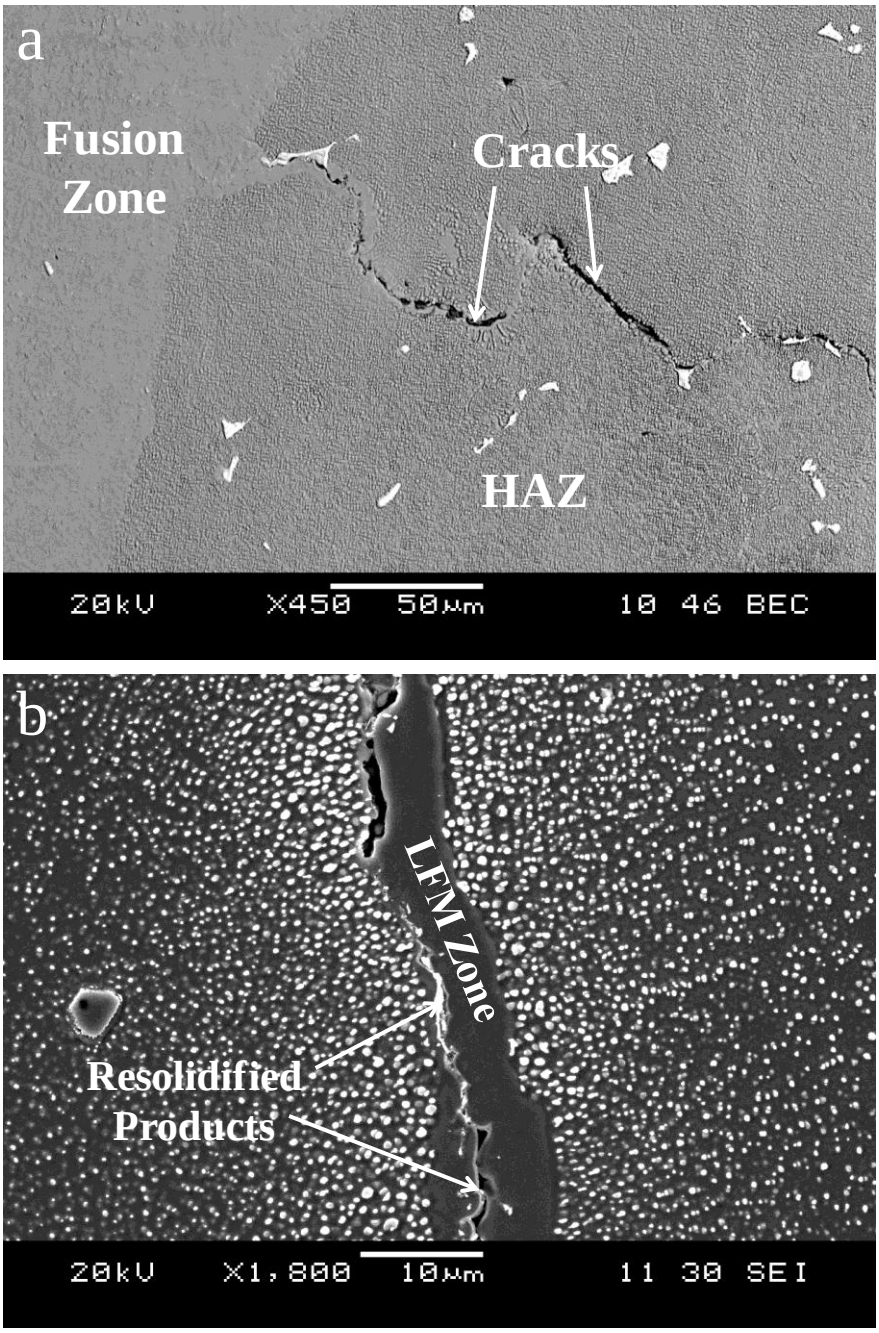

Figure 4 - 14: SEM micrographs of the laser-arc hybrid welded SHT-treated IN 738 material, showing (a) a typical HAZ crack (b) liquid film migration (LFM) and re-solidified products along a crack path

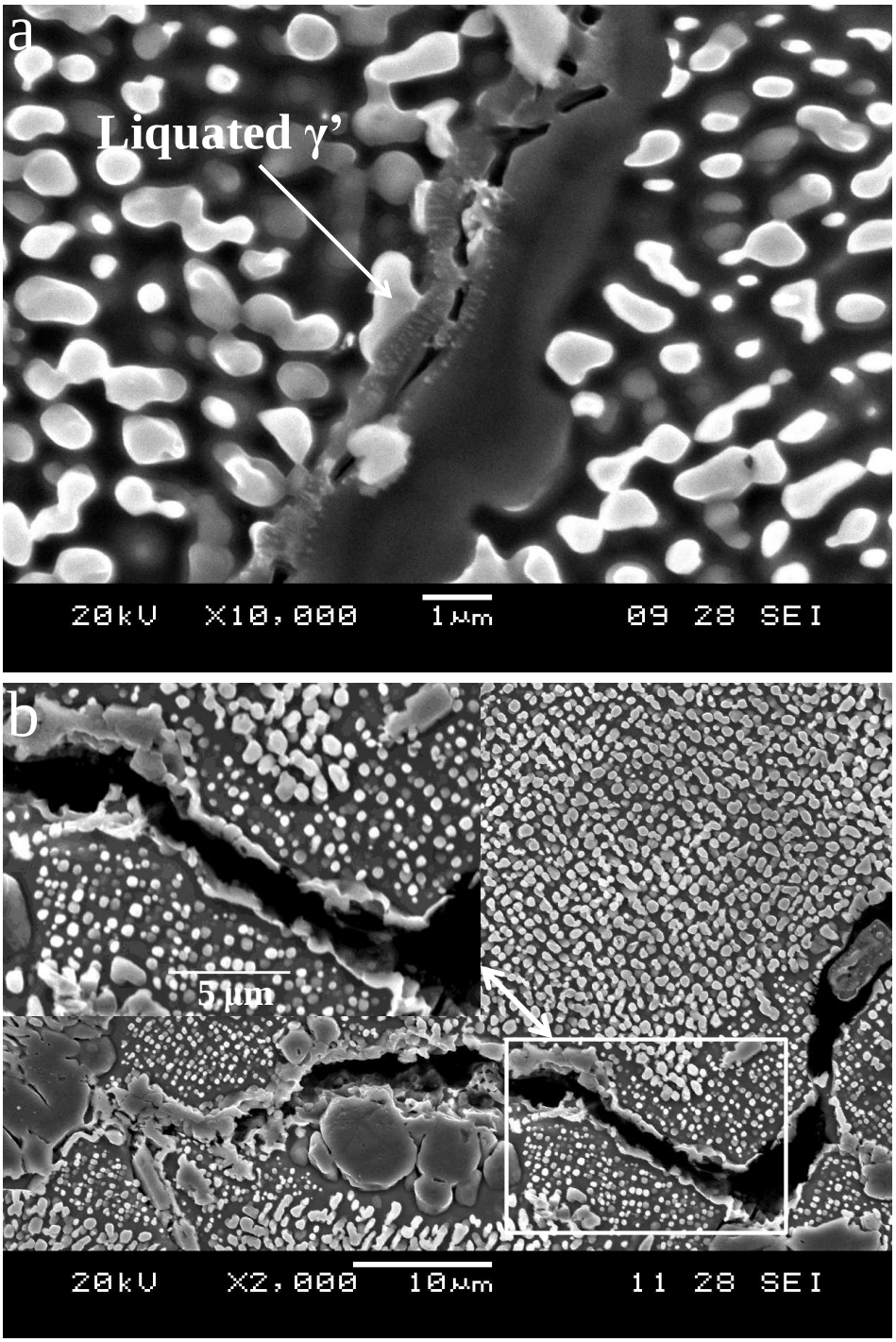

Figure 4 - 15: SEM micrographs showing the morphology of crack paths and delineation of crack paths by re-solidified products in the laser-arc hybrid welded UMT-treated IN 738 material

intergranular liquid film and the stability of the intergranular liquid film to temperatures at which thermally generated tensile stresses are sufficient to cause cracking during weld cooling [69]. A known mechanism by which intergranular liquation occurs in the HAZ during welding is constitutional liquation of various phases. Constitutional liquation was suggesting that intergranular liquation preceded cracking at these boundaries as shown in Figure 4-14b. Also, re-solidified products formed along the crack paths (Figures 4-14b and 4-15), which is a common characteristic of liquation cracking. The occurrence of HAZ intergranular liquation cracking usually requires the formation of a continuous intergranular liquid film and the stability of the intergranular liquid film to temperatures at which thermally generated tensile stresses are sufficient to cause cracking during weld cooling [69]. A known mechanism by which intergranular liquation occurs in the HAZ during welding is constitutional liquation of various phases. Constitutional liquation was first proposed by Pepe and Savage, when they observed liquation of titanium sulphide particles in 18-Ni maraging steel [64]. This phenomenon has been subsequently observed and used to explain non-equilibrium sub-solidus melting of second phases in various alloy systems during welding [65, 66, 68, 147]. In the present work, constitutional liquation of the strengthening γ' phase, γ-γ' eutectic, MC Carbides and other phases was observed to have contributed to intergranular liquation in the HAZ.

4.1.6.1 Constitutional Liquation of γ' precipitates and γ-γ' eutectic

Rapid heating of an alloy containing intermetallic particles to temperatures equal to or above the eutectic transformation temperature could result in constitutional liquation of the intermetallic particles if they survive to the eutectic temperature during heating. The γ-γ' eutectic transformation in IN 738 superalloy occurs over a range of temperatures,

which could be below 1180^{o}C, the γ' solvus temperature in IN738 superalloy [45]. The persistence of γ' precipitates to temperatures above their equilibrium solvus temperature, up to γ-γ' eutectic transformation temperature could result in their dissolution by constitutional liquation. SEM microstructural examination of γ' precipitates in the HAZ of the laser-arc hybrid welded IN 738 superalloy revealed that the particles dissolved essentially by constitutional liquation during welding (Figure 4-16a). Constitutional liquation of γ' precipitate was observed to have contributed to intergranular liquation in the HAZ (Figure 4-16b). Additionally, SEM analysis of the HAZ revealed the liquation of γ-γ' eutectics (Figure 4-16c), with microcracks observed in the vicinity of the liquated eutectics.

In order to study and understand the effect of the rapid thermal cycling experienced by the alloy in the HAZ during welding, Gleeble simulation of HAZ microstructure was performed. The results of the simulation performed at temperatures below the equilibrium solidus of the alloy (usually around 1234^{o}C [158]) revealed significant sub-solidus liquation of various phases in the alloy. For example, the SEM micrograph of Figure 4-17a shows re-solidified fine γ-γ' eutectic microconstituents that formed as a result of liquation and subsequent resolidification of intergranular γ' precipitates in a Gleeble specimen that was rapidly heated to 1180^{o}C. Figure 4-17b also shows the liquation of γ-γ' eutectics and re-solidified products ahead of the liquated eutectics in the Gleeble-simulated material. The contribution of γ' precipitates liquation to HAZ intergranular liquation in IN 738 superalloy has been reported to be one of the major factors influencing HAZ intergranular cracking in the alloy [147].

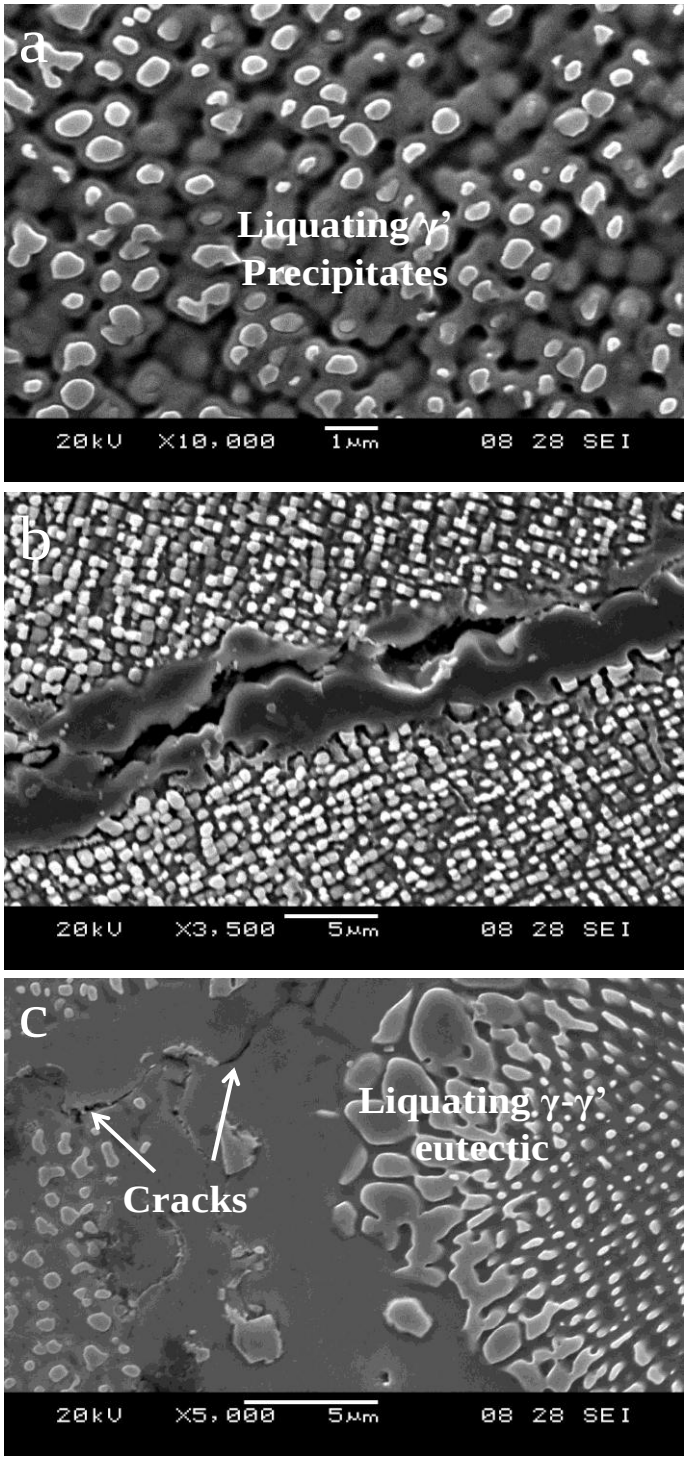

Figure 4 - 16: SEM micrographs of the welded SHT-treated IN 738 material showing (a) constitutional liquation of γ' precipitates in the HAZ (b) the contribution of constitutional liquation of γ' precipitates to intergranular liquation (c) liquation of γ-γ' eutectic

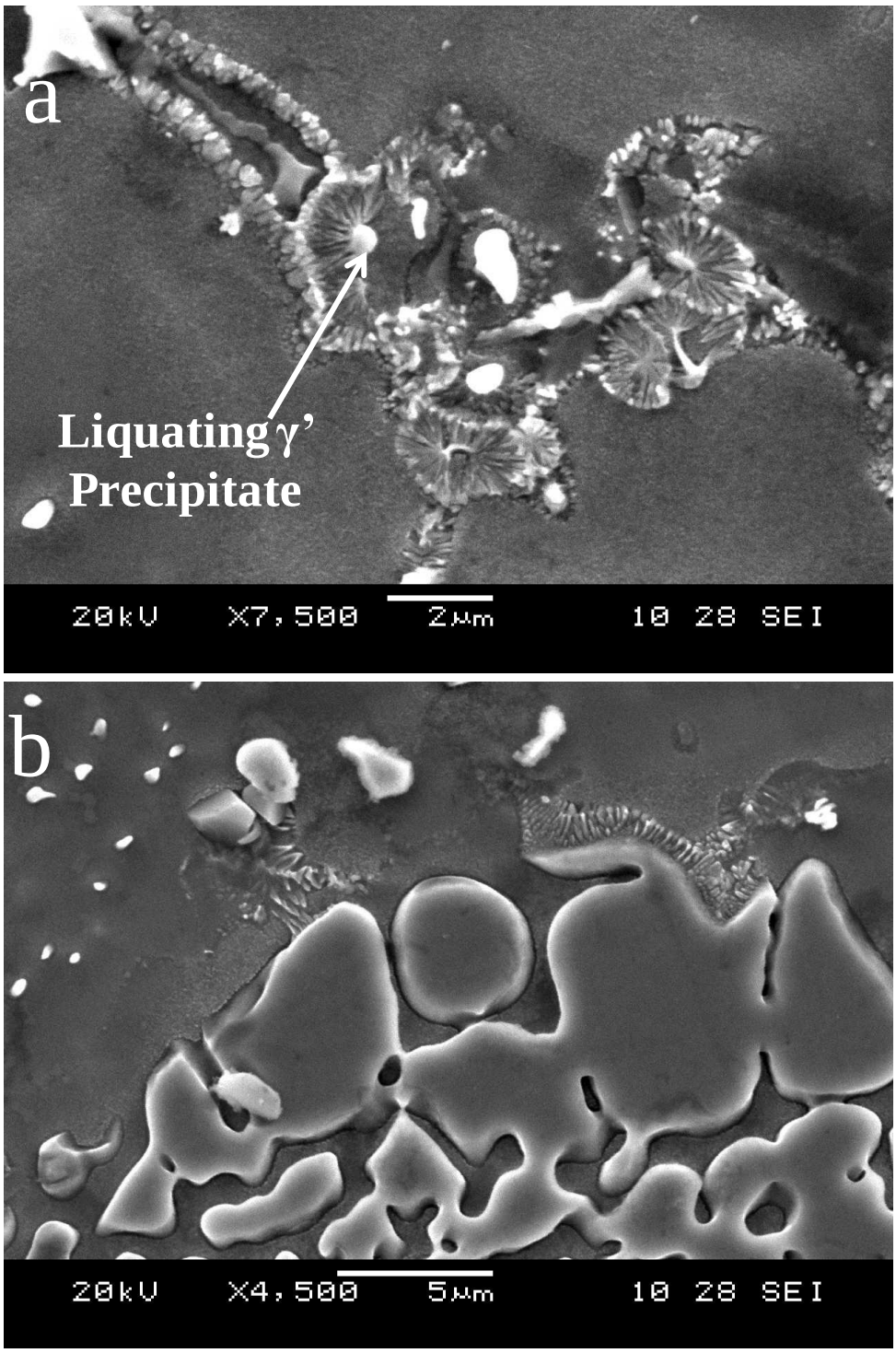

Figure 4 - 17: SEM micrographs of Gleeble-simulated SHT-treated IN 738 material that was rapidly heated to 1180^{o}C, held for 1 s and air-cooled, showing (a) liquation of γ' precipitate and formation of re-solidified fine γ-γ' eutectic (b) liquation of γ-γ' eutectic

4.1.6.2 Liquation of MC Carbides and Other Phases

Apart from constitutional liquation of γ' precipitates, SEM examination of the HAZ showed the delineation of intergranular crack paths by re-solidified products that were found to be rich in carbide-forming elements, Ti, Ta and Nb (Figure 4-18a and 4-18b), suggesting that the liquation of MC carbides and M_2SC sulphocarbides could have contributed to intergranular liquation in the HAZ. The results of Gleeble simulation in the present work showed sub-solidus liquation of M_2SC sulphocarbides and MC carbides (Figure 4-19a and 4-19b). The presence of sulphocarbides has been shown to be detrimental to tensile ductility of nickel-base superalloys [159]. In addition to carbides liquation, there were indications that borides could have also decomposed during the welding thermal cycling. Figure 4-19c is a SEM micrograph of the Gleeble material that was rapidly heated to $1180^{o}C$, showing re-solidified products that apparently formed from the decomposition of borides. SEM-EDS line scan across the re-solidified products showed the enrichment of this region in boride- and carbide-forming elements, namely, Mo, Cr, W, Nb, Zr and B (Figure 4-20). It has been suggested that an abrupt decomposition of M_2SC and boride particles during welding could cause the release of S and B atoms, which are known to be melting point depressants in nickel-base alloys [147]. The release of melting point depressants by particle decomposition and their segregation to intergranular regions during welding would lower the melting temperature of the grain boundaries. This would then contribute significantly to non-equilibrium intergranular liquation and susceptibility to HAZ intergranular cracking.

The results of the present microstructural study showed that while FZ cracking may not be a problem during laser-arc hybrid welding of IN 738 superalloy, intergranular

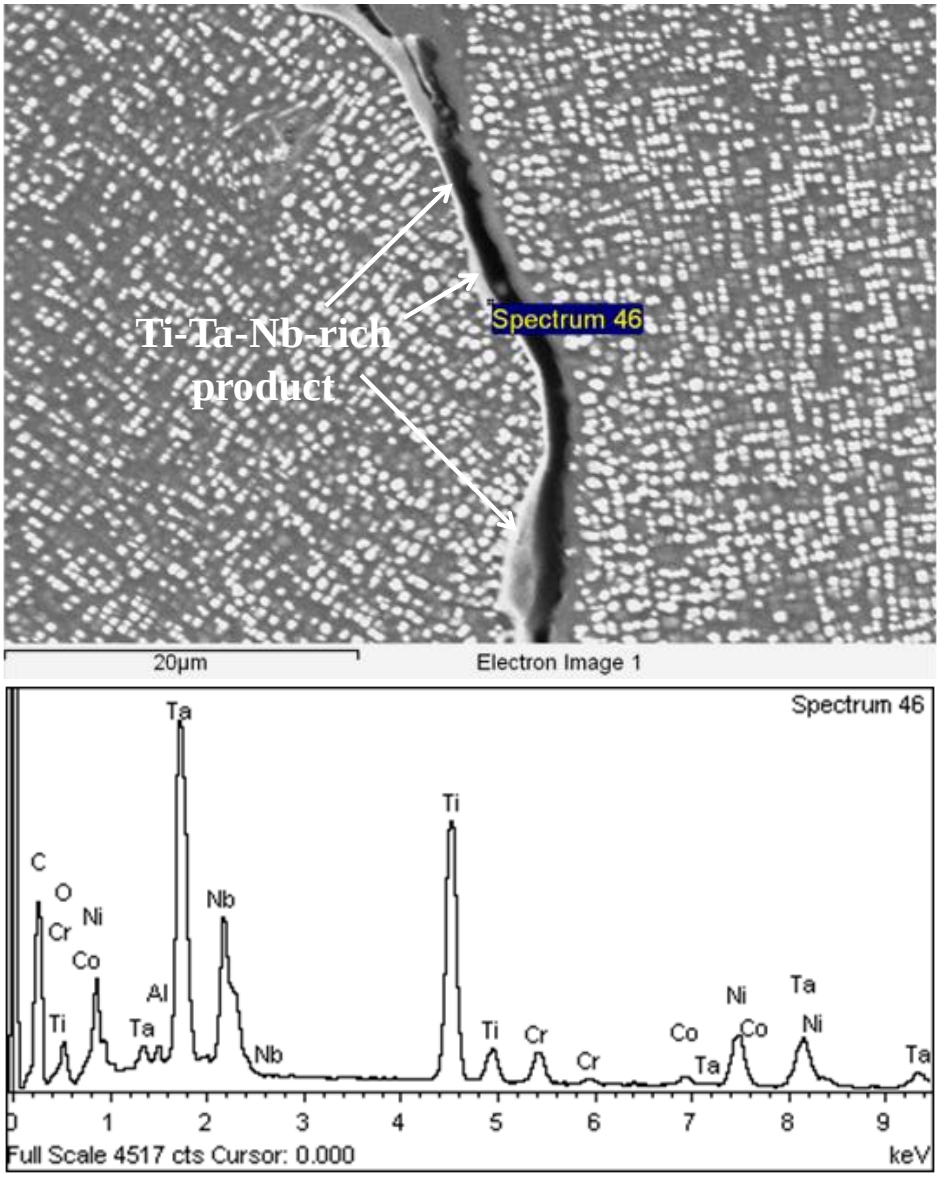

Figure 4 - 18: SEM micrographs and SEM-EDS spectrum showing products rich in carbide forming elements along a crack path in the welded SHT-treated material

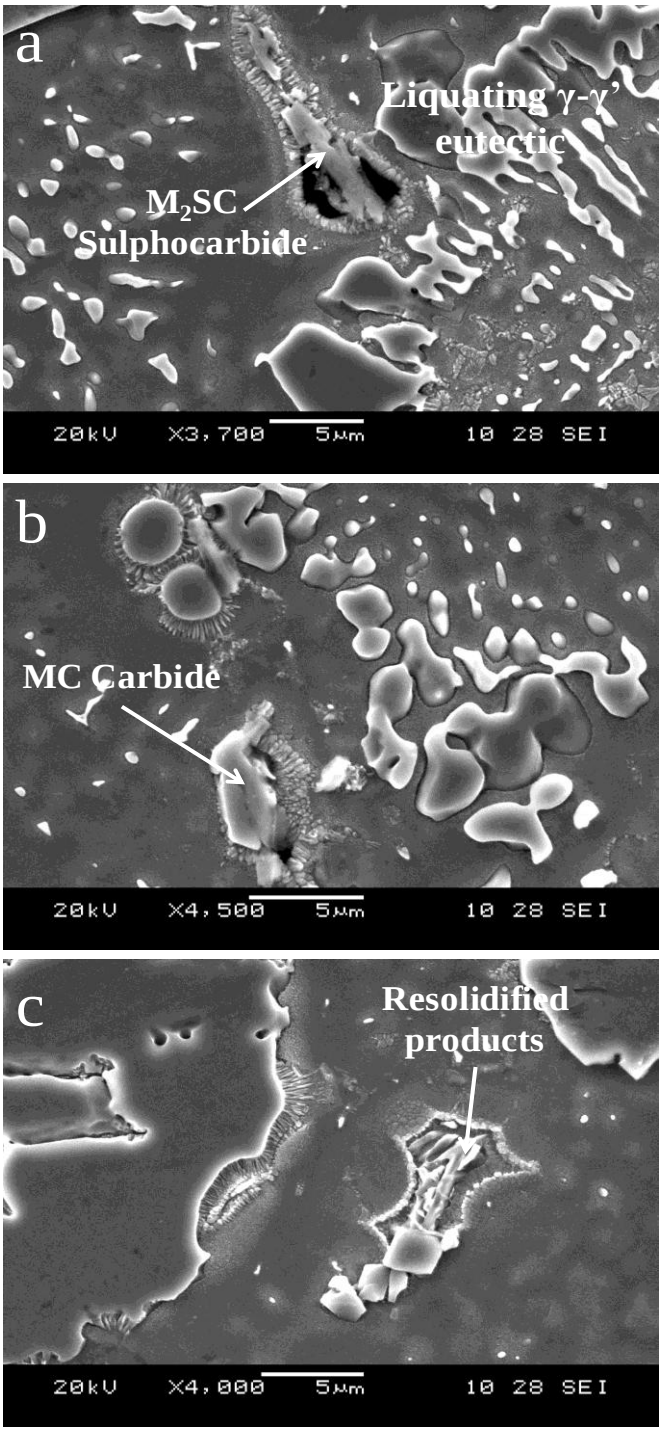

Figure 4 - 19: SEM micrographs of Gleeble-simulated SHT-treated IN 738 materials that was rapidly heated to 1180^{o}C, held for 1 s and air-cooled, showing (a) liquation of M_2SC sulphocarbide (b) liquation of MC carbide and (c) re-solidified products rich in boride forming elements

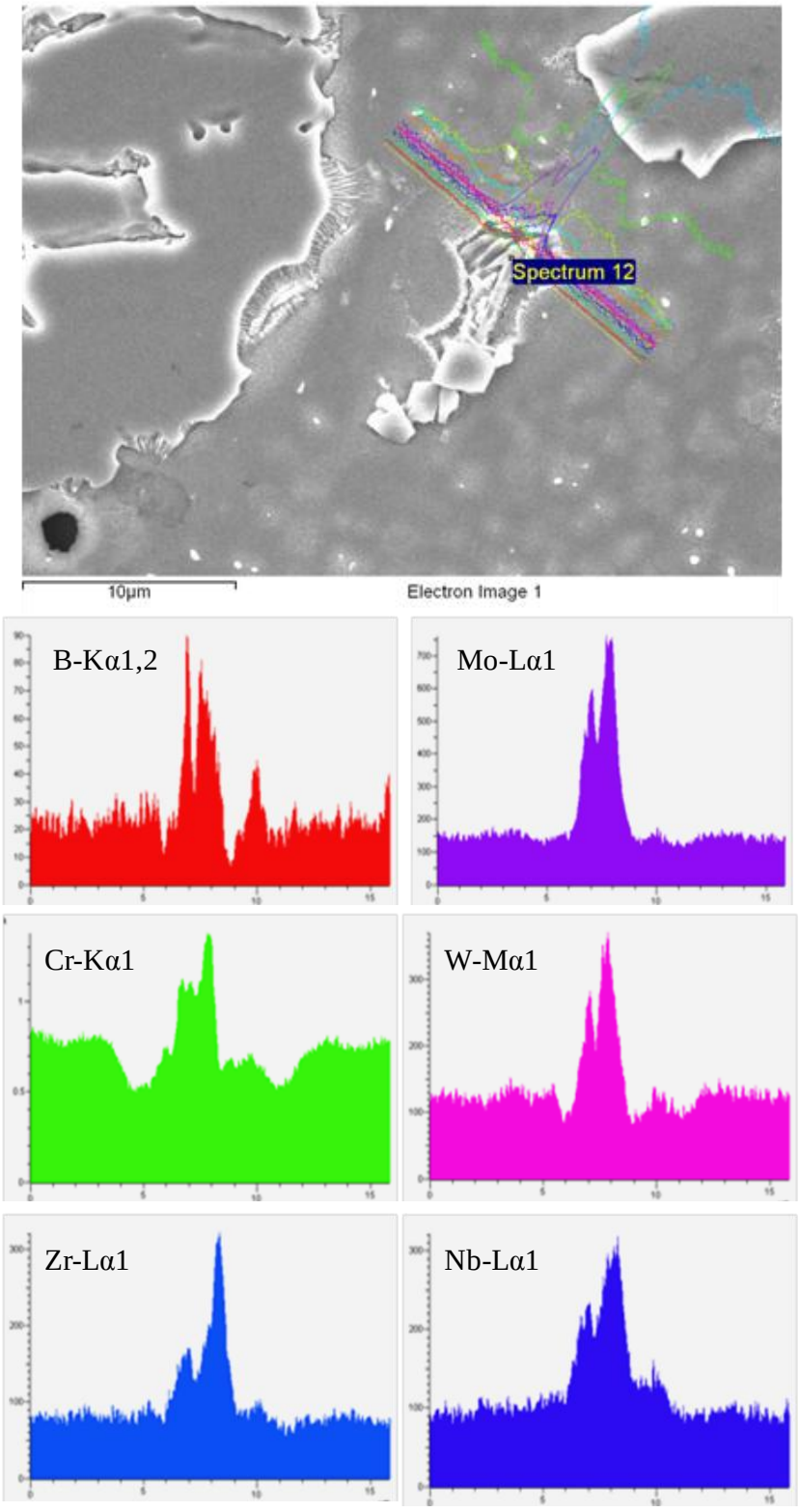

Figure 4 - 20: SEM-EDS line scan across re-solidified products in a SHT-treated Gleeble material that was rapidly heated to 1180^{o}C, held for 1 s and air-cooled

liquation, caused by the liquation of various phases, and the resultant HAZ cracking are important factors to be considered in the application of this welding technology in the joining of the superalloy. Although laser-arc hybrid welding appears promising for improving the weldability of nickel-base IN 738 superalloy, a suitable weldability improvement procedure is required in order to significantly minimize or totally eliminate HAZ cracking in the alloy. Possible weldability improvement strategies could include modification of the pre-weld microstructure and improvements in the selection of process parameters, which are considered critical for realizing the benefits of laser-arc hybrid welding.

4.2 Improvement in Laser-Arc Hybrid Weldability: The Development of a Practicable and More Effective Pre-Weld Thermal Processing Procedure

4.2.1 Introduction

In this section, the results of weldability studies performed on laser-arc hybrid welded IN 738 superalloy specimens that were subjected to various pre-weld thermal treatments are discussed. The need for developing a more industrially feasible heat treatment was identified. A major finding in this work, which was the development of a more industrially feasible pre-weld thermal processing of the alloy, is presented. The newly developed thermal treatment procedure is found to be both practicable and effective in drastically reducing HAZ intergranular cracking in IN 738 superalloy.

4.2.2 Assessment of Laser-Arc Hybrid Weldability of IN 738 Superalloy Specimens Subjected to Various Pre-Weld Thermal Processing

In the last section, HAZ intergranular liquation cracking was identified as a major limiting factor that needs to be properly addressed in the application of laser-arc hybrid welding for the joining of nickel-base IN 738 superalloy. HAZ intergranular liquation cracking is common to fusion welding processes. Previous studies have shown that pre-weld thermal processing of materials, hence, pre-weld microstructure, is critical in determining the susceptibility of precipitation strengthened nickel-base superalloys to HAZ intergranular cracking [160]. At present, the thermal treatment usually applied to IN 738 superalloy is the widely known standard solution heat treatment (SHT), which has been assessed to result in a highly crack susceptible pre-weld microstructure in the alloy [158, 161]. A thermal treatment procedure designated as UMT was found to significantly reduce HAZ intergranular liquation cracking in IN 738 superalloy during TIG welding [3,

158], which is an arc welding process. A better improvement in HAZ cracking resistance of the alloy was achieved during CO_2 laser beam welding by the application of another pre-weld heat treatment, NUMT. Laser-arc hybrid welding involves a combination of the two major welding technologies, namely, arc welding and laser welding. In the present work, a systematic study was performed to understand the microstructural response and cracking resistance of IN 738 superalloy subjected to SHT, UMT and NUMT treatments prior to laser-arc hybrid welding, which is discussed next.

Figure 4-21 shows the total crack lengths measured in 10 sections each of the welded materials. It was observed that HAZ intergranular cracking was highest in the SHT material, followed by the UMT material. The least total crack length was realized in the material that was subjected to the NUMT treatment. The reason for excessively high cracking susceptibility in SHT-treated IN 738 superalloy has been previously attributed to significant intergranular liquation in the HAZ, as was also discussed in the last section, and the inability of the base alloy to accommodate welding stress due to high hardness [3, 161]. The excessively high cracking susceptibility of the SHT material in this work is consistent with the previous findings. Although the UMT and NUMT materials showed notable improvements over the SHT material, the results revealed that the extent of cracking in the NUMT material was significantly lower than that observed in the UMT material. Therefore understanding the factors responsible for the better performance of the NUMT over UMT was considered crucial and potentially useful for developing a more effective heat treatment for the alloy. HAZ intergranular liquation cracking usually results from a competition between the formation of a continuous intergranular liquid and the development of on-cooling tensile stresses in the HAZ regions. Expansion and

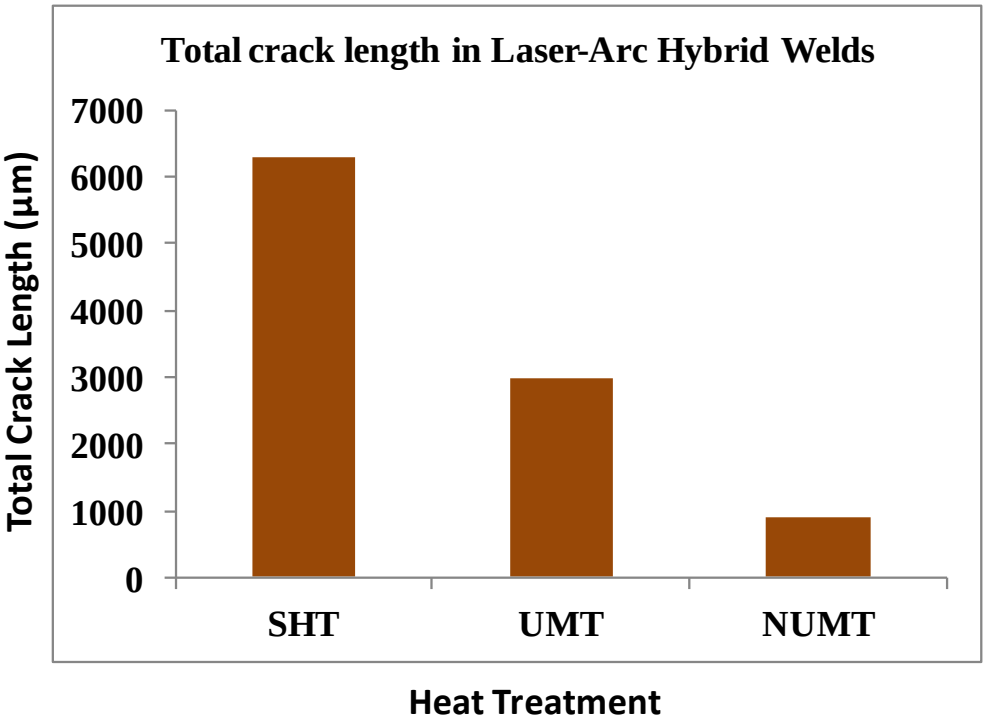

Figure 4 - 21: Total crack lengths in 10 sections each of IN 738 materials subjected to SHT, UMT and NUMT.

contraction occurs in the material when the temperature changes during welding. This is due to the temperature dependence of the elastic modulus and yield strength of the material [55]. Contraction during weld cooling usually results in the generation of on-cooling tensile stresses [52, 56, 162]. The mechanical driving force for cracking, which is the on-cooling tensile stress, is usually present during welding. Therefore, it is conceivable that reduction in the ductility of the material by the formation of continuous intergranular liquid is the major factor determining susceptibility to HAZ intergranular liquation cracking. In order to investigate the resistance of the NUMT material to HAZ cracking, a Gleeble simulation experiment was performed to evaluate intergranular liquation behaviour in the UMT and NUMT materials.

UMT and NUMT materials were rapidly heated to temperatures ranging from 1120^{o}C to 1220^{o}C at 150^{o}C/s, held for 1 s and air-cooled. A significant extent of liquation, characterized by the decomposition of borides, was first observed in the UMT material at 1150^{o}C. Re-solidified fine γ-γ' eutectic products formed in the vicinity of the decomposed borides in the UMT sample at 1150^{o}C. Borides decomposition contributed substantially to intergranular liquation in the UMT sample and significant liquation of γ' and γ-γ' eutectic occurred at all temperatures from 1150^{o}C to 1220^{o}C. Figure 4-22 shows some selected SEM micrographs of Gleeble-simulated UMT samples at various temperatures from 1150^{o}C to 1220^{o}C. Contrary to the liquation behaviour observed in the UMT material, no significant intergranular liquation was noticed at temperatures up to 1180^{o}C in the NUMT material that did not contain any boride phases. Although γ' precipitates appeared to have liquated below 1180^{o}C, the contribution of the liquation of γ' precipitates to intergranular liquation in the NUMT material was not noticeable until

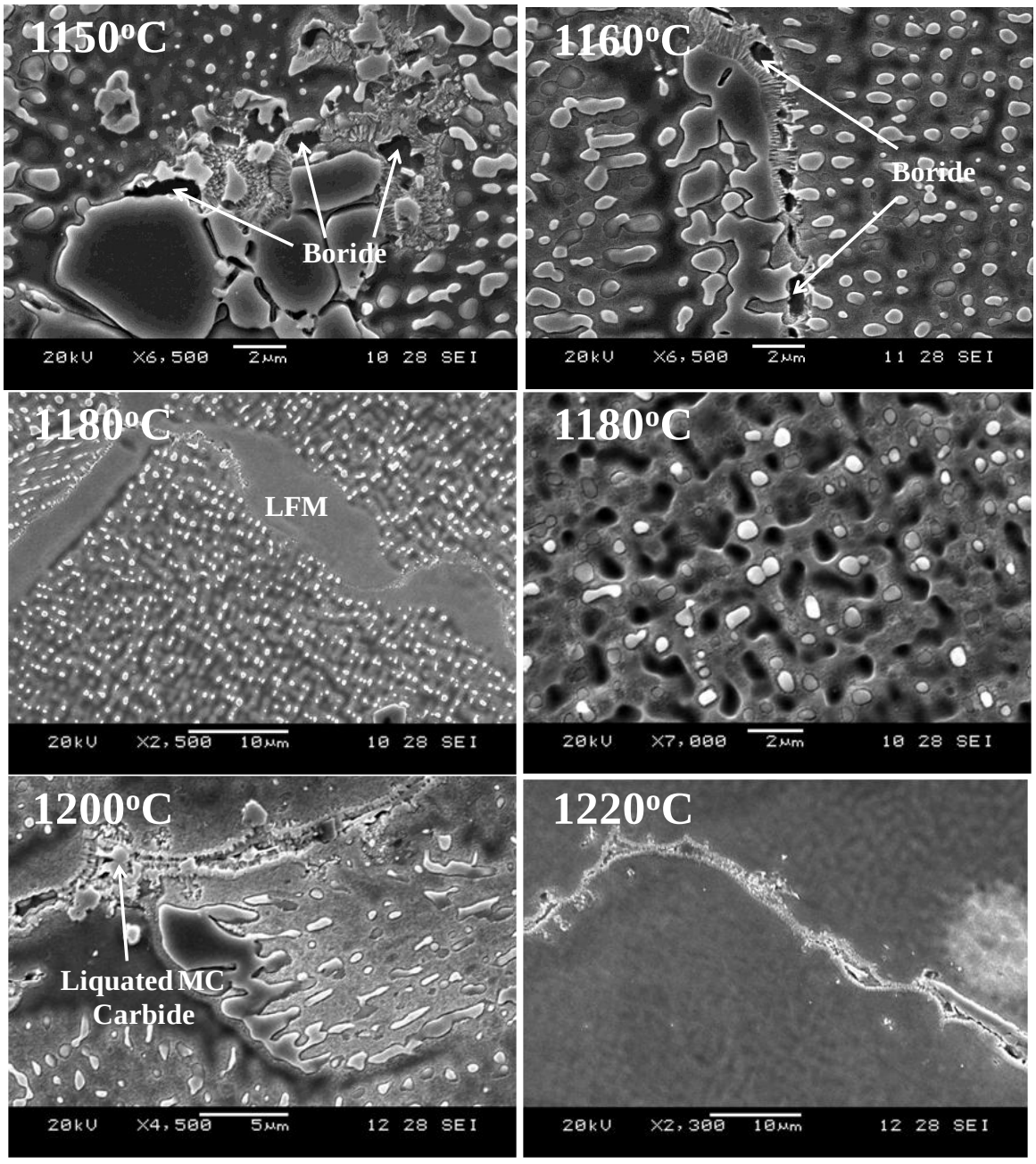

Figure 4 - 22: Selected SEM micrographs of UMT materials that were Gleeble-simulated at various temperatures.

around 1180^{o}C to 1200^{o}C (Figure 4-23). The results of this Gleeble simulation showed that intergranular liquation starts at a lower temperature in the UMT material compared to the NUMT material. This finding suggests that the temperature range over which non-equilibrium HAZ intergranular liquation occurs is larger in the UMT material compared to the NUMT material. The occurrence of significant intergranular liquation in the UMT material at lower temperatures was observed to be in close association with the decomposition of borides in the material. The decomposition of boride particles in the interdendritic regions of the UMT material, and more importantly at the grain boundaries, would have resulted in the release of elemental boron into these grain boundaries, thereby lowering their effective melting temperature. Therefore, the effectiveness of NUMT in reducing HAZ intergranular liquation cracking during welding can be related to its better resistance to intergranular liquation, especially at lower temperatures, compared to the UMT that exhibits significant liquation over a larger temperature range.

As discussed earlier, the pre-weld thermal treatment that is usually applied to IN 738 superalloy is the SHT, despite its excessively high susceptibility to HAZ intergranular cracking. Although UMT and NUMT showed better performance than SHT and the NUMT's performance is especially desirable, these heat treatments are not industrially applicable. The non-applicability of UMT and NUMT results from their requirement for water quenching (Table 3-2) as a process step during heat treatment, which is usually difficult to achieve in the aerospace industry where most of the thermal processing are performed under vacuum conditions. In order to improve the weldability of IN 738 superalloy during laser arc hybrid welding, it was necessary to develop another pre-weld thermal treatment procedure that is effective in minimizing or totally eliminating HAZ

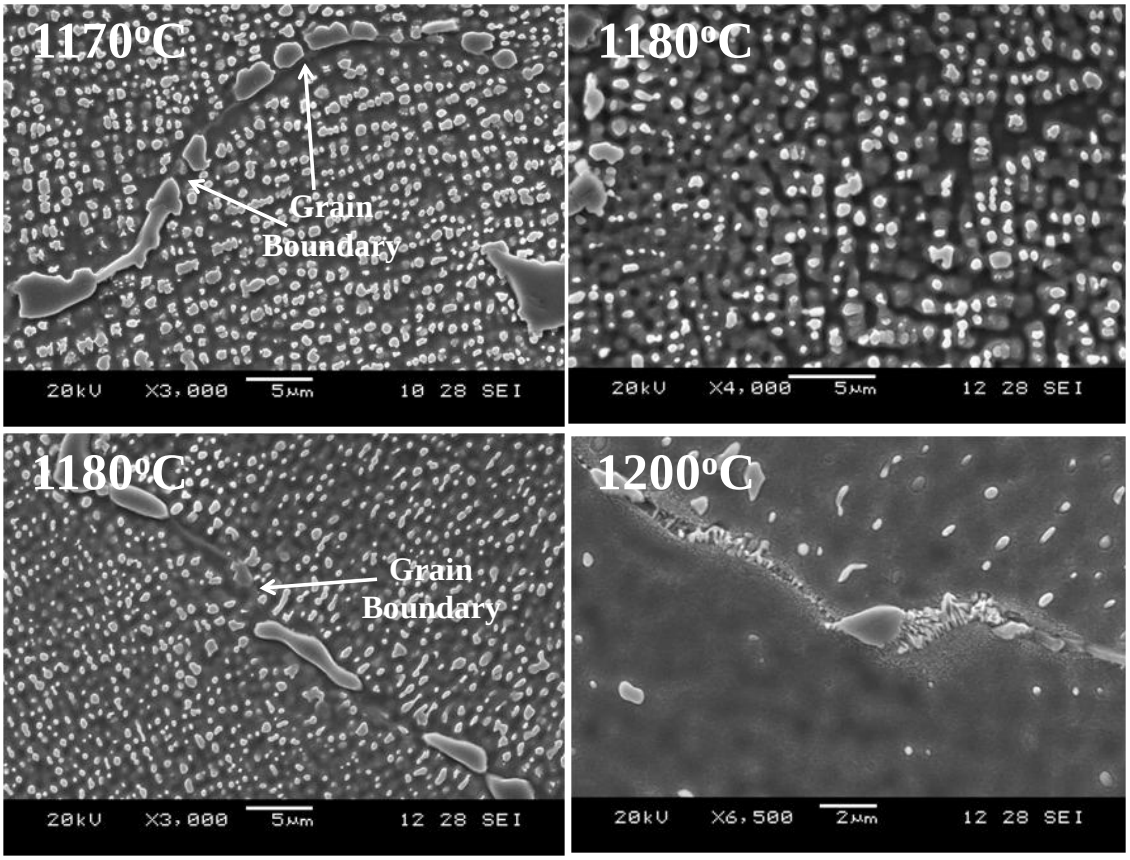

Figure 4 - 23: Selected SEM micrographs of NUMT materials that were Gleeble-simulated at various temperatures.

intergranular liquation cracking, while being industrially deployable at the same time. Such an effective and practicable heat treatment was developed in the present work and is discussed next.

4.2.3 Development of an Industrially Applicable and Effective Pre-Weld Thermal Treatment for IN 738 Superalloy

It is known that the presence of boron in a nickel-base superalloy could increase the effective solidification range of the alloy [163]. Segregation of boron to grain boundaries and other interfaces in the interdendritic regions can occur during thermal treatment prior to welding. Boron segregation is also possible during cooling of cast alloy ingots. Segregation of solutes can occur by two mechanisms, namely, equilibrium segregation [164] and non-equilibrium segregation [82-85, 165, 166]. Equilibrium segregation occurs during isothermal holding if the thermal treatment temperature is sufficiently high to promote solute diffusion. The solute atoms that diffuse to the grain boundaries are bound to the grain boundaries and the extent of segregation has been experimentally found to increase with decreasing temperature and increasing solute concentration in the matrix. Non-equilibrium segregation usually occurs during cooling from high temperature [82, 83, 166]. It requires the formation of solute-vacancy complexes and a concentration gradient of these complexes between the grain interiors and the grain boundaries. Vacancies are annihilated at grain boundaries, causing a concentration gradient of complexes. This drives the complexes to diffuse from grain interiors to grain boundaries, resulting in excessive concentration of solute atoms in the vicinity of the grain boundaries. The extent of non-equilibrium segregation depends on the starting temperature, bulk solute concentration and cooling rate [82-86, 165, 166]. Increase in

concentration of boron at grain boundaries and other interfaces as a result of boron segregation has been found to result in the formation of borides in nickel-base superalloys [22, 65]. As demonstrated by Gleeble simulation in the present work, the decomposition of borides caused extensive intergranular liquation in IN 738 superalloy and resulted in a crack-susceptible microstructure. Therefore an effective thermal treatment procedure for the alloy must consider both the elimination of boride phases present in the cast alloy and the minimization of boron segregation at grain boundaries prior to welding.

Previous studies have shown that a very fast cooling rate, such as obtained during water quenching, allows only limited time for solute-vacancy complexes to diffuse to grain boundaries during cooling [65]. This was found to minimize the extent of non-equilibrium segregation. However, in the context of developing a suitable pre-weld thermal treatment for IN 738 superalloy, water quenching is not desirable due to the difficulty of using it in industry. Another method by which non-equilibrium boron segregation can be minimized is by very slow cooling, which can cause de-segregation of already-segregated solutes to grain interior due to solute concentration gradient [81]. Karlsson et. al. [82] realized a substantial reduction in non-equilibrium boron segregation in austenitic stainless steel at very slow cooling rates of 0.25 and 0.29^{o}C, which are typical of furnace cooling conditions. This suggests that a thermal treatment procedure based on furnace cooling as the only cooling method could be both practicable and effective in minimizing non-equilibrium boron segregation during cooling from the thermal treatment temperature. Furnace cooling of nickel-base superalloys can be easily performed as an industrial process. Nevertheless, there is no current pre-weld thermal

treatment procedure developed for IN 738 superalloy that is solely based on furnace cooling. The water quenching process step in the currently existing thermal treatment procedures limits their industrial applicability. Therefore the only cooling method considered for developing a new thermal treatment procedure for IN 738 superalloy in this work was furnace cooling.

It should be noted that minimization of non-equilibrium boron segregation was not the only factor that was considered for developing a better heat treatment in this work, equilibrium segregation of boron was also considered as a possible problem if the thermal treatment temperature was not carefully chosen. It has been experimentally confirmed that equilibrium boron segregation decreases with increasing thermal treatment temperature, while non-equilibrium boron segregation increases with increasing temperature [81, 82]. Cooling from a higher temperature allows longer segregation time and a faster segregation rate than cooling from a lower temperature. Therefore, an attempt to reduce equilibrium boron segregation by increasing the heat treatment temperature could result in higher susceptibility to non-equilibrium boron segregation. In a work by Huang et. al. [81], a balance between equilibrium and non-equilibrium boron segregation was achieved around 1037^{o}C for nickel-base IN 718 superalloy. In IN 738 superalloy, 1120^{o}C was found suitable for minimizing equilibrium boron segregation and effectively preventing boride formation in the alloy [161].

In order to establish a possible balance between equilibrium and non-equilibrium boron segregation in IN 738 superalloy at 1120^{o}C, a welding experiment was set up for materials treated at 1025^{o}C, 1120^{o}C and 1180^{o}C for 2 h, followed by furnace cooling. The choice of these three temperatures was considered reasonable for two major reasons.

Firstly, under furnace cooling condition, the hardness values of the materials at the three temperatures were comparable (Figure 4-24). This suggests that the ability of the base materials to accommodate welding stress can be safely assumed to be similar. Secondly, all other phases that usually contribute to HAZ intergranular liquation, including γ' precipitates, γ-γ' eutectic and carbides, were present in the materials after the heat treatment. The cooling curve for the furnace-cooled material, treated at 1120^{o}C, in this work is presented in Figure 4-25. The initial cooling rate was estimated to be around 0.12^{o}C/s, which is in agreement with the cooling rate used by Karlsson et. al [82]. The results of the welding experiment showed that the extent of HAZ intergranular cracking was least in the material treated at 1120^{o}C (Figure 4-26). Thermal treatment of IN 738 superalloy at 1025^{o}C is known to result in formation of significant amount of boride in the alloy, due to excessive equilibrium boron segregation. The decomposition of borides, as also found in the UMT material that was treated at 1025^{o}C in this work, could significantly increase the extent of intergranular liquation. Also, at 1180^{o}C where equilibrium segregation of boron is expected to be minimal, non-equilibrium segregation could be the controlling mechanism due to the higher thermal treatment temperature. Thermal treatment at 1120^{o}C appeared to have provided a balance between the two competing solute segregation mechanisms. Therefore, 1120^{o}C and furnace cooling were chosen as the candidate temperature and cooling method, respectively, for the new heat treatment.

The results of the welding experiment for the furnace-cooled materials showed that, although the least cracking was obtained in the material that was treated at 1120^{o}C for 2 h, the extent of HAZ cracking in this material was still unacceptably high. SEM

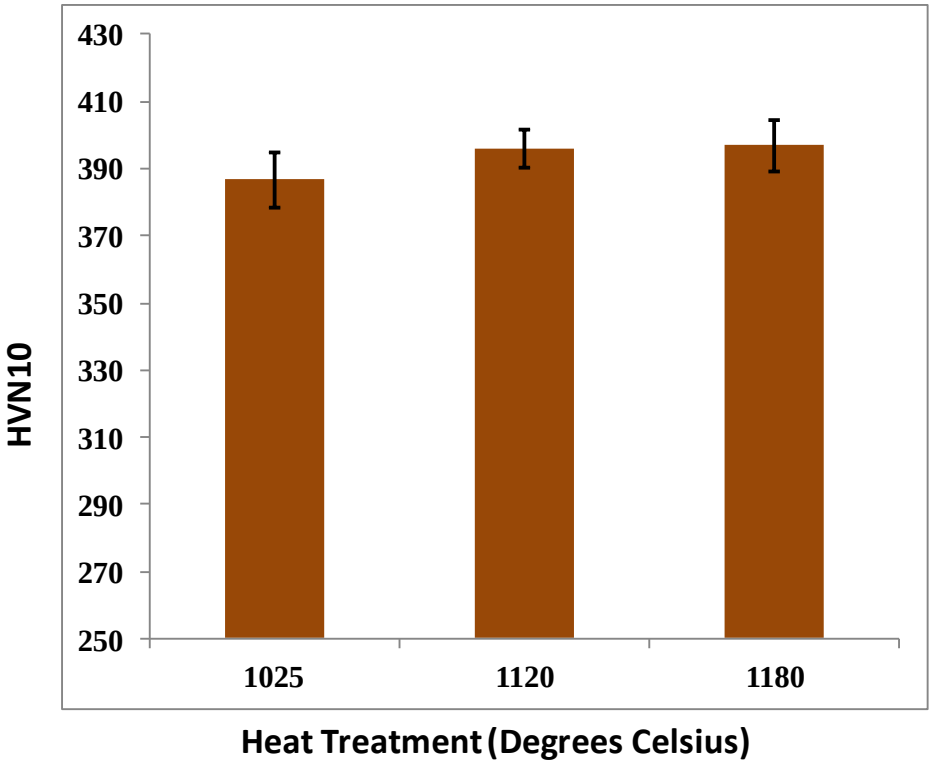

Figure 4 - 24: Vickers hardness of furnace-cooled IN 738 materials treated at 1025^{o}C, 1120^{o}C and 1180^{o}C for 2 h

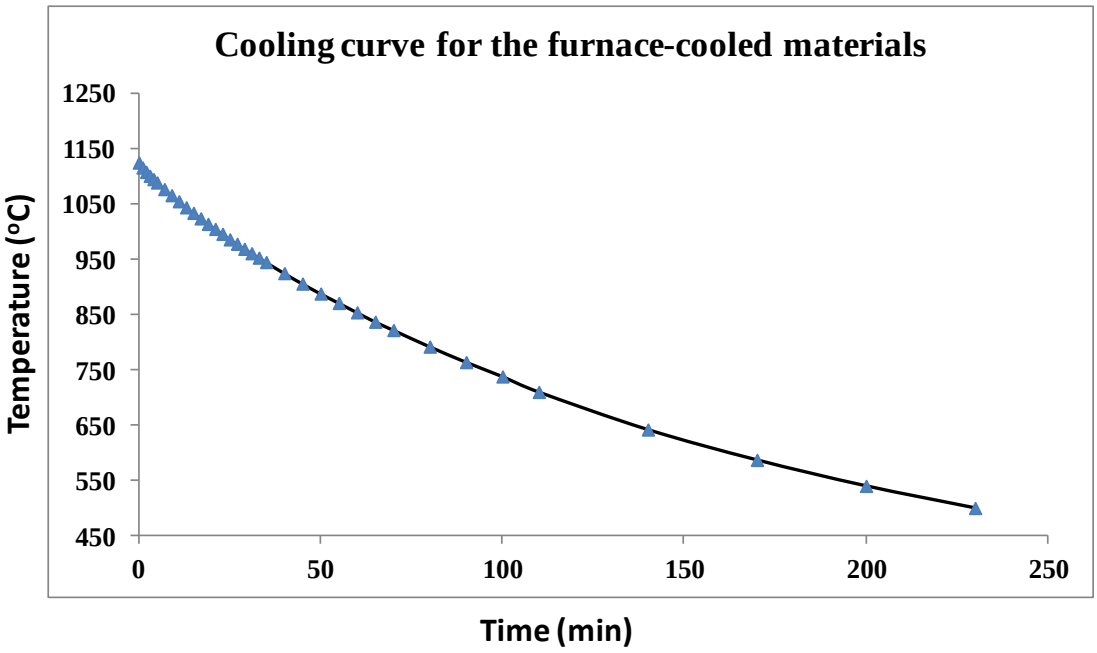

Figure 4 - 25: Temperature-time plot for furnace-cooling

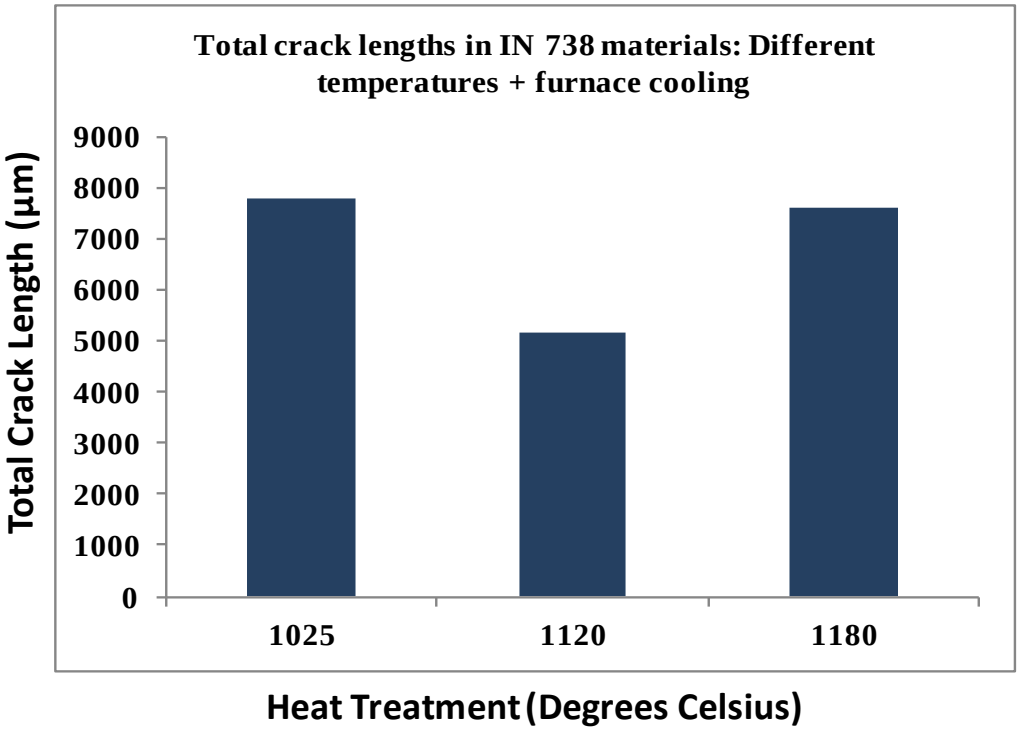

Figure 4 - 26: Total crack lengths in 10 sections each of IN 738 materials subjected to heat treatments at 1025^{o}C, 1120^{o}C and 1180^{o}C for 2 h, furnace-cooled

microstructural analysis of the material showed that some of the borides persisted in the alloy after the 2 h heat treatment time (Figure 4-27). The presence of borides in the alloy after heat treatment indicates that the alloy is still highly susceptible to HAZ intergranular liquation cracking. Ability to completely dissolve the borides at 1120^{o}C, where equilibrium segregation of boron can be effectively minimized, is desirable for the development of an effective heat treatment procedure for IN 738 superalloy. This possibility was investigated and is discussed next.

The concentration profile for the dissolution of a precipitate, for example, in a binary system, may be schematically represented as shown in Figure 4-28 [167, 168]. Earlier analysis of the phenomenon of second phase dissolution in alloy systems have shown that, for a stationary interface approximation, the dissolution rate dR/dt can be obtained as [167, 168]

$$\frac{dR}{dt} = -k\left[\frac{D}{R} + \sqrt{\frac{D}{\pi t}}\right] \qquad (4-7)$$

R is the radius of the precipitate, t is time, D is the volume interdiffusion coefficient (assumed to be independent of composition) and k is the supersaturation parameter, given as

$$k = \frac{2(C_I - C_M)}{(C_P - C_I)} \qquad (4-8)$$

C_P is the concentration of the precipitate. C_I and C_M are the concentrations at the precipitate/matrix interface and in the matrix, respectively. Aaron and Kotler [167] pointed out that |k| is usually very small (≈ 0.1) in most alloy systems and that in this

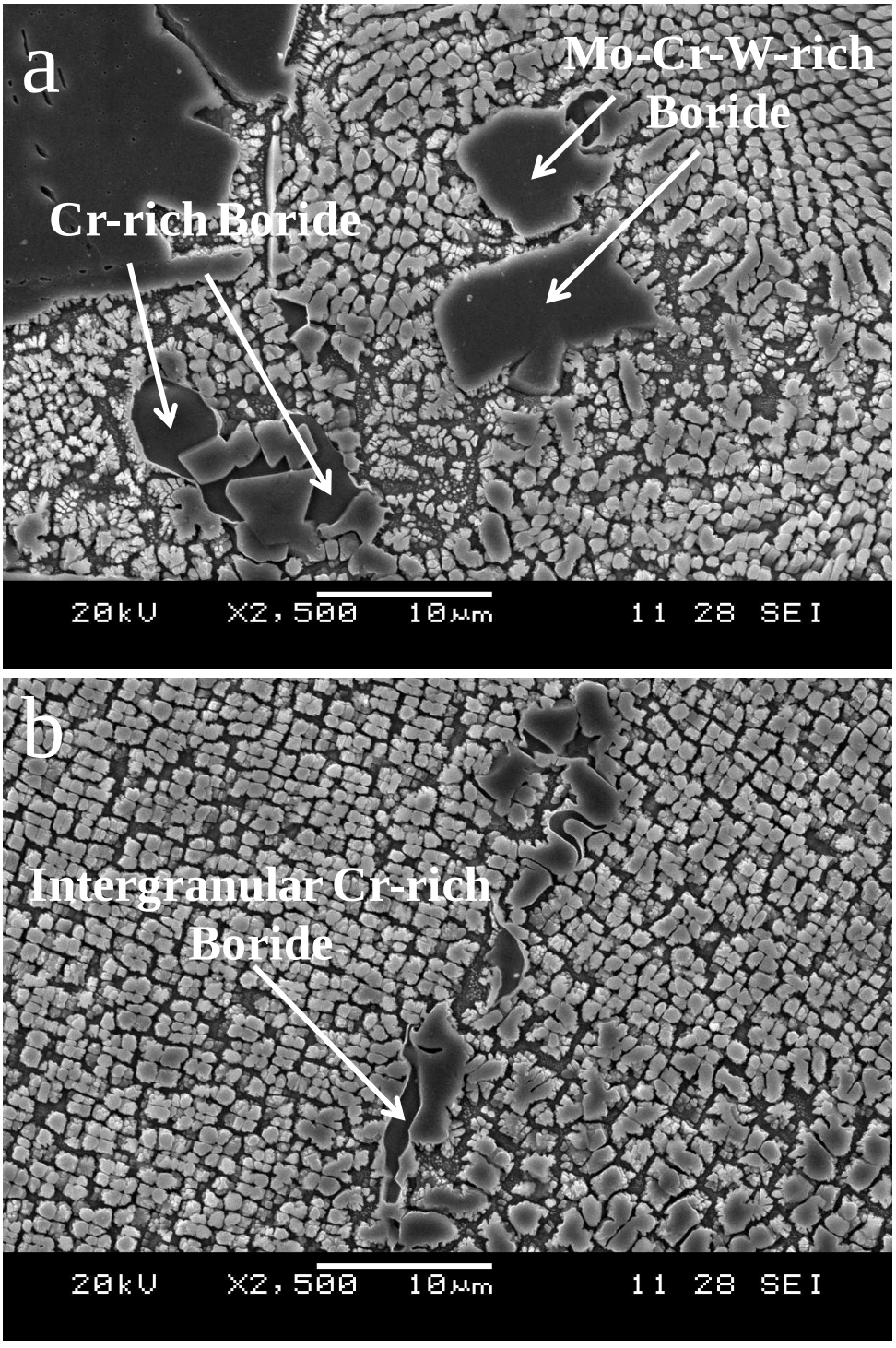

Figure 4 - 27: SEM micrographs showing the persistence of borides in IN 738 materials subjected to heat treatment at 1120^{o}C for 2 h, furnace-cooled.

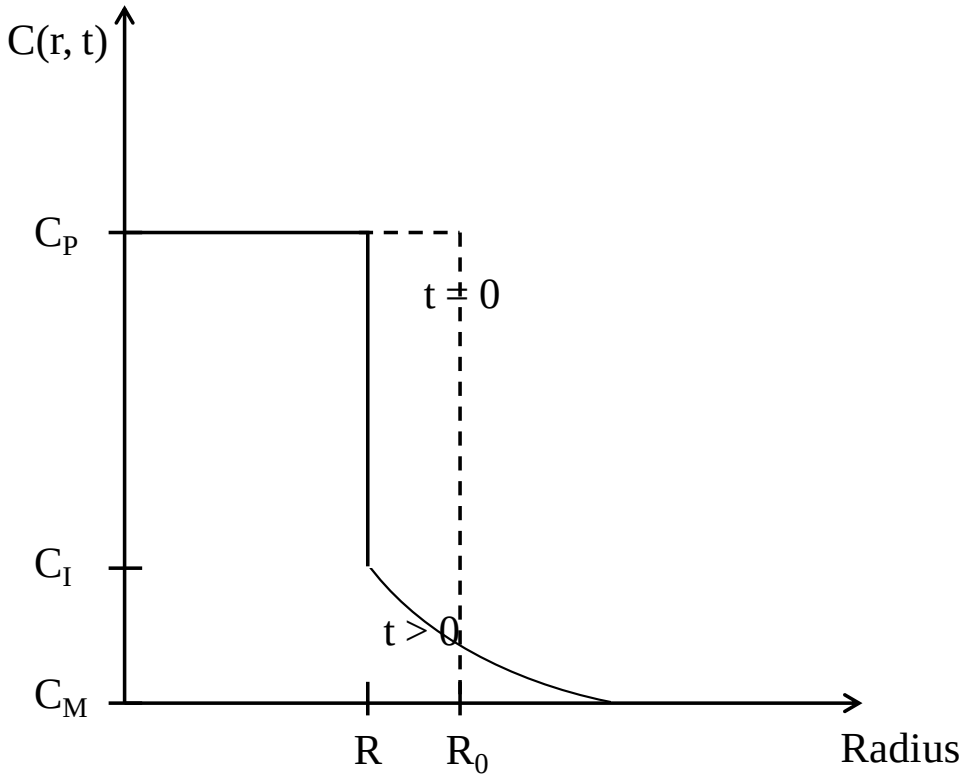

Figure 4 - 28: Schematic representation of the concentration profile for the dissolution of a second phase precipitate

small |k| limit, R becomes a slowly varying function of time. It has been suggested that the dissolution rate depends on both shape and size of the precipitate [167, 168]. For a planar precipitate, where R = ∞, dissolution rate is mainly governed by the $t^{1/2}$ term in equation 4-7. If R = ∞, then the D/R term tends to zero and does not contribute to the dissolution rate. This planar precipitate analysis can also be applied to spherical precipitates at the initial stages of dissolution, as stated by Whelan and Aaron et. al. [167, 168]. If the spherical precipitate is sufficiently large (large R), the precipitate/matrix interface may be approximated as being planar at the initial stages of dissolution before the precipitate becomes small enough for D/R to be significant. In this case, the dissolution rate is expected to be slow at the beginning but rapid when R becomes very small. In a more physical sense, it was suggested that the dissolution rate of a precipitate increases as the precipitate/matrix interfacial area decreases due to decrease in the size of the solute source with respect to the area of the diffusion zone surrounding it [167]. Therefore, the kinetics of larger size precipitates is expected to be slower than that of very small precipitates. A careful observation of the microstructure of the boride phases in IN 738 superalloy in the present work showed that the particles are mostly irregularly shaped. They varied greatly in size, from sub-micrometer sizes up to about 8 μm. While the smaller particles could have dissolved earlier during thermal treatment, the larger blocky ones survived for longer periods.

It should be noted that, apart from the influence of precipitate shape and size, there are other important factors that contribute to the dissolution rate. For diffusion-controlled dissolution, the diffusion rate of the slowest diffusing element may be the rate-controlling factor. The boride-forming elements in IN 738 superalloy, especially Mo and W, are

known to be very slowly diffusing components of most nickel-base superalloys [53]. The slowness in the diffusion of these elements in IN 738 superalloy could limit the dissolution rate of borides and result in very sluggish dissolution behaviour. Apart from a possible diffusion-limited dissolution, it has also been suggested that the occurrence of interface reactions that proceed slower than diffusion-controlled dissolution may limit the extent of dissolution of second phases [167]. This has been attributed to a possible reduction in the flux of atoms crossing the precipitate/matrix interface, which reduces the actual interface concentration C_I to a value below the equilibrium interface concentration. Sluggishness in the dissolution of borides in IN 738 superalloy would result in a requirement for longer holding times at the thermal treatment temperature if the borides were to be completely dissolved.

The possible effect of holding time on the dissolution of the boride phase in IN 738 superalloy at the selected thermal treatment temperature was studied by subjecting specimens of the alloy to treatments at 1120^{o}C for different times ranging from 2 h to 24 h. This study showed that some of the boride particles persisted in the alloy up to 12 h, showing that the dissolution behaviour of borides was sluggish indeed. For example, the SEM micrographs in Figure 4-29 revealed the persistence of boride phases in the alloy at 4 h and 8 h, respectively. The borides were observed to have dissolved completely in the alloy at 16 h. A similarly slow dissolution behaviour of second phase particles, in order of hours, has been observed in another alloy system [169]. In order to confirm the influence of boride dissolution on HAZ cracking susceptibility during welding and to correlate the result of the observation described above with actual welding data, IN 738 welding coupons were laser-arc hybrid welded after being subjected to pre-weld heat

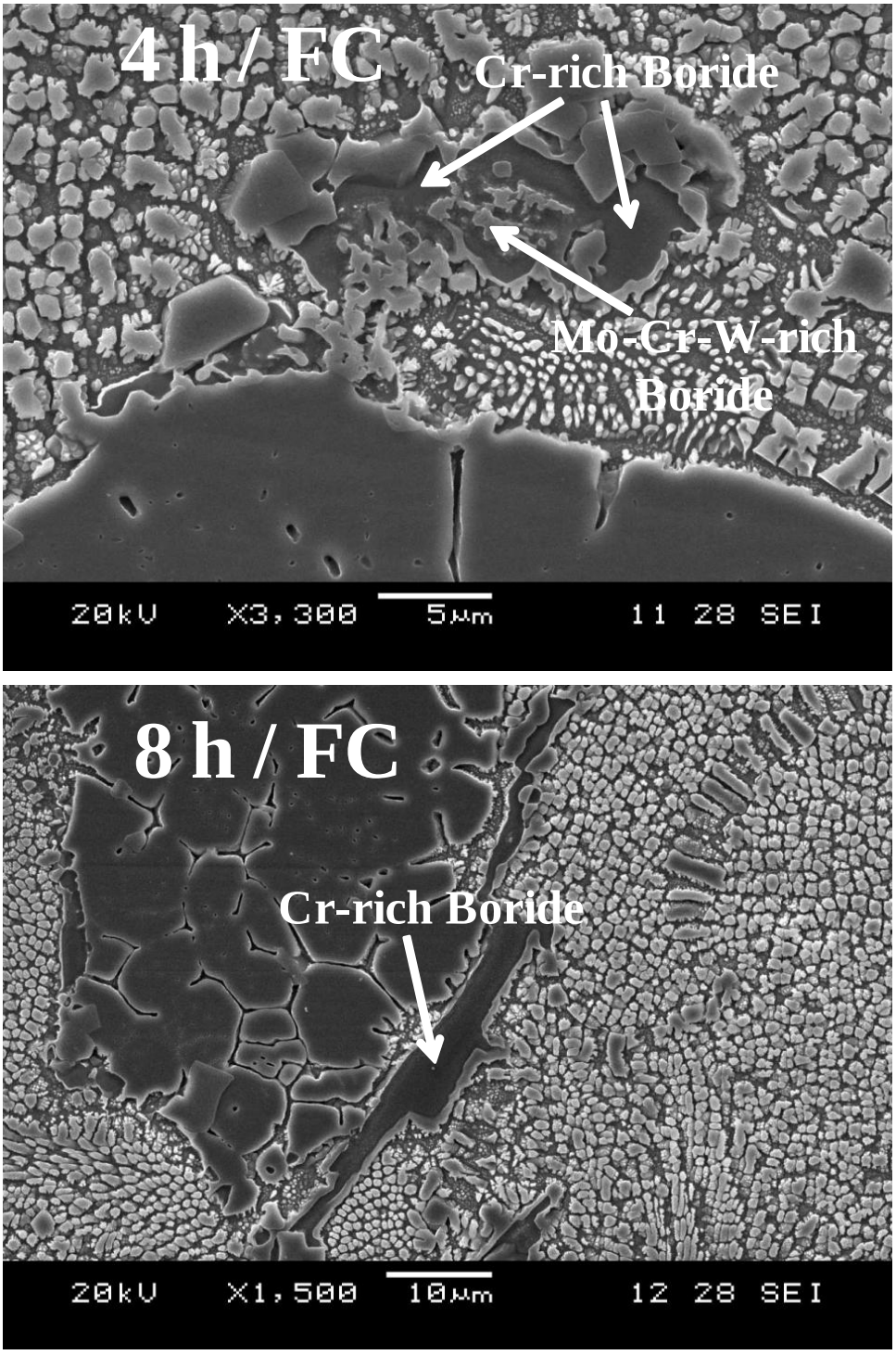

Figure 4 - 29: SEM micrographs showing the persistence of borides in IN 738 materials subjected to heat treatments at 1120^{o}C for 4 and 8 h, furnace-cooled

treatments at 1120^{o}C for times varying from 2 h to 24 h, followed by furnace cooling. The results are presented in Figure 4-30, showing the dependence of HAZ cracking susceptibility on holding time at 1120^{o}C. The least amount of cracking was realized in the material that was held for times from 16 h and above. This finding is in good agreement with the observed complete dissolution of borides in the alloy after 16 h. In addition, it should be noted that the hardness of the material did not vary with holding time at 1120^{o}C (Figure 4-31). This shows that the presence of borides in the materials treated for shorter time at 1120^{o}C is a major factor contributing to HAZ intergranular cracking susceptibility in these materials. Therefore, the thermal processing of 1120^{o}C / 16 h / FC, designated as FUMT, is chosen as a practicable and effective heat treatment for improving the weldability of IN 738 superalloy during laser-arc hybrid welding of the alloy. A comparison of HAZ cracking susceptibility in the newly developed FUMT and the standard heat treatment (SHT) is given in Figure 4-32, showing about 80% reduction in cracking susceptibility when the FUMT is used.

4.2.4 Microstructural Analysis of IN 738 Superalloy in the New FUMT Condition

The microstructure of the FUMT-treated IN 738 superalloy consisted of irregularly shaped γ' precipitates, as shown in the SEM image of Figure 4-33. High magnification SEM analysis (inset of Figure 4-33) also revealed the presence of very fine γ' precipitates that formed during the heat treatment. MC carbides and γ-γ' eutectics survived the FUMT treatment. Most importantly, no boride particles were observed in the FUMT material.

Observations in this work suggest that laser-arc hybrid welding technology is easily adaptable to the joining of nickel-base IN 738 superalloy and, possibly, other nickel-base superalloys, producing a desirable weld bead shape and appearance. In addition,

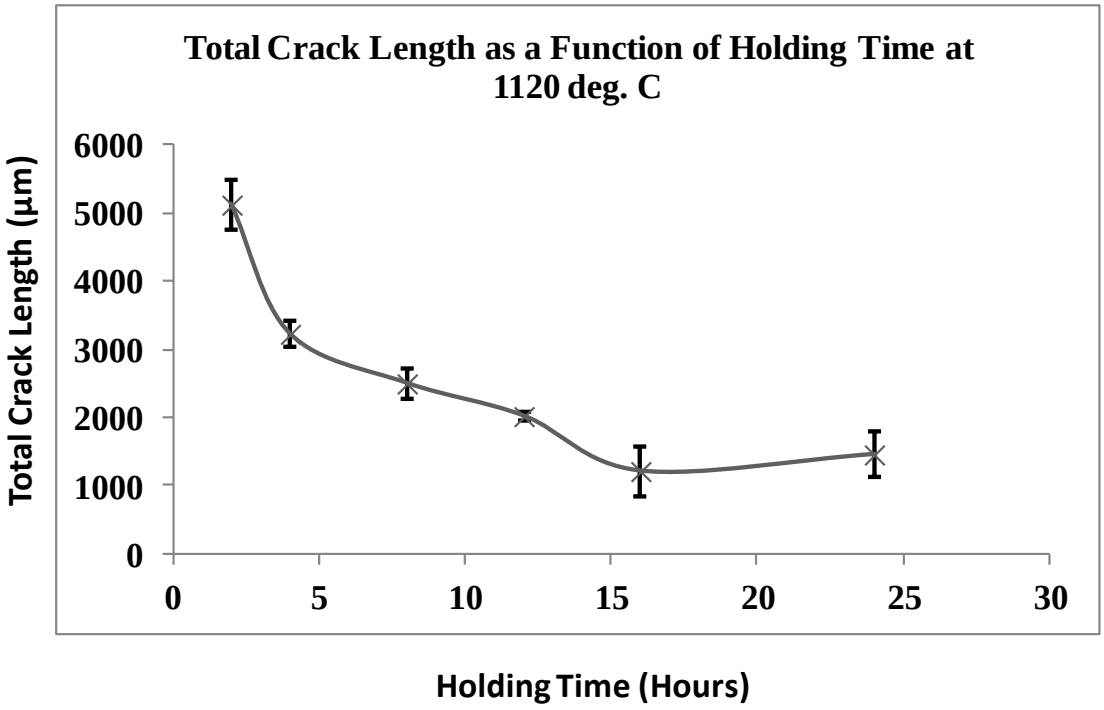

Figure 4 - 30: The effect of holding time at 1120^{o}C on HAZ intergranular cracking susceptibility for materials held for times from 2 to 24 h, followed by furnace cooling.

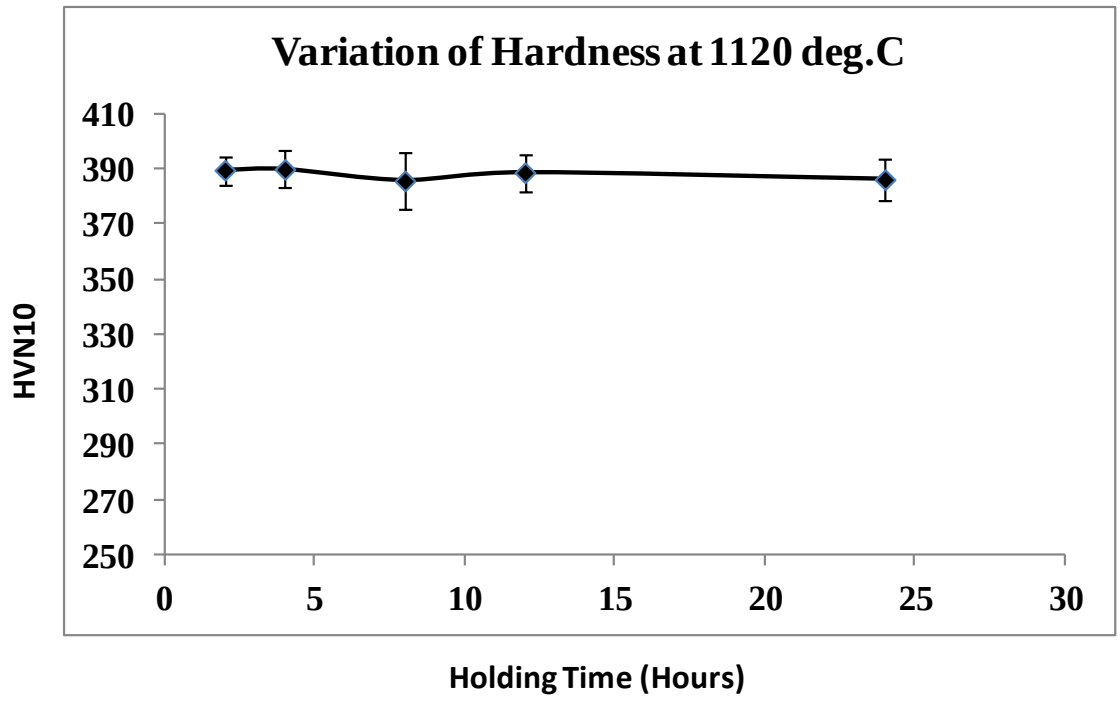

Figure 4 - 31: Vickers hardness variation for IN 738 samples treated at 1120^{o}C for different holding times, followed by furnace cooling.

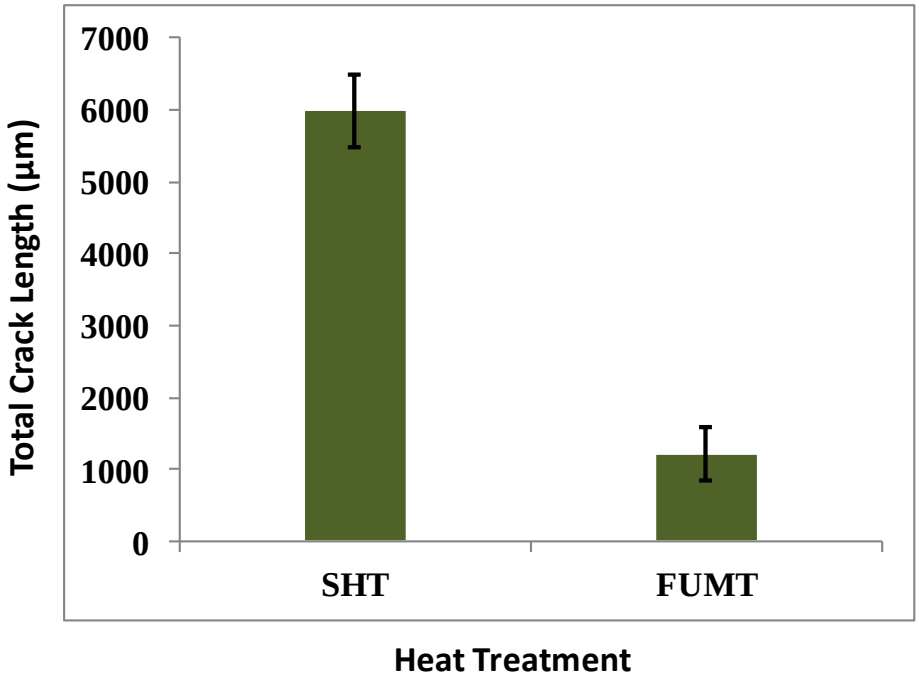

Figure 4 - 32: A comparison of HAZ cracking susceptibility in laser-arc hybrid welded SHT and FUMT materials

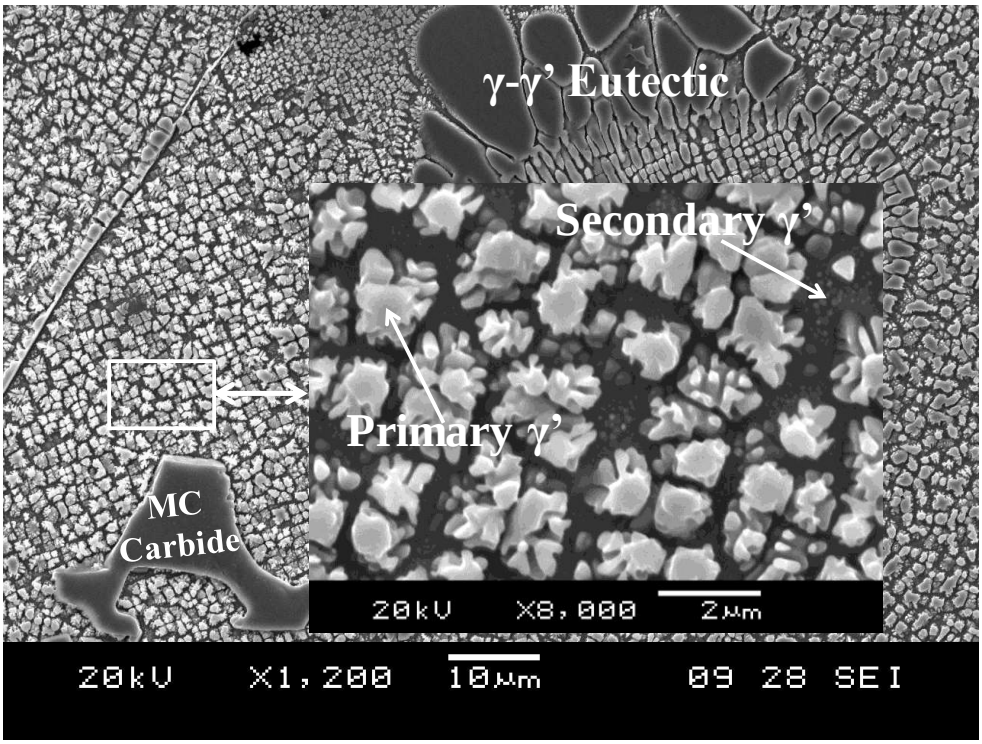

Figure 4 - 33: Microstructure of the IN 738 superalloy showing γ' precipitate, γ-γ' eutectic and MC carbide in the material subjected to the new FUMT treatment

susceptibility to HAZ intergranular liquation cracking, which is common during fusion welding of precipitation strengthened nickel-base superalloys, can be drastically reduced in IN 738 superalloy by the application of the newly developed pre-weld FUMT treatment. These findings are very crucial to the adoption of laser-arc hybrid welding of nickel alloys as an industrially feasible and beneficial manufacturing process. Another factor that requires a careful consideration during laser-arc hybrid welding is the role of filler alloys on metallurgical characteristics and weld quality. Due to the strong dependency of laser-arc hybrid welding characteristics on filler alloys, studies were performed on IN 738 superalloy during the process using nickel-base filler alloys of various compositions in order to understand the role of filler alloys on HAZ cracking susceptibility. The results are elucidated in the next section.

4.3 The Role of Filler Alloy Composition on Laser-Arc Hybrid Weldability

4.3.1 Introduction

One of the advantages of laser-arc hybrid welding is the possibility of reducing weld cracking through proper selection and use of welding filler alloys [6, 10]. In this part of the present work, the results of studies on the role of filler alloys of varying compositions on the susceptibility of nickel-base IN 738 superalloy to HAZ intergranular cracking during laser-arc hybrid welding is discussed.

4.3.2 Filler Alloy Composition and HAZ Cracking Susceptibility

The selection of filler alloys is known to be a critical factor to consider in producing welds that meet service requirements for strength, corrosion resistance and tolerance for dilution with the base alloy without causing excessive cracking in the fusion zone (FZ) [170-172]. While the influence of filler alloys on weld metal cracking is commonplace, susceptibility to cracking in the HAZ due to variation in filler alloy composition is sometimes overlooked. Five different filler alloys were selected to study the role of filler alloy composition on HAZ intergranular liquation cracking susceptibility based on their Al + Ti + Nb + Ta concentration. Al and Ti are generally known to be important precipitation hardening components contributing to the volume fraction of the $L1_2$-γ' phase in nickel-base superalloys [45, 173]. However, in addition to Al and Ti, studies have shown that in the $L1_2$ γ'-type A_3B intermetallic compound the element B can be Al, Ti, Nb or Ta [1]. The presence of Nb in γ' has been experimentally verified [174], while Ta has also been found to be a strong participant in γ' formation, particularly in single crystal alloys [1]. The atomic concentration of Al + Ti + Nb + Ta in the filler alloys used in this work varied in the decreasing order in Rene 41 □ HY 282 □ IN 718 □ FM 92 □

IN 625. The addition of a filler alloy during welding modifies the composition of the melted base material in the FZ by diluting it. This results in a FZ that consists of a mixture of the filler alloy and the base alloy. An expression for calculating the fraction of the weld metal that results from the consumption of the filler alloy was derived in section 4.1. This expression, which assumes complete mixing of the filler alloy and the base alloy in the fusion zone, is given by

$$F = \frac{\pi r^2 S_F}{A S_W} \quad \text{.....(4-9)}$$

where r is the radius of the filler wire, A is the cross-sectional area of the FZ measured in the plane transverse to the welding direction, S_W and S_F are the welding speed and the filler wire feed speed, respectively. The calculated value of F and the compositions of as-received IN 738 superalloy and the filler alloys were used to estimate the atomic concentration of Al + Ti + Nb + Ta in the weld metal for all the filler alloys used. The result is presented in Table 4.2, which shows that the concentration of Al + Ti + Nb + Ta in the weld FZ also varied in the decreasing order of Rene 41 □ HY 282 □ IN 718 □ FM 92 □ IN 625.The effect of this compositional variation on liquation cracking in the HAZ of the laser-arc hybrid welded materials was studied.

Figure 4-34 shows the total crack length (TCL) measured in the HAZ of IN 738 materials that were laser-arc hybrid welded with the five filler alloys. The trend shows that the filler alloys with higher Al + Ti + Nb + Ta concentration exhibited higher propensity for HAZ cracking. A similar observation has been reported in a previous work on Gas Tungsten Arc (GTA) welded IN 738 superalloy, which also showed that the composition of the filler alloys is an important factor determining the extent of cracking in the HAZ

Table 4 - 2: Al + Ti +Nb + Ta concentration in the weld metals (atomic percent)

Filler Alloy	**IN 625**	**FM 92**	**IN 718**	**HY 282**	**Rene 41**
Al	5.9	5.8	6.0	6.6	6.6
Ti	3.3	4.1	3.5	3.9	4.1
Nb	0.8	0.4	1.2	0.5	0.4
Ta	0.5	0.4	0.4	0.4	0.4
Al + Ti + Nb + Ta in FZ	**10.5**	**10.8**	**11.2**	**11.3**	**11.6**

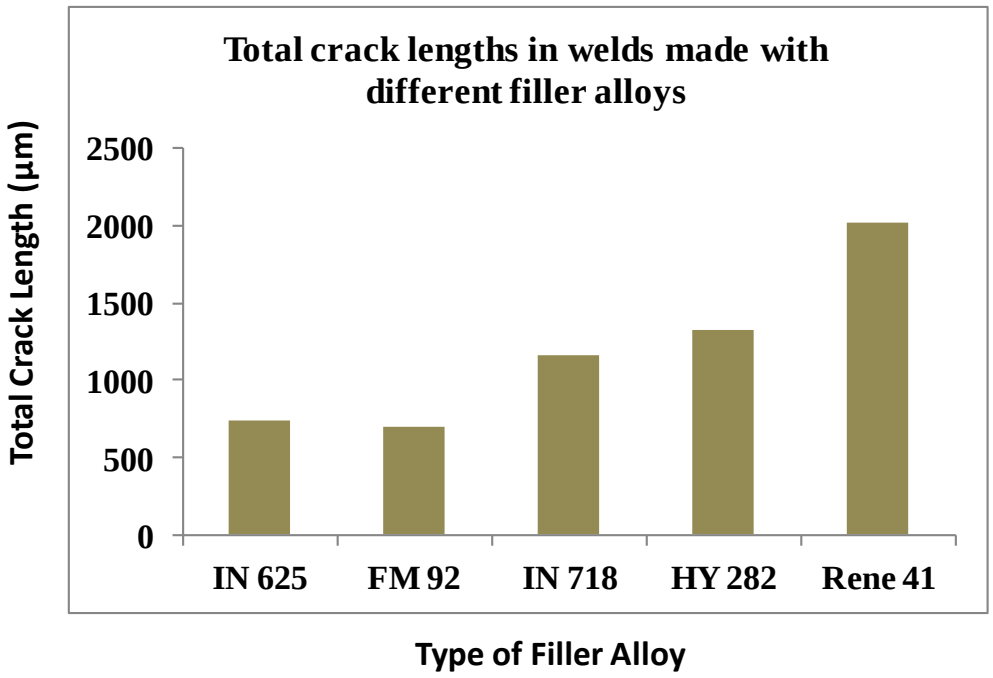

Figure 4 - 34: Total crack lengths measured from 10 sections each of laser-arc hybrid welded IN 738 superalloy using 5 different welding filler alloys

[158]. In IN 738 superalloy and, in fact, other γ' strengthened nickel-base superalloys, variation in the concentration of precipitation hardening components in the weld metal could result in a significant change in precipitation strengthening behaviour within the fusion zone. Variation in concentration of Al + Ti + Nb + Ta in the fusion zone can produce two main effects on the precipitation of γ' particles in the alloy.

Firstly, a lower concentration of Al + Ti + Nb + Ta is expected to produce a lower volume fraction of the precipitate. In order to analyze this possibility, a theoretical thermodynamic calculation software, JMatPro, was used to determine the volume fraction of γ' particles that would precipitate during weld solidification, based on the composition of the weld metal, for all the five filler alloys. The results showed that the volume fraction of γ' precipitates varied according to the calculated concentration of Al + Ti + Nb + Ta in the weld metal (Figure 4-35). A combined plot of both TCL and γ' volume fraction as a function of the calculated concentration of Al + Ti + Nb + Ta in the weld metals (Figure 4-36) suggests that the trend in HAZ cracking susceptibility is significantly influenced by variation in the volume fraction of γ' precipitate. In addition, SEM-EDS semi-quantitative analysis was carried out to determine the composition of the dendritic core regions of the fusion zone when different filler alloys were used. The EDS data represents the composition of the core only and does not account for any effect of microsegregation of various elements. Nevertheless, a plot of the volume fraction versus concentration of Al + Ti + Nb + Ta based on the experimental SEM-EDS results agree with the results of the Al + Ti + Nb + Ta concentration obtained from the calculations, and shows that the variation in HAZ cracking susceptibility is attributable to the compositional variation in the weld metals (Figure 4-37).

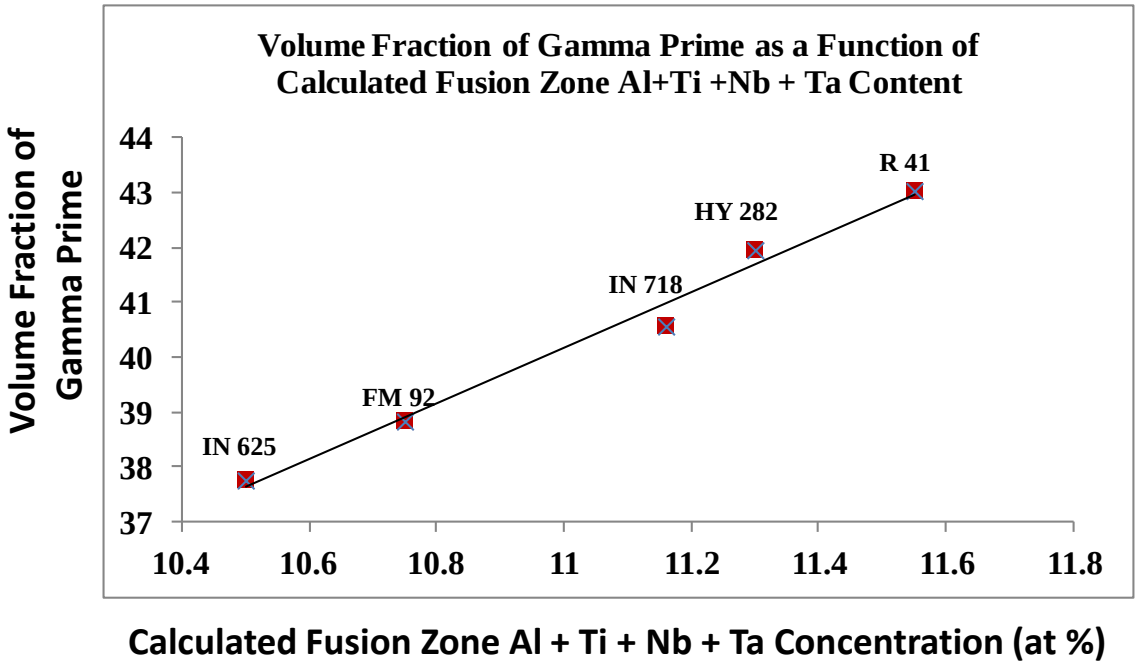

Figure 4 - 35: A plot of the volume fraction of γ' particles as a function of calculated values of concentration of Al + Ti + Nb + Ta in the weld metal of various welds made with different filler alloy

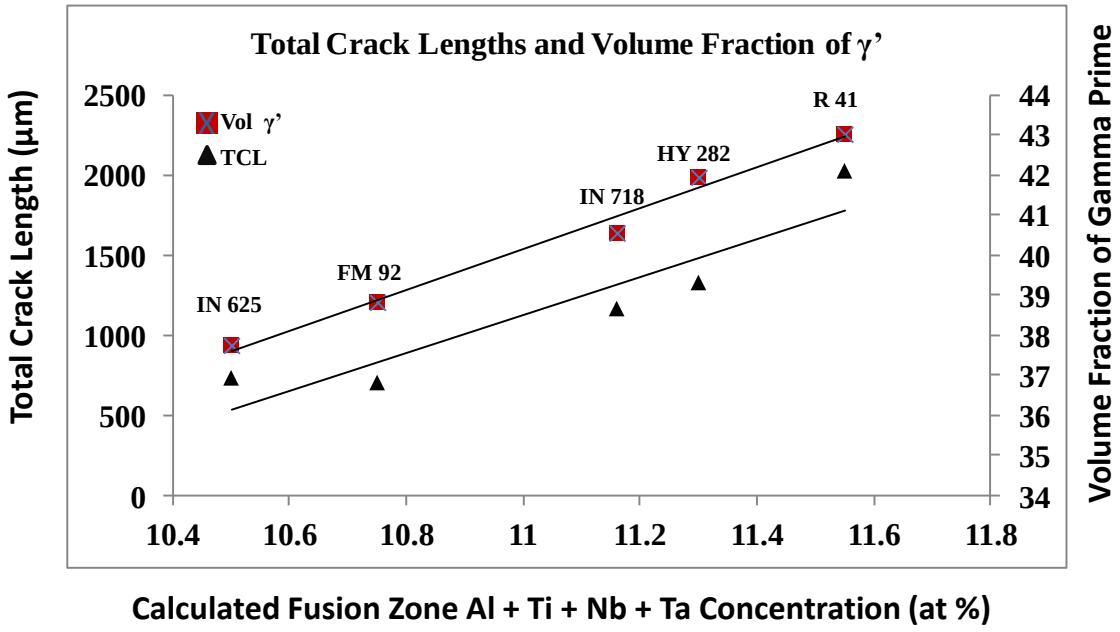

Figure 4 - 36: Plots of total crack length and volume fraction of γ' as functions of calculated values of concentration of Al + Ti + Nb + Ta in the fusion zone

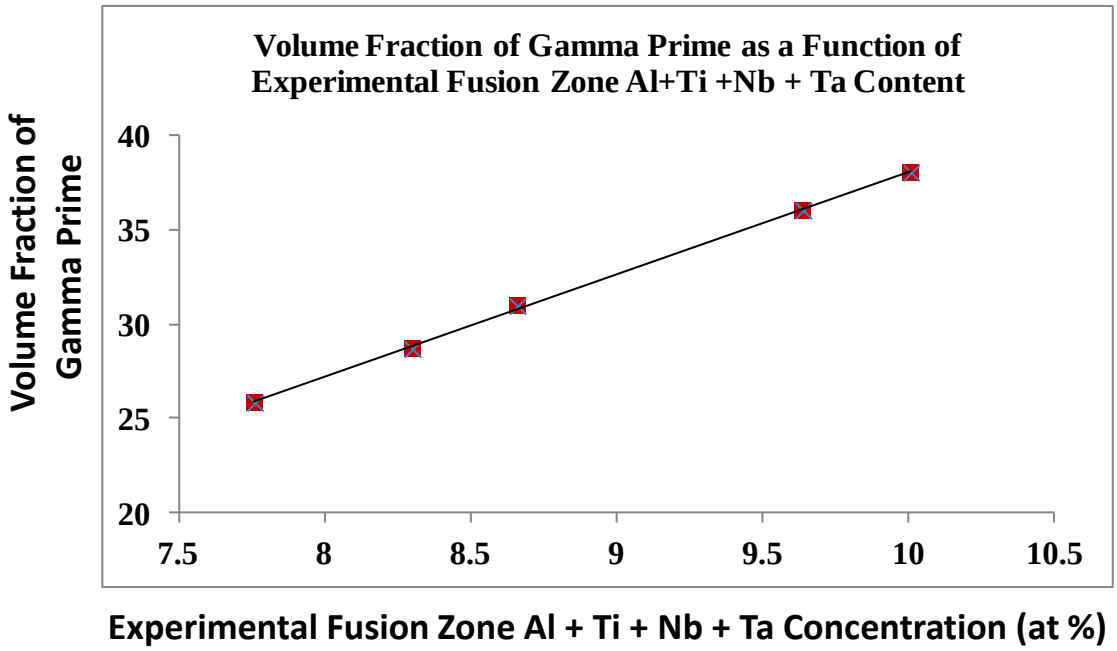

Figure 4 - 37: A plot of volume fraction of γ' as a function of experimentally determined concentration of Al + Ti + Nb + Ta in the fusion zone

The second effect of the variation in concentration of Al + Ti + Nb + Ta on the precipitation of γ' particles relates to the solvus of the precipitate. The higher the concentration of Al + Ti + Nb + Ta, the higher the solvus of γ' precipitate. For example, the solvus of γ' precipitate in HY 282 (Al + Ti + Nb + Ta = 6.24 at.%) and IN 738 (Al + Ti + Nb + Ta = 12.46 at.%) are 997^{o}C and 1165^{o}C, respectively [173]. Higher γ' solvus suggests that the precipitates could have started to form at higher temperatures. The generation of tensile stresses, which eventually leads to HAZ intergranular cracking in nickel-base superalloys, does not generally start until the weld begins to cool [175]. The alloy remains susceptible to cracking until it is cooled down to the ductility recovery temperature (DRT), where most of the intergranular liquid has been resolidified. The difference between the peak temperature reached, T_p and the DRT is referred to as the brittle temperature range (BTR). The DRT in IN 738 superalloy was found to be as low as 1000^{o}C [176]. Formation of γ' precipitates at higher temperatures within the BTR can contribute significantly to the on-cooling tensile stresses, thereby resulting in higher susceptibility to HAZ cracking.

The observation of a relationship between HAZ cracking susceptibility and the variation in concentration of Al + Ti + Nb + Ta in the weld metals, coupled with the correlation between this variation and the precipitation of γ' particles, suggests that γ' particles precipitated in the fusion zone. However, detailed SEM study did not reveal the presence of γ' precipitate in the fusion zone (Figure 4-38). In order to fully understand the microstructural characteristics of the fusion zone, TEM analysis was carried out, which shows that γ' particles indeed precipitated in the FZ and resulted in significant precipitation hardening of the weld metals.

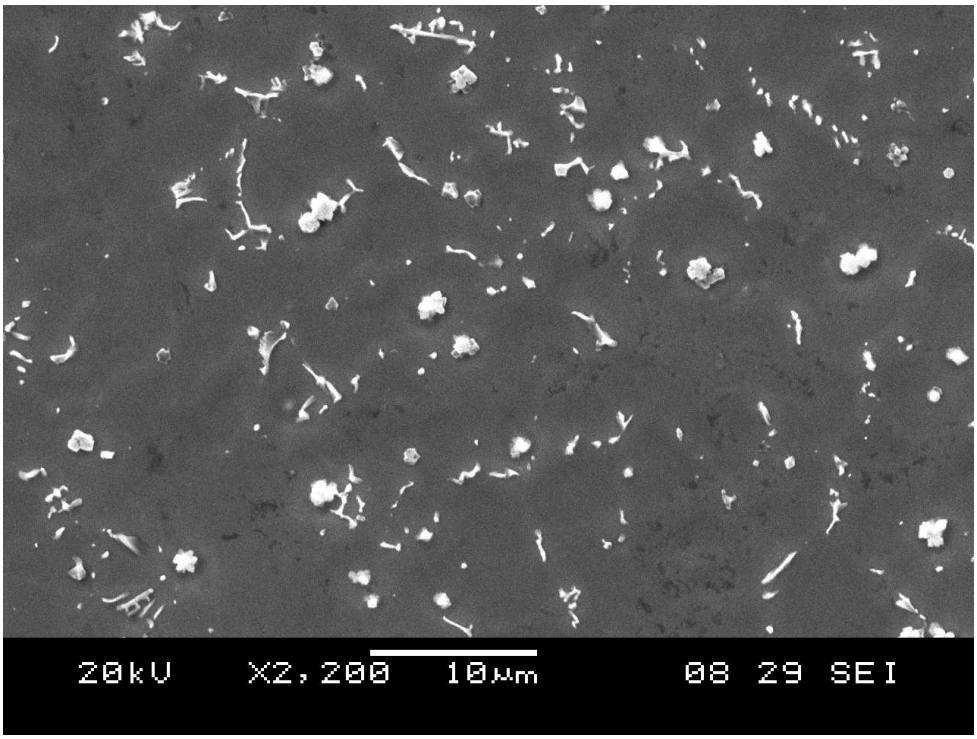

Figure 4 - 38: SEM micrograph of the fusion zone, showing carbides but no γ' particles

4.3.3 TEM Study of γ' Precipitation

The results of the TEM analysis that was performed on the fusion zone of weldments made with all five different filler alloys revealed the presence of nanosize spherical γ' particles in the weldments. Dark field TEM images and SADPs taken from different zone axis, all showing superlattice reflections of γ' particles, confirm that the precipitate is present in the fusion zone for all the 5 filler alloys (Figures 4-39 to 4-43). The results revealed that the largest average particle diameter was observed in the material that was welded with Rene 41 filler alloy. The average particle diameter in the weld metal with Rene 41 appeared to be of the order of about 10 nm. A qualitative observation of the dark field images (Figures 4-39 to 4-43) also suggests that the extent of γ' precipitation varied with the concentration of Al + Ti + Nb + Ta , with the largest amount appearing to have precipitated in the material welded with Rene 41 filler alloy and reduced with a reduction in the concentration of Al + Ti + Nb + Ta. Precipitation hardening generally occurs when the motion of a gliding dislocation is impeded by a secondary phase, such as the ordered $L1_2$ intermetallic γ' phase in nickel base superalloys [177-180]. The presence of γ' particles and the variation in the volume fraction of the precipitate could result in different precipitation hardening behaviour in the weld metals, which is expected to reflect in the micro-hardness measured in the fusion zones. The weld metals with higher a Al + Ti + Nb + Ta concentration, and consequently higher volume fraction of γ' particles, exhibited higher microhardness, while the weld metals with lower Al + Ti + Nb + Ta concentration exhibited lower microhardness (Figure 4-44). The TEM results and the observed trend in precipitation hardening are in agreement with both the calculated volume fractions of γ' particles in the weld metals and the TCL measured in the HAZ of

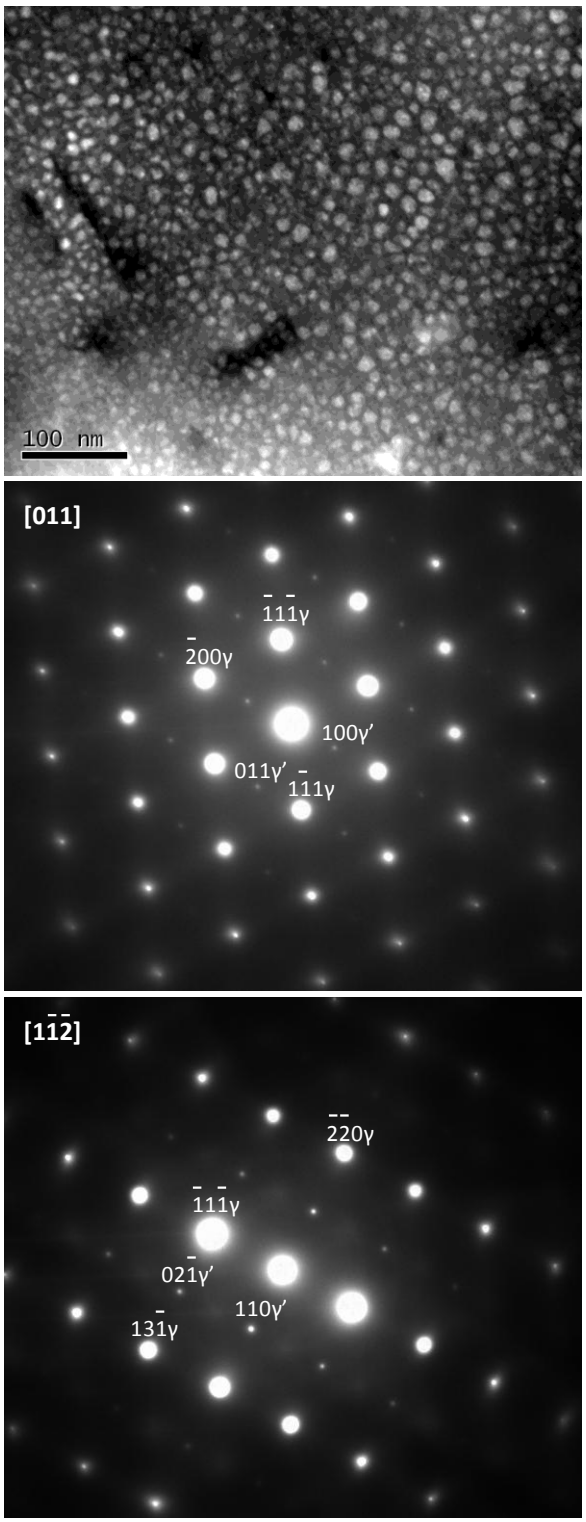

Figure 4 - 39: TEM dark field image of the weld metal with Rene 41 filler alloy and SADPs showing superlattice reflections of γ' precipitates

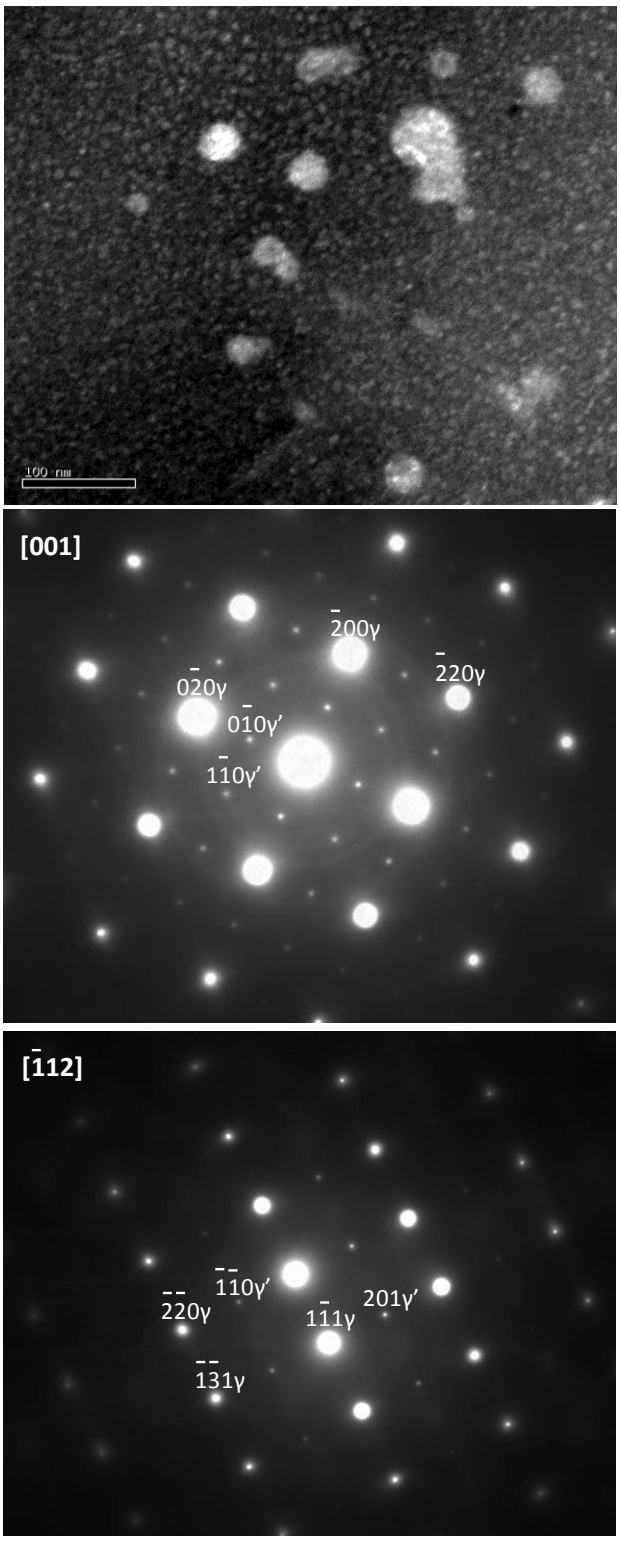

Figure 4 - 40: TEM dark field image of the weld metal with HY 282 filler alloy and SADPs showing superlattice reflections of γ' precipitates

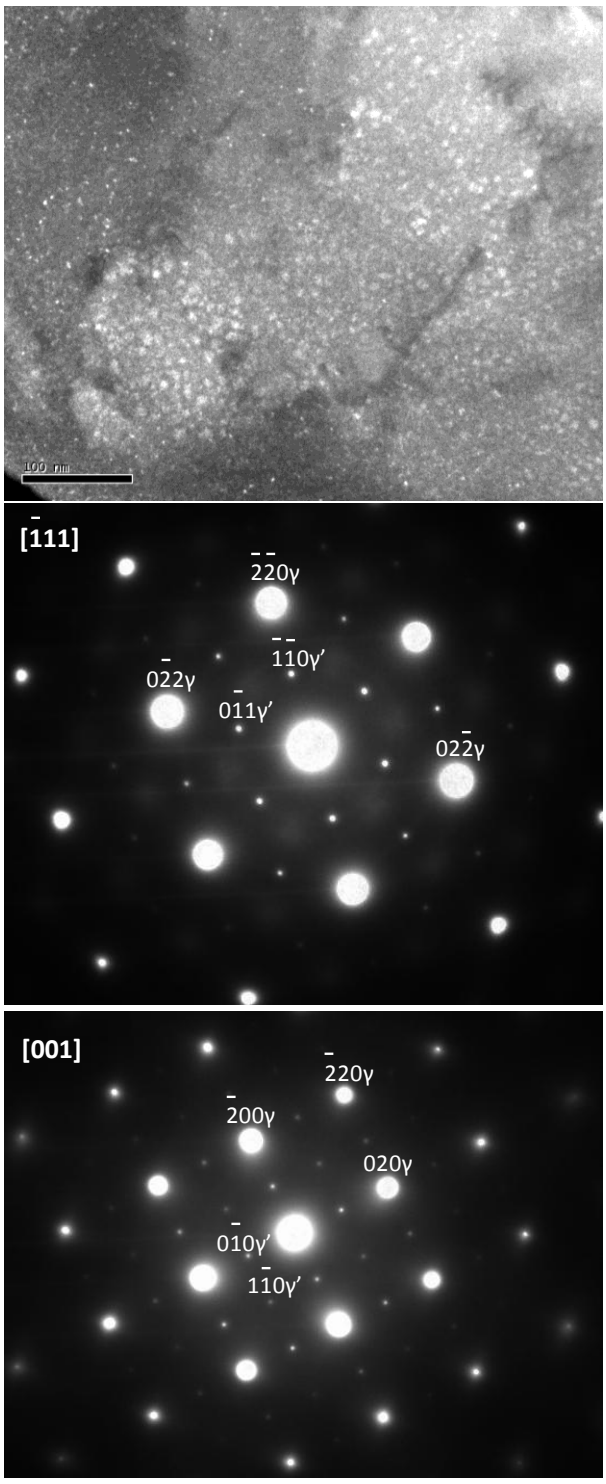

Figure 4 - 41: TEM dark field image of the weld metal with IN 718 filler alloy and SADPs showing superlattice reflections of γ' precipitates

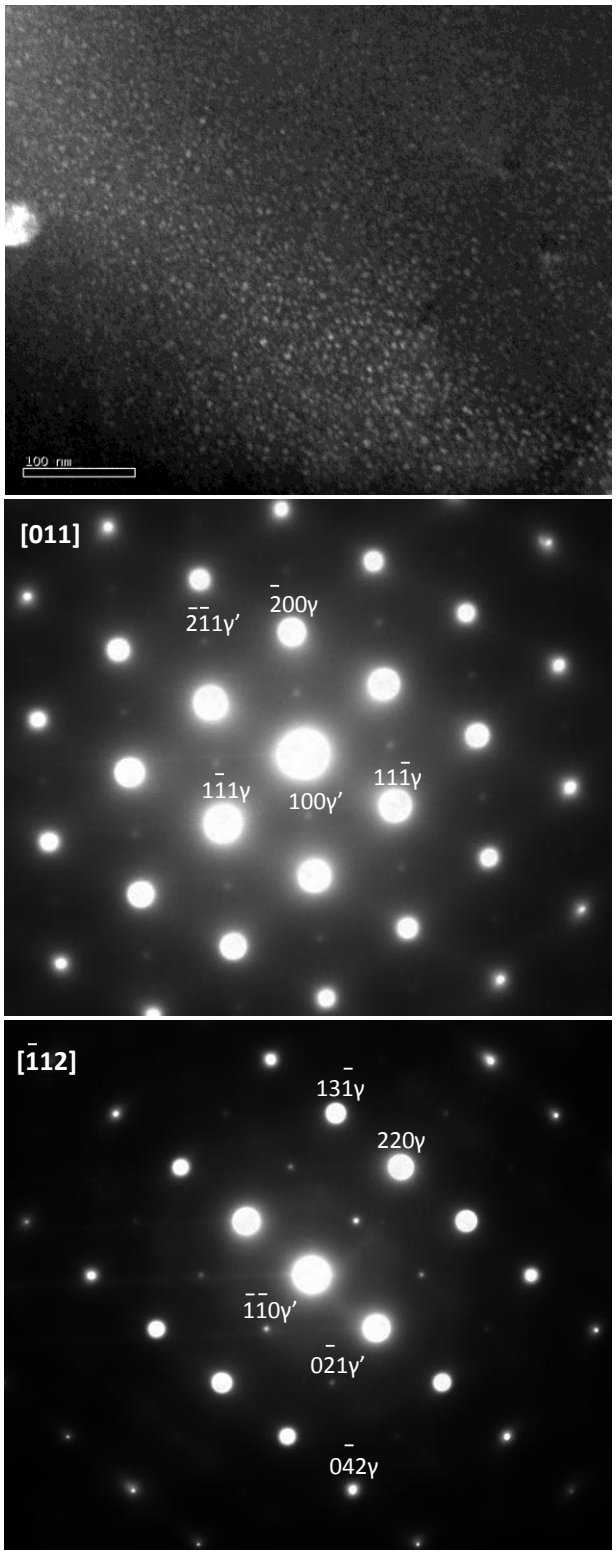

Figure 4 - 42: TEM dark field image of the weld metal with FM 92 filler alloy and SADPs showing superlattice reflections of γ' precipitates

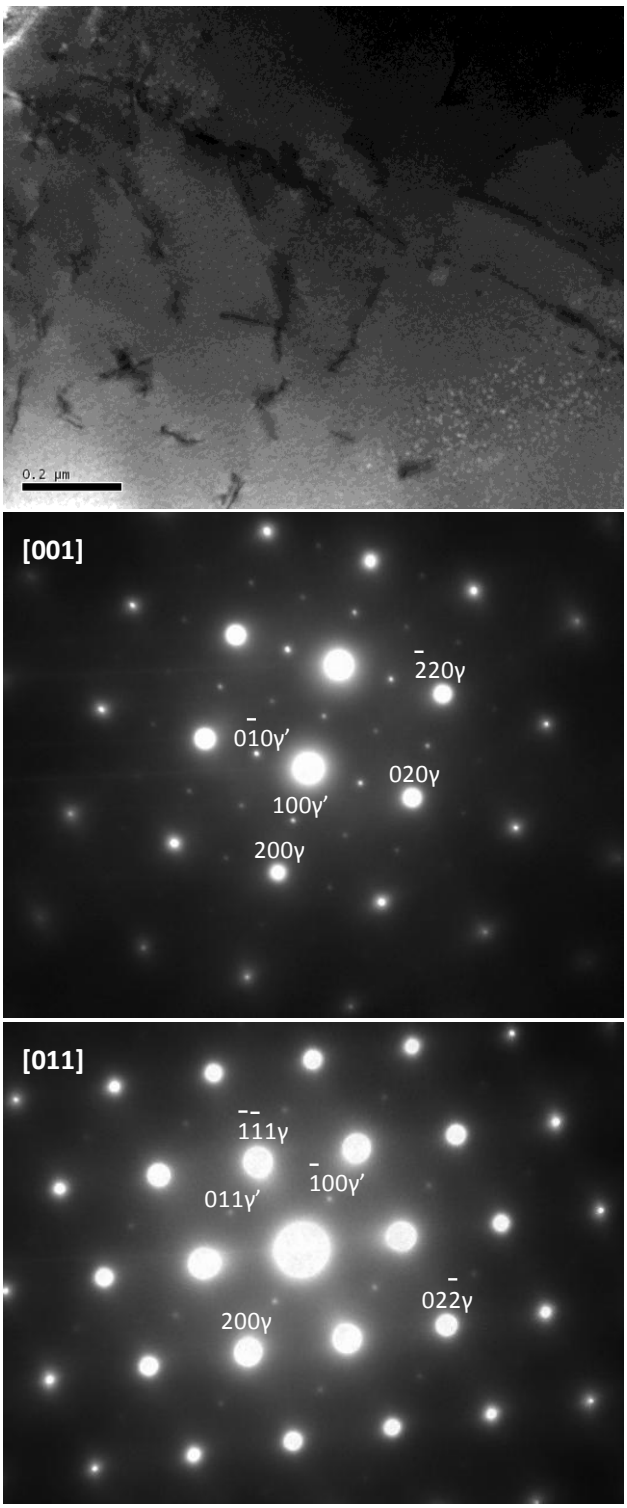

Figure 4 - 43: TEM dark field image of the weld metal with IN 625 filler alloy and SADPs showing superlattice reflections of γ' precipitates

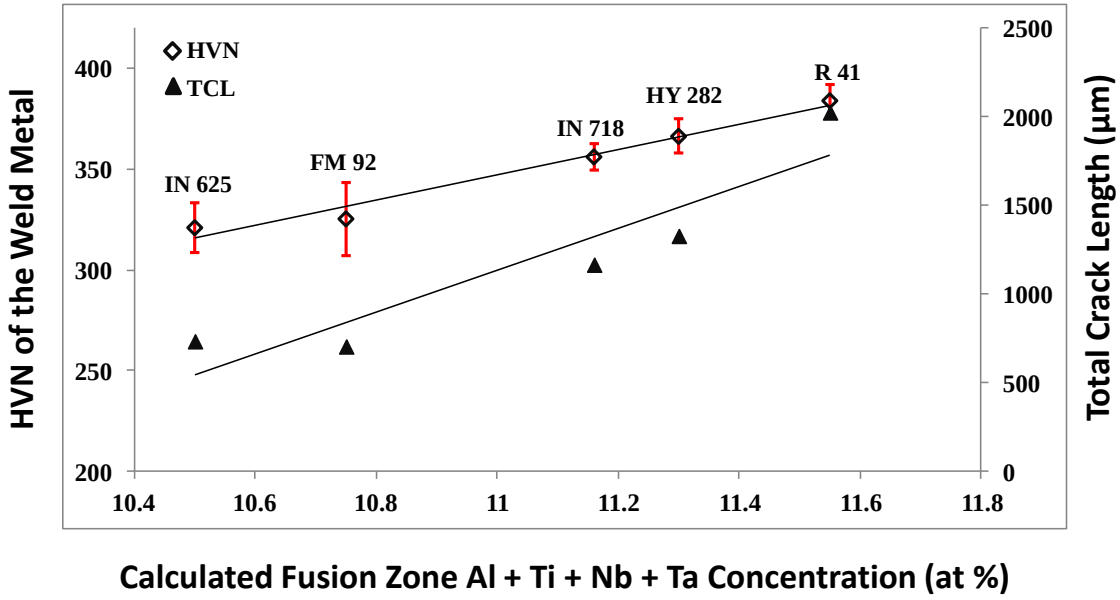

Figure 4 - 44: Plots of weld metal micro-hardness and total crack length as functions of calculated values of concentration of Al + Ti + Nb + Ta.

the welds. This result suggests that lower volume fraction of γ' phase produced softer weld metals and vice versa.

The TEM observations of γ' particles in the fusion zone of all the weldments in this work and the qualitative observation of volume fraction difference corroborate earlier discussions on the relationship between Al + Ti + Nb + Ta concentration and the volume fraction of γ' particles. The present results show that susceptibility to intergranular cracking in the HAZ of IN 738 superalloy is dependent on precipitation hardening in the weld metal, which, in turn, depends on the composition of the filler alloy used during laser-arc hybrid welding. As discussed earlier, the driving force for HAZ intergranular cracking is the generation of tensile stresses during weld cooling. A softer weld metal is expected to accommodate the tensile stresses to a greater extent while a harder weld metal would tend to offer more restraint to plastic deformation, thereby transferring most of the on-cooling tensile stresses to the HAZ. This could have resulted in more HAZ cracking due to the inability of the HAZ to relax the welding stresses. In addition to metallurgical compatibility of a filler alloy to a base alloy during welding, slow strength recovery and high-temperature ductility have been identified to be crucial in selecting appropriate filler alloy composition [181]. An experimental study of problems associated with welding investment-cast cobalt-base alloys has also shown that softer lower-carbon filler alloys produce welds that are less susceptible to hot cracking in the HAZ [181]. The variation in cracking susceptibility observed in the present work can be attributed to the variation in precipitation hardening behaviour of the weld metals based on Al + Ti + Nb + Ta concentration. Aside from the influence of precipitation hardening, the shrinkage, and the consequent volumetric changes that accompany γ' precipitation, is another factor

that needs to be considered in understanding the effect of filler alloy composition on HAZ cracking susceptibility.

4.3.4 Possible Effect of Volumetric Changes

Earlier theoretical and experimental analysis revealed that the linear dimension of a crystal is directly proportional to the volume fraction of a new phase that precipitates from the solid solution of the crystal if both phases have the same isotropic elastic properties [182]. This change in dimension was given as

$$\frac{\Delta l}{l} = \frac{v_o}{3v_B}\left[\frac{v_B - v_o}{v_o} - \eta(\upsilon_B - \upsilon_o)\right]p \qquad (4-10)$$

where v_B, v_o and υ_B, υ_o are the effective atomic volumes and atomic concentrations of the precipitate phase and solid solution, respectively, in the original state, η is the coefficient of proportionality in Vegard's law and p is the volume fraction of the precipitate. In the experiment of Gitgarts et. al [182], dilational analysis performed horizontally on rods of a nickel-base alloy showed that linear dimensional change (-Δl/l) of the rods was directly proportional to the volume fraction of the γ' phase during aging. In another work on tungsten inert gas (TIG) welding of IN 738 superalloy using different filler alloys [158], the lattice parameters a_γ and $a_{\gamma'}$ for the matrix phase and the precipitate phase, respectively, were determined for the weld metals with the different filler alloys by TEM. The lattice parameter for the γ' phase was observed to be consistently smaller than that of the matrix phase. For example, the results for weld metals with Rene 41 and IN 718 filler alloys, alongside the percent difference between the lattice parameters for the two phases, are presented in Table 4-3. The data shows 1.47% and 0.35% differences in linear dimensions between γ and γ' phases for the weld metals with Rene 41 and IN 718 filler

Table 4 - 3: Lattice parameters of γ and γ' phases in weld metals of TIG welded IN 738 superalloy with 2 different filler alloys [158]

Parameter	$a_{\gamma}(\mathring{A})$ (hkl-220)	$a_{\gamma'}(\mathring{A})$ (hkl-110)	$\frac{a_{\gamma}-a_{\gamma'}}{a_{\gamma}}\times 100\%$
Rene 41 filler	3.598	3.5458	1.47
IN 718 filler	3.5960	3.5833	0.35

alloys, respectively. This also represents about 4.35% and 1.06% differences between the volumes of unit cells of γ and γ' phases for the two weld metals, respectively. In addition, the result suggests a higher volume change when Rene 41 filler alloy was used. Therefore, it can be reasonably purported that the precipitation of γ' phase from the γ matrix would be accompanied by significant shrinkage and volumetric changes during precipitation, and these are expected to be proportional to the volume of γ' phase. In the present work, differences in the amount of volumetric changes that occurred during weld cooling as a result of variation in γ' volume fraction in the weld metals could be a key factor that contributed to HAZ cracking susceptibility. Shrinkage usually results in tensile stress generation, which could be more easily accommodated by a softer and more ductile weld metal, and prevent excessive tensile loading of the crack-susceptible HAZ.

4.4 Post-Weld Heat Treatment (PWHT) Behaviour of the Laser-Arc Hybrid Welded Material

4.4.1 Introduction

In section 4.2, a complete discussion on the development of an industrially feasible and effective pre-weld thermal treatment procedure (FUMT) was provided. Post-weld heat treatment (PWHT) of fusion welded precipitation strengthened nickel-base superalloys is a standard industry practice. PWHT assists in relieving residual welding stresses, homogenizing the microstructure and restoring mechanical strength [183, 184]. IN 738 superalloy is usually subjected to PWHT consisting of resolutionizing at 1120^{o}C for 2 h followed by aging at 845^{o}C for 24 h. Previous PWHT studies of IN 738 materials that were given other pre-weld heat treatments, and those conducted on other precipitation strengthened nickel-base superalloys revealed the occurrence of PWHT cracking [184-186]. Therefore, it is important to examine the PWHT behaviour of the laser-arc hybrid welded IN 738 material subjected to the pre-weld FUMT treatment. Standard PWHT was applied to the FUMT-treated laser-arc hybrid welded IN 738 superalloy. The performance of the FUMT-treated material after PWHT was also compared to that of SHT-treated material. The microstructure of the FUMT material after PWHT is discussed first, followed by the results of the assessment of PWHT cracking.

4.4.2 Microstructural Analysis of Welds of the FUMT Treated IN 738 Superalloy after Post-Weld Heat Treatment

SEM microstructural analysis of the base alloy, the HAZ and the weld metal of the FUMT-treated material after PWHT was carried out. The microstructure of the base alloy after PWHT is presented in Figure 4-45. It is seen that the γ’ phase is distributed in two

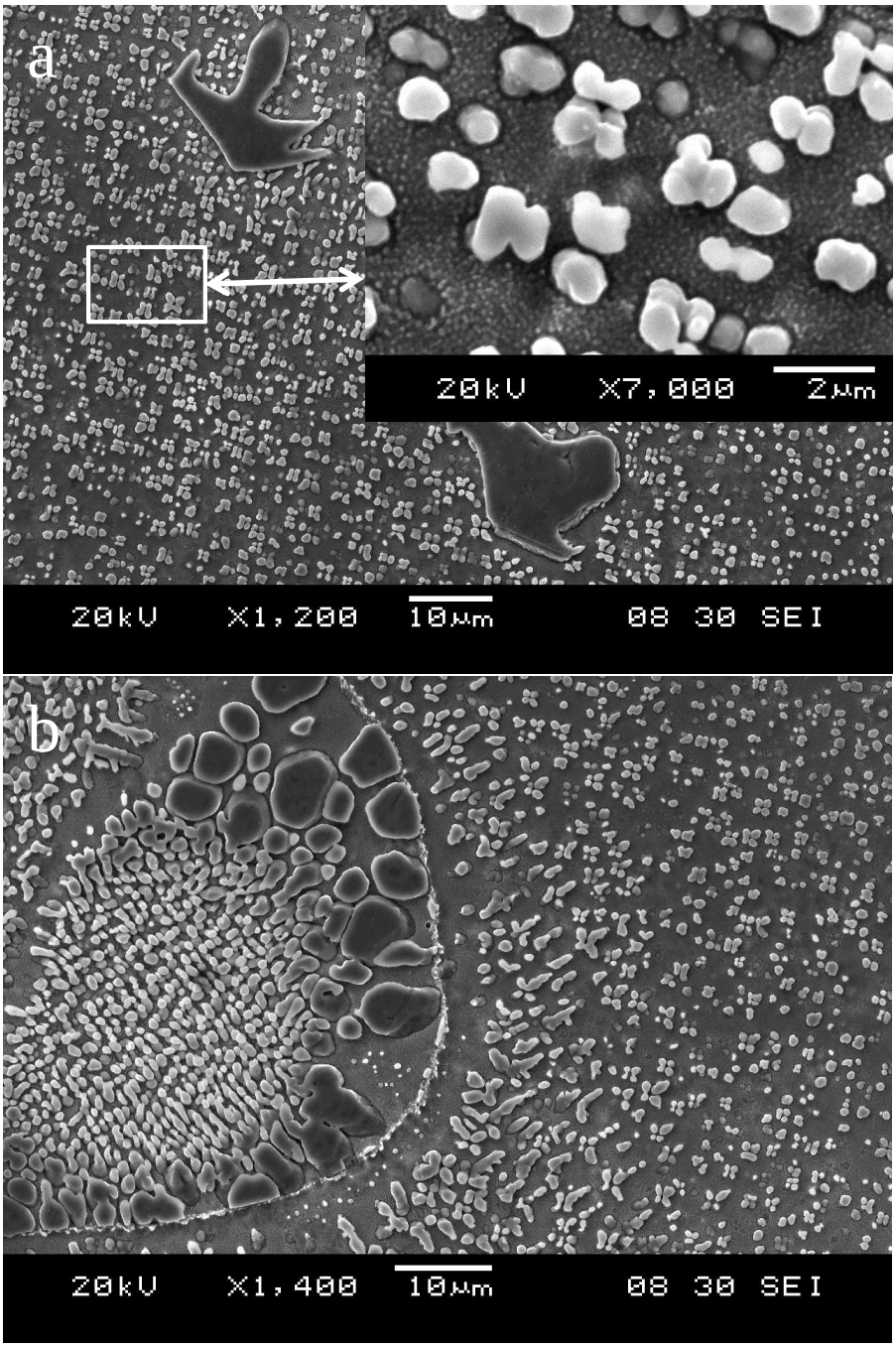

Figure 4 - 45: Microstructure of the base IN 738 material after PWHT showing (a) MC Carbides and γ' precipitate (b) γ-γ'eutectic

modes, namely, primary γ' and very fine secondary γ' precipitates. The blocky MC carbides and γ-γ' eutectic also persisted in the alloy after the PWHT. The SEM image in Figure 4-46 shows a crack path in the HAZ. One of the major characteristics of the HAZ is the significant re-precipitation of γ' in all the regions previously enriched in γ'-forming elements as a result of dissolution of the precipitates during welding. Figure 4-46b shows that the re-precipitation of γ' particles occurred along the crack path where γ' liquation would have occurred during welding.

The microstructure of the fusion zone consisted of Ti-rich MC carbide that was previously identified by TEM in section 4.1 and a bimodal distribution of γ' precipitates. Spherical γ' precipitates of sizes up to about 0.4 μm were observed to be distributed along the interdendritic regions of the fusion zone, while finer spherical precipitates of less than 0.1 μm in size mainly occupied the dendrite core (Figures 4-47a and 4-47b). The observation of larger size γ' particles in the interdendritic region is consistent with the microsegregation pattern in the fusion zone of the as-welded alloy as reported in the earlier part of this work (Section 4.1). The γ'-forming elements Al, Ti, Nb and Ta were observed to partition into the interdendritic regions of the fusion zone. Higher amounts of the γ'-forming elements would result in higher volume fraction and size of γ' precipitates and this could be responsible for the difference in sizes of the precipitates in different regions of the fusion zone. Also, some primary MC carbides that did not dissolve in the fusion zone during welding were observed in the PWHT material as well (Figure 4-47c).

It has been suggested that re-precipitation of γ', such as observed in the post-weld heat treated IN 738 superalloy in this work, depletes the surrounding matrix of γ'-forming elements and causes a decrease in lattice parameter of the matrix, which results in a net

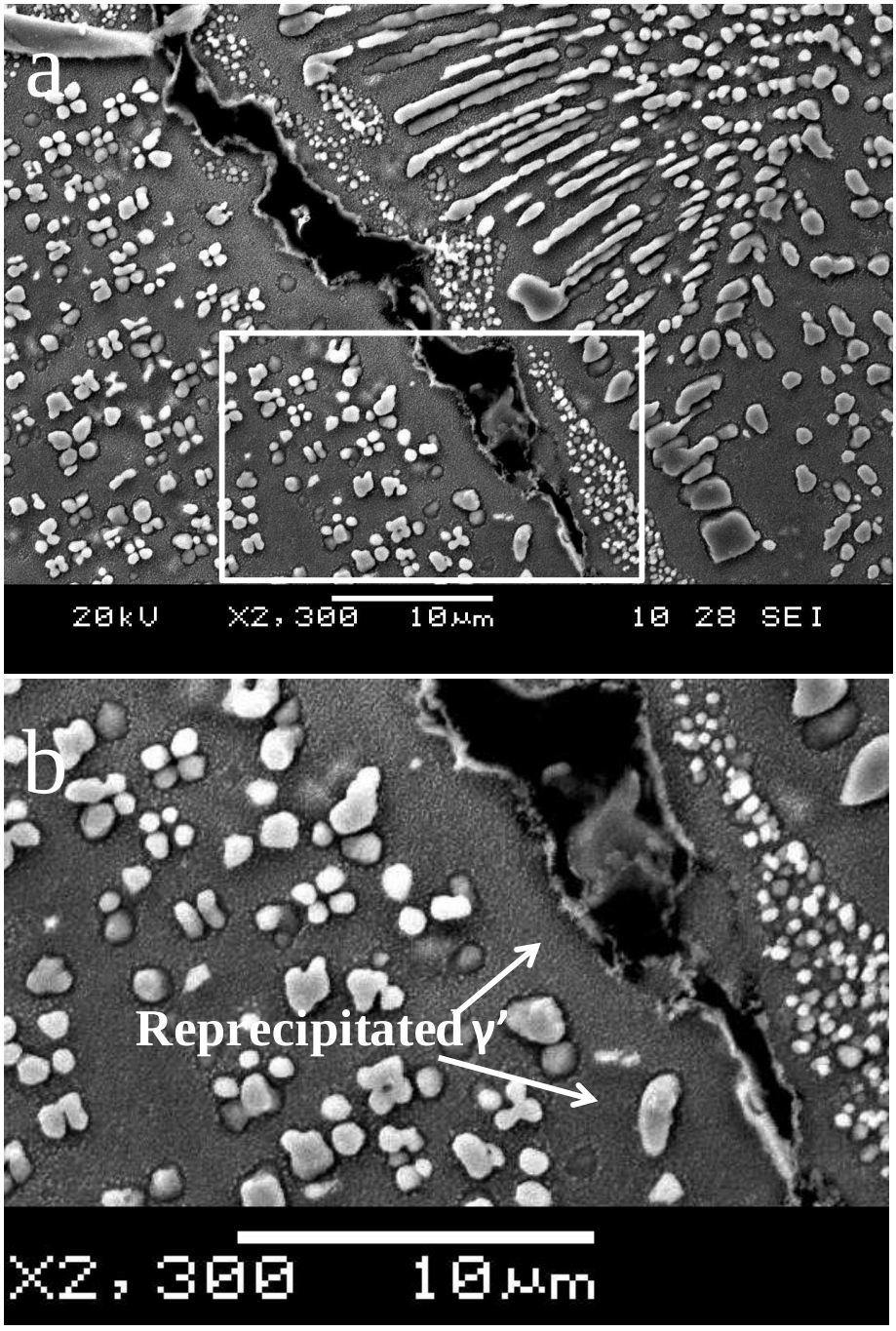

Figure 4 - 46: (a) HAZ microstructure, showing a crack path and re-precipitation of γ' particles in the vicinity of the crack and other HAZ regions (b) the inset in (a)

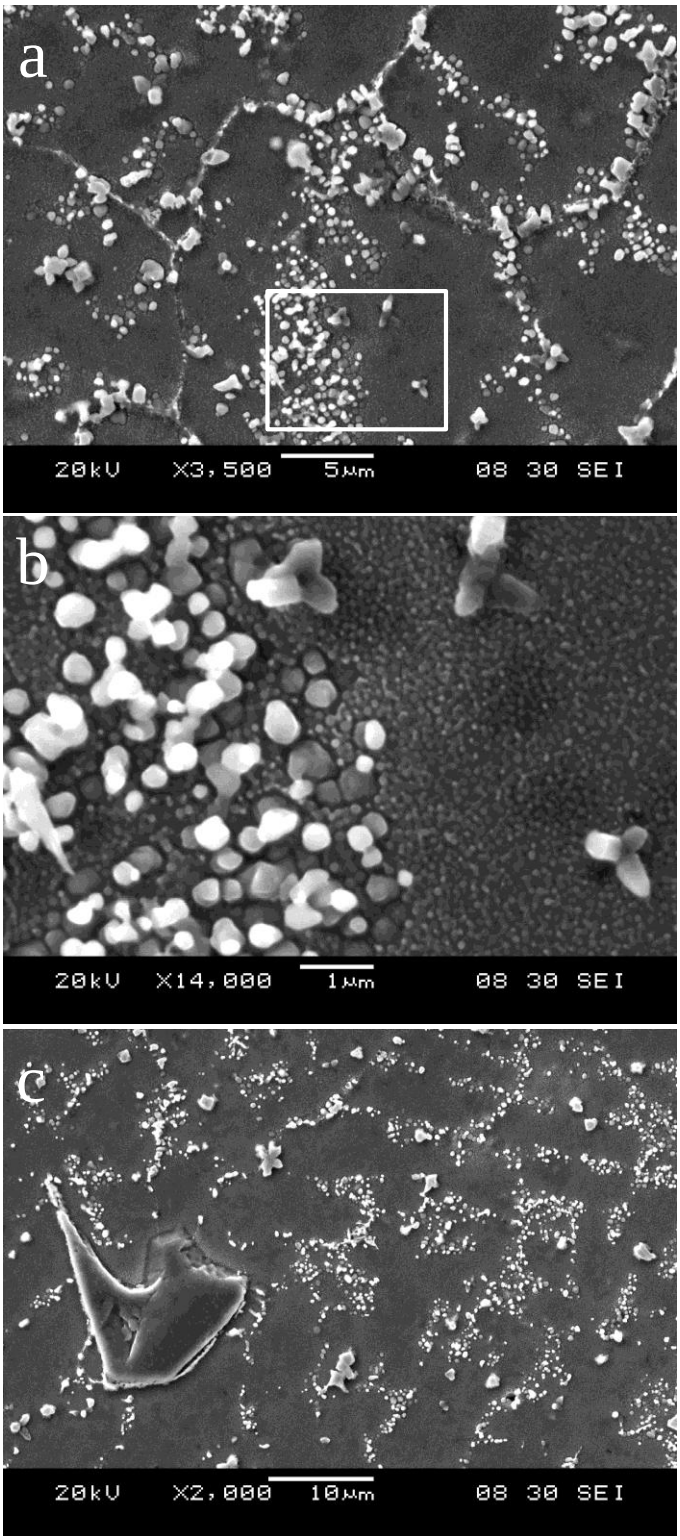

Figure 4 - 47: SEM Micrographs of the fusion zone (FZ) of the PWHT material, showing (a) an overview of the FZ microstructure, (b) the inset in (a), and (c) primary MC Carbide

contraction [183]. This aging contraction generates high stresses and strains in the material. Aging contraction stresses, residual welding stresses and thermal stresses have been identified as key factors contributing to PWHT cracking in many nickel-base superalloys [183-186]. PWHT cracking occurs when these stresses are preferentially relaxed in the HAZ, where the grain boundaries have been previously embrittled by various metallurgical reactions [187]. As mentioned earlier, PWHT cracking susceptibility of the welded alloy was assessed. The results are presented next.

4.4.3 Assessment of PWHT Cracking in the Welded FUMT Material

In section 4.2, it was shown that the new FUMT treatment produced an improvement of up to about 80% reduction in HAZ cracking susceptibility in IN 738 superalloy during laser-arc hybrid welding, compared to the cracking susceptibility of the SHT material. The results of the PWHT that was carried out in this work showed that the resistance of the FUMT material to HAZ intergranular cracking is not compromised during PWHT. Figure 4-48 shows a comparison of total crack lengths (TCLs) measured in the HAZ of post-weld heat treated SHT and FUMT materials, which suggests that the FUMT material is not only resistant to cracking during welding but also resistant to PWHT cracking. The measured TCLs in FUMT materials before and after PWHT showed no significant increase in cracking after PWHT (Figure 4-49). The resistance of the FUMT material to PWHT cracking can be attributed to the superior microstructural characteristics of the newly developed heat treatment, as discussed in detail earlier in section 4.2. Studies have shown that the pre-weld condition of the base metal is an important factor that affects PWHT cracking [187]. Resistance to PWHT cracking was observed in Rene 41 following slow cooling from solution annealing temperature, which produced coarse overaged γ’

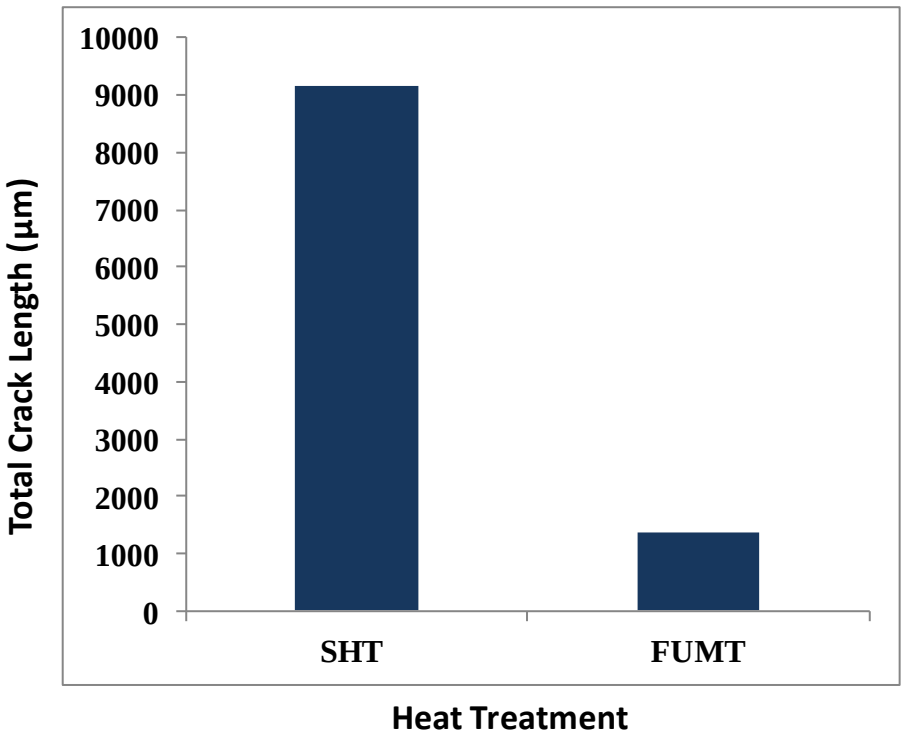

Figure 4 - 48: Total crack lengths in the HAZ of post-weld heat treated SHT and FUMT materials

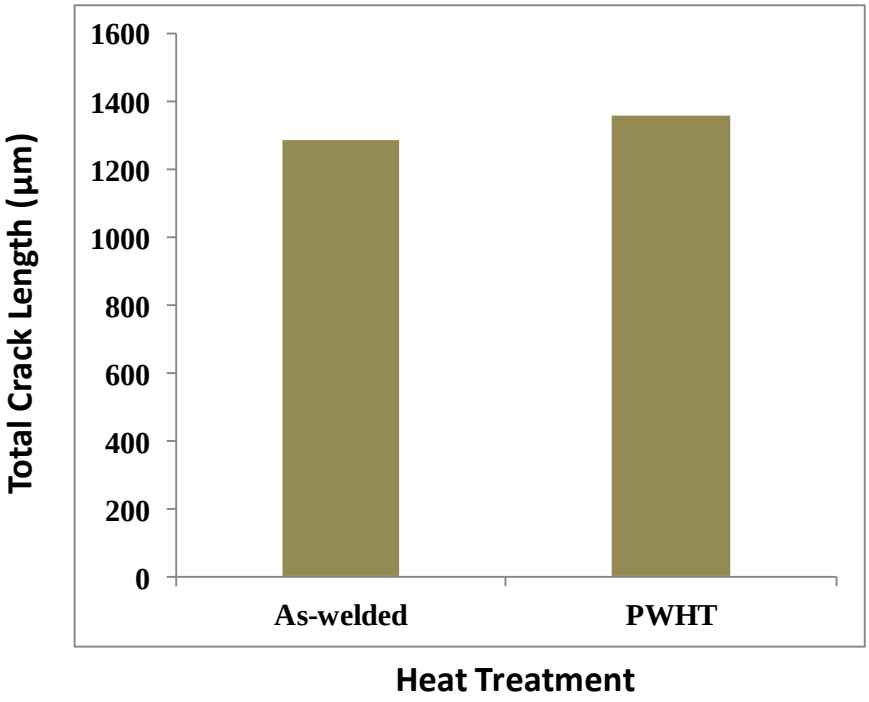

Figure 4 - 49: Total crack lengths in the HAZ of as-welded and post-weld heat treated FUMT material

precipitates and resulted in a softer base metal condition [187, 188]. It was suggested that stress relaxation during PWHT would be transferred to the weaker, overaged and more ductile base metal since the base metal will not undergo any significant increase in strength while the HAZ will during aging. In this work, the FUMT treatment produced an overaged condition in IN 738 superalloy. Figure 4-50 shows the hardness of IN 738 superalloy subjected to the SHT and FUMT treatments. The FUMT material was found to be significantly softer than the SHT material, which suggested that the better performance of the FUMT treatment during PWHT can be related to its superior microstructural characteristics. The current results revealed that the newly developed FUMT treatment procedure, coupled with the selection of an appropriate type of filler alloy would assist in reducing HAZ intergranular cracking both during laser-arc hybrid welding and during PWHT of the laser-arc hybrid welded IN 738 superalloy.

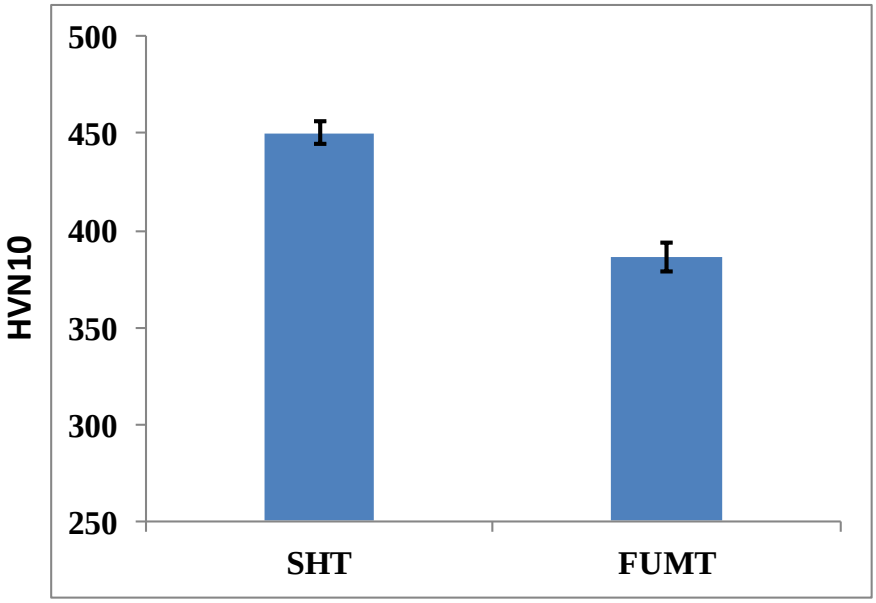

Figure 4 - 50: Vickers hardness of SHT and FUMT base materials

CHAPTER 5

SUMMARY AND CONCLUSIONS

The outcome of this research can be summarized into the following major findings:

1. Laser-arc hybrid welding produced a desirable weld bead shape and appearance in nickel-base IN 738 superalloy, similar to the weld profile of a typical laser beam weld, and no exclusive weld metal cracking was observed. The process was demonstrated to have great potentials for joining IN 738 superalloy and, possibly, other nickel-base superalloys.

2. Elemental partitioning pattern in the fusion zone, as studied by EPMA and the calculation of the total volume fraction of the weld metal that resulted from welding filler alloy consumption, showed that Ti, Ta, Nb, Mo, Al and Zr partitioned into the interdendritic regions. This elemental partitioning pattern is in agreement with existing theoretical and experimental works on microsegregation of different elements during solidification of various alloys.

3. SEM and TEM examination of the weld fusion zone in an SHT-treated IN 738 material welded with IN 718 filler alloy revealed the presence of sub-micrometer size secondary solidification reaction constituents that include MC-type carbides. Formation of MC type carbides in the interdendritic regions of the fusion zone due to microsegregation of carbide-forming elements such as Ti, Ta and Nb was observed in all weldments in this study.

4. Although exclusive fusion zone cracking did not occur during laser-arc hybrid welding of IN 738 superalloy, HAZ intergranular liquation cracking occurred, which is a major problem that needs to be addressed in order to maximize the benefits of the laser-arc welding process and improve the weldability of the alloy.

5. An important factor contributing to intergranular liquation, and hence intergranular liquation cracking, in the HAZ during welding is the significant non-equilibrium liquation of second phases including γ' precipitates, MC carbides and M_2SC sulphocarbides, γ-γ' eutectics and borides that were present in pre-weld materials.

6. The contribution of the decomposition of borides to intergranular liquation in IN 738 superalloy is very significant in that it could increase the temperature range over which non-equilibrium HAZ intergranular liquation occurs through the release of elemental boron into the grain boundaries. Gleeble physical simulation results showed that non-equilibrium liquation was more severe in the vicinity of decomposed borides in the alloy and could occur at temperatures as low as $1150^{o}C$.

7. Elimination of borides in IN 738 superalloy is critical for developing a pre-weld heat treatment that reduces HAZ cracking sensitivity for the alloy. Controlling the

amount of borides in the alloy is achievable during heat treatment by a careful selection of temperature and cooling rate.

8. A major finding in this work is the development of a new pre-weld thermal treatment procedure (1120^{o}C / 16 h / FC), designated as FUMT, which is both industrially feasible and effective in drastically reducing HAZ intergranular liquation cracking in IN 738 superalloy during laser-arc hybrid welding.

9. The newly developed FUMT pre-weld treatment is not only effective in reducing HAZ liquation cracking during welding; laser-arc hybrid welded IN 738 materials that were subjected to the FUMT treatment were also found to be resistant to post-weld heat treatment (PWHT) cracking.

10. Propensity for HAZ cracking in IN 738 superalloy also depends, to a significant degree, on the composition of the filler alloy used during welding. Filler alloys with less Al + Ti + Nb + Ta concentrations were observed to produce welds that were less susceptible to HAZ cracking than those with higher Al + Ti + Nb + Ta concentrations.

11. Thermodynamic temperature step calculation of the volume fraction of γ' particles in weldments made with 5 different filler alloys, namely IN 625, FM 92, IN 718, HY 282 and Rene 41, showed that HAZ cracking varied in the same manner as the calculated value of γ' volume fraction varied with the concentration of Al + Ti + Nb + Ta in the weld metals produced by the filler alloys.

12. While SEM was unable to resolve the γ' particles that were present in the fusion zone, TEM dark field images and SADPs revealed that nanosize γ' particles formed in the weld metals of all the 5 filler alloys used. The TEM data is in agreement with thermodynamic calculations. Variation in HAZ cracking susceptibility when different filler alloys were used can be reasonably attributed to variation in the extent of precipitation hardening produced by the re-precipitation of γ' phase in the weld metals.

13. Softer weld metals (with lower γ' volume fraction) produced by lower Al + Ti + Nb + Ta concentration appear to accommodate the on-cooling tensile stresses to a greater extent, compared to weld metals with higher Al + Ti + Nb + Ta concentration, which tend to offer more restraint to plastic deformation, thereby transferring most of the tensile stresses to the HAZ.

14. Shrinkage, and the consequent volumetric changes, due to γ' precipitation in the weld metals could have contributed to excessive tensile loading of the crack-susceptible HAZ, which would also depend on the volume fraction of precipitated γ' particles.

15. The newly developed FUMT treatment procedure, coupled with the selection of an appropriate type of filler alloy would assist, significantly, in reducing HAZ intergranular cracking both during laser-arc hybrid welding and during PWHT of the laser-arc hybrid welded IN 738 superalloy.

CHAPTER 6

SUGGESTIONS FOR FUTURE WORK

1. All welding runs in this present work were carried out using the same set of welding parameters, while the IN 738 material was subjected to different pre-weld heat treatments, resulting in different microstructural characteristics. Additionally, filler alloys of different compositions were used to alter the composition of the weld metals. The improvement in weldability that was realized in this work resulted from microstructural modifications. However, weldability improvement can also be achieved by process optimization. The welding parameters used in this work were results of several preliminary trials performed at the beginning of the work, which produced sound joints. Nevertheless, the welding might not have been conducted under optimum process conditions. It is therefore recommended that process parameter optimization should be carried out in order to determine the effect of welding parameters on weldability.

2. This present work focused on laser-arc hybrid welding of polycrystalline nickel-base IN 738 superalloy. However, the alloy is also manufactured in forms of directionally solidified (DS) and single crystal (SX) alloys. It is recommended that this study be extended to studying the effect of grain structure on microstructural response and weldability of the alloy during laser-arc hybrid welding.

3. The results of this work suggest that laser-arc hybrid welding has a great potential for joining nickel-base superalloys for aerospace applications. Due to the limited information about the joining of nickel alloys by this process, it is required that extensive research be carried out on other nickel-base alloys to provide appropriate information on the weldability of each alloy during the process.

4. The new pre-weld thermal treatment procedure that was developed in this work was found to be effective in drastically reducing HAZ intergranular liquation cracking during laser-arc hybrid welding. Since the mechanism of HAZ liquation cracking is the same in the alloy irrespective of the type of fusion welding technique used, it is suggested that the new heat treatment be applied to other fusion welding techniques. This should also require significant weldability studies.

5. A comprehensive study of the mechanical behaviour of laser-arc hybrid welded IN 738 superalloy subjected to the newly developed heat treatment is recommended. This can include high and low temperature tensile testing, high cycle and low cycle fatigue studies, creep testing, etc.

REFERENCES

[1] E.W. Ross and C.T. Sims: "Nickel-Base Alloys" in Superalloys II: High Temperature Materials for Aerospace and Industrial Power, A Wiley-Interscience publication, 1987, p.97

[2] M. Prager and C. S. Shira: Weld. Res. Council Bull, 1968, vol. 128, p.1

[3] A Thakur, N.L. Richards and M.C. Chaturvedi: International Journal for the Joining of Materials, 2003, vol. 15, p.21

[4] O.A. Ojo, N.L. Richards and M.C. Chaturvedi: Mater. Sci. Technol., 2004, vol. 20, p.1021

[5] E.A. Bonifaz and N.L. Richards: International Journal of Applied Mechanics, 2010, vol. 2, p.807

[6] K.C. Antony and G.W. Goward: Superalloys 1988, The Metallurgical Society, p.745

[7] W.M. Steen: J. Appl. Phys., 1980, vol. 51, p.5636

[8] M. Eboo, W.M. Steen and J. Clarke: Advances in Welding Processes Fourth International Conference, Harrogate, 9-11 May 1978, p.257

[9] W.M. Steen and M. Eboo: Metal Construction, 1979, vol. 7-7, p.332

[10] B. Ribic, T.A. Plamer and T. DebRoy: International Materials Review, 2009, vol. 54, p.223

[11] C. Bagger and F.O. Olsen: Journal of Laser Applications, 2005, vol. 17, No. 1, p.2

[12] H. Staufer: Weld. J., 2007, vol. 86, No. 10, p.36

[13] Mahrle and E. Beyer: Journal of Laser Applications, 2006, vol. 18, p.169

[14] T. Ishide, S. Tsubota, M. Watanabe and K. Ueshiro: Journal of the Japan Welding Society, 2003, vol. 72, No. 1, p.22

[15] J. Defalco: Weld. J., 2007, vol. 86, No 10, p.47

[16] S. Webster: Ironmaking and Steelmaking, 2007, vol. 35, No. 7, p.496

[17] R. Brockmann: Welding and Cutting, 2009, No. 4, p.192

[18] A.N. Nazmul and K. Young-Pyo: Australasian Welding Journal, 2005, vol. 50, p.22

[19] E.F. Bradley, Superalloys: A technical Guide, ASM International, Metals Park, OH, 1988

[20] Alloy IN 738: A Technical Data, INCO, New York, p.1

[21] G. C. Bieber, R.J. Mihalisin, 2nd International Conference on the Strength of Metals and Alloys, Asilomer, ASM Vol. IV, p. 1031

[22] O.A. Ojo: Ph.D. Thesis, University of Manitoba, Canada, 2004

[23] A.T. Egbewande: MSc Thesis, University of Manitoba, Canada, 2008

[24] O.T. Ola: MSc Thesis, University of Manitoba, Canada, 2010

[25] W. F. Smith: Structure and Properties of Engineering Alloys, 2nd Ed, New York : McGraw-Hill, c1993, p.504

[26] W. Hoffelner, E. Kny, R. Stickler, W.J. McCall: The Effect of Aging Treatment on the Microstructure of the Ni-base Superalloy IN 738, Z. Werkstofftech 1979, Vol. 10, p. 84

[27] R.C. Reed: The Superalloys: Fundamentals and Applications, Cambridge University Press, 2006, p. 35

[28] R.F. Decker: Strengthening Mechanisms in Nickel-Base Superalloys, Climax Molybdenum Company Symposium, Zurich, May 5-6, 1969

[29] D.S. Paulonis, J.M. Oblak and D.S. Duvall: Trans. ASM, 1969, Vol. 62, p.611

[30] M.J. Donachie and S.J. Donachie, Superalloys: A Technical Guide, 2nd Edition, ASM International, 2002 p.31

[31] T.J. Garroshen, G.P. McCarty: Metall. Mater. Trans., 1985, Vol. 16A, p.1213

[32] W.C. Hagel, H.J. Bettie: Iron and Steel Institute Special Report, London, 64, p.98

[33] J.M. Fragomeni: Recent Advances in Solids and Structures, 1999, Vol. 398, p.179

[34] B. Reppich, P. Schepp and G. Wehner: Acta Metall., 1982, Vol. 30, p.95

[35] E. Nembach, S. Schanzer, W. Schroer and K. Trinckauf: Acta Metall., 1988, Vol. 36, No. 6, p.1471

[36] A.J. Ardell: Metall. Trans. A, 1985, Vol. 16A, p.2131

[37] O. Wouters: Rijksuniversiteit Groningen, "Dislocations and Precipitation Hardening" in Plasticity in Aluminum Alloys at Various Length Scales, Ph.D. Thesis, 1997, p.25

[38] J.L. Castagne: J. De. Physique, 1966, Vol. 27, p.C3 233

[39] A.J. Ardell, V. Munjal and D.L. Chellman: Metall. Trans. A, 1976, Vol. 7A, p.1263

[40] A. Melander and P.A. Person: Metal. Sci. J., 1978, Vol. 13, p.391

[41] J.L. Castagne, F. Lecroisey and A. Pineau: C. R. Acad. Sci. Paris, 1968, Vol. 266, p.510

[42] V. Munjal and A.J. Ardell: Acta Metall., 1975, Vol. 23, p.513

[43] J.S. Zhang, Z.Q. Hu, Y. Murata, M. Morinaga, N. Yukawa: Metall. Mater. Trans., 1993, Vol. 24A, p. 2443

[44] R. Sallemark, Progress Report 2 Cost 50 Programme Sweden, 1975.

[45] R. Rosenthal, D.R.F. West: Mater. Sci. Technol., 1999, Vol. 15, p.1387.

[46] J.M. Larson: Metall. Mater. Trans., 1976, Vol. 7A, p.1497

[47] W.C. Johnson, J.E. Doherty, B.H. Kear, A.F. Giamei: Scripta Metall., 1974, Vol. 8, p.971

[48] J.E. Doherty, B.H. Kear, A.F. Giamei, C.W. Steinke: "Effect of Surface Chemistry on Grain Boundary Strength", Grain Boundaries in Engineering Materials, Claitor's Publishing Div., 1975

[49] A.W. Thompson: Acta Metall., 1975, Vol. 28, p.607

[50] J.W. Schultz, University of Michigan, Uni. Microfilms, Ann Arbor, PhD Thesis, 1965

[51] H.R. Zhang, O.A. Ojo, M.C. Chaturvedi: Scripta Mater., 2008, Vol.58, p.167

[52] K. Masubuchi: Encyclopedia of Materials Science and Engineering, M.B. Bever (Editor), 1986, Vol. 7, p.5280

[53] S. Kuo: Welding Metallurgy, 2nd ed., John Wiley & Sons Inc., Hoboken, 2003, p 9.

[54] D.L. Olson, T.A. Siewert, S. Liu and G.R. Edwards (eds): Overview of Weld Discontinuities, in ASM Handbook, Vol. 6: Welding, Brazing and Soldering, p. 1073

[55] K. Easterling: "Introduction to the Physical metallurgy of Welding", 2nd Edition, Copyright Butterworth-Heinemann, 1992

[56] K. Masubuchi: ASM Handbook: Welding, Brazing and Soldering, 1993, Vol. 6, p.1094

[57] G.J. Davies and J.G. Garland: Int. Metall. Rev., 1975, Vol. 20, p.83

[58] D.C.G. Lees: J. Inst. Metals, 1946, Vol. 72, p.343

[59] A.R.E. Singer and P.H. Jennings: J. Inst. Metals, 1947, Vol. 73, p. 273

[60] M.J. Cieslak: Cracking Phenomena Associated with Welding, ASM Handbook: Welding Brazing and Soldering, 1993, Vol. 6, p88

[61] K. Nakata and F. Matsuda, Trans JWRI, 1995, Vol. 24, p.83

[62] R.G. Baker: Philosophical Transactions of the Royal Society of London, Series A, Mathematical and Physical Sciences, 1976, Vol. 1307, p.207

[63] M.C. Chaturvedi: Materials Science Forum, , 2007, Vols. 546-549p.1163

[64] J.J. Pepe and W.F. Savage: Effects of Constitutional Liquation in 18-Ni Maraging Steel Weldments, Weld. J., 1967, Vo146 (No. 9), p 411-s

[65] W.A. Owczarski, D.S. Duvall and C.P. Sullivan: Weld. J., 1967, Vol. 46, p.423s.

[66] B. Weiss, G.E. Grotke and R. Stickler: Weld. J., 1970, Vol. 49, p.471s.

[67] J.A. Brooks: Weld. J., 1974, Vol. 53, p.517.

[68] R. Nikkalil, N.L. Richards and M.C. Chaturvedi: Metall. Mater. Trans. A, 1993, Vol. 24A, p.1169.

[69] B. Radhakrishnan and R.G. Thompson: Metall. Mater. Trans. A, 1993, Vol. 24A, p.1409.

[70] K.R. Vishwakarma and M.C. Chaturvedi: in E.A. Loria (Ed.), Superalloys 718, 625, 706 and Derivatives 2005, The Minerals, Metals and Materials Society, 2005, p.637

[71] W. Chen and M.C. Chaturvedi: Metall. Mater. Trans. A, 1998, Vol. 29A, p.743

[72] M. McLean and A. Strang: Metals Technol., 1984, Vol. 11, p. 454

[73] E.D. Hondros and M.P. Seah: in R.W. Chan (Ed): Physical Metallurgy, 3rd edition, North Holland, Amsterdam, 1984

[74] M.P. Seah and E.D. Hondros: Proc. R. Soc., 1973, Vol. 335A, p.191

[75] D. McLean: Grain Boundaries in Metals, Clarendon Press, Oxford, 1957

[76] J.H. Westbrook and K.T. Aust: Acta Metall., 1963, Vol. 11, p.1115

[77] K.T. Aust, R.E. Hanneman, P. Nissen and J.H. Westbrook: Acta Metall., 1968, Vol. 16, p.291

[78] R.L. Eadie and K.T. Aust: Scripta Metall., 1970, Vol. 4, p.641

[79] K.T. Aust: Canadian Metallurgical Q., 1974, Vol. 13 (1), p.133

[80] D.C. Paine, G.C. Weatherly and K.T. Aust: J. Mater. Sci., 1986, Vol. 21, p.4257

[81] X. Huang, M.C. Chaturvedi, N.L. Richards and J. Jackman: Acta Mater., 1997, Vol. 45, p.3095

[82] L. Karlsson and H. Norden: Acta Metall. 1988, Vol. 36, p.1

[83] L. Karlsson and H. Norden: Acta Metall. 1988, Vol. 36, p.13

[84] L. Karlsson: Acta Metall. 1988, Vol. 36, p.25

[85] L. Karlsson and H. Norden: Acta Metall. 1988, Vol. 36, p.35

[86] R.D. Campbell and D. W. Walsh: “Weldability Testing”, in ASM Handbook: Welding, Brazing and Soldering, Vol. 6, 1993, p.603

[87] "Weldability Testing," Chapter 4, Welding Handbook, Vol. 1, 8th ed., American Welding Society, 1987

[88] R.D. Stout and W.D. Doty: Weldability of Steels, Welding Research Council, 1987

[89] C.D. Ludin, A.C. Lingenfelter, G.E. Grotke, G.G. Lessmann and S.J. Matthews: The Varestraint Test, Weld. Res. Counc. Bull., No. 280, 1982

[90] E.F. Nippes and W.F. Savage: Weld. J., 1955, Vol 34 (No. 4), p 183-s

[91] E.F. Nippes, W.F. Savage. and G. Grotke: Bulletin Series Vol 33 (No. 2), Welding Research Council, 1957

[92] E.F. Nippes, W.F. Savage, and J.M. Paez: Weld. J., 1960, Vol 39 (No. 1), p 31-s

[93] K.C. Wu: Weld. J., 1963, Vol 42 (No. 9), p 392-s

[94] R.F. Fastini and M. Semchyshen: The Effect of Molybdenum on the Continuous Cooling Transformation of a 0.40% Carbon Steel, ASM Trans. Quart., Sept 1964

[95] D.G. Howden, Isothermal Transformation Characteristics of a Low-Alloy Steel Using a Weld Thermal Cycle Simulator, Can. Metall. Quart., 1967 , Vol 6 (No. 3)

[96] C.F. Meitzner and A.W. Pense: Weld. J., 1969, Vol 48 (No. 10), p.431-s

[97] A.W. Dix and W.F. Savage: Weld. J., 1973. Vol 52 (No. 3), p 135-s

[98] S.J. Matthews: Weld. J., 1968. Vol 47 (No. 4), p 155-s

[99] K.C. Wu and T.A. Krinke: Weld. J., 1968. Vo147 (No. 6), p 332-s

[100] W.P. Hughes and T.F. Berry: Weld. J., 1967, Vol 46 (No. 8), p 361-s

[101] Anon, Computerized Thermal and Mechanical Testing Machine a Significant Asset in Research, Development and Production, Industrial Heating, 1986, Vol. 53 (No 12), p.28

[102] L.O. Osoba: Ph.D. Thesis, University of Manitoba, Canada, 2012

[103] T. Graf and H. Staufer: Weld J., 2003, Vol. 82, p.42

[104] K. Hakansson, T. Siwecki and D. Stemne: Welding in the World, 2008, Vol. 52, p.103

[105] A. Nonn, W. Dahl and W. Bleck: Engineering Fracture Mechanics, 2008, Vol. 75, p.3251

[106] E. W. Reutzel: Advantages and disadvantages of arc and laser welding, in Hybrid Laser-Arc Welding, F.O. Olsen (ed.), Woodhead Publishing Limited, Abington Hall, Granta Park, Great Abington, Cambridge, UK, 2009, p.3

[107] D.S. Howse, R.J. Scudamore and G.S. Booth: Proceedings of the Fifteenth International Offshore and Polar Engineering Conference, Seoul, Korea, June 15-19 2005, pp.90-95

[108] C. Thorny, T. Seefeld and F. Vollertsen: Welding in the World, 2005, Vol. 49, p.88

[109] A. Mahrle and E. Beyer: Heat sources of hybrid laser–arc welding processes, in Hybrid Laser-Arc Welding, F.O. Olsen (ed.), Woodhead Publishing Limited, Abington Hall, Granta Park, Great Abington, Cambridge, UK, 2009. P.47

[110] J. Greses, P.A. Hilton, C.Y. Barlow and W.M. Steen: 'Spectroscopic studies of plume/ plasma in different gas environments', Proceedings of the International Congress on Lasers and Electro-Optics (ICALEO 2001), p.10

[111] K.E. Lahti: Svetsaren, 2003, Vol. 58, p.22

[112] J. Pilarczyk, M. Banasik and J. Dworak: Welding International, 2008, Vol. 22, p.388

[113] L.E. Stridh: Materials Science Forum, 2007, Vols. 539-543, p.3991

[114] M.S. Surendar: Yosetsu Gakkai Shi, 2010, Vol. 79, p.14

[115] T. Ishide, S. Tsubota and M. Watanabe: Proc. of SPIE (First International Symposium on High-Power Laser Macroprocessing), Osaka, JLPS, 2002, Vol. 4831, p.347

[116] M. Kutsuna and L. Chen: IIW, 2002, Doc XII-1708-02

[117] J.R. Biffin and R.P. Walduck: Proceedings EUROJOIN 2, 2nd European Conference on Joining Technology, Firence, Italy, 16-18 May 1994, p.295

[118] S.E. Nielsen, M.M. Andersen, J.K. Kristensen and T.A. Jensen: International Institute of Welding, IIW Document, XII 1731-02, 2002

[119] S. Fujinaga, R. Ohashi, S. Katayama and A. Matsunawa: LAMP 2002 Proceedings, First International Symposium on High Power Laser Macroprocessing – Proc. SPIE, 2002, Vol. 4831, pp.301-306

[120] L. Liming, W. Jifeng and S. Gang: Mater. Sci. and Eng. A, 2004, Vol. 381, p.129

[121] C.V. Hyatt, K.H. Magee, J.F. Porter, V.E. Merchant and J.R. Matthews: Weld. J., 2001, Vol. 80, no. 7, p.163s

[122] G. Campana, A. Fortunato, A. Ascari, G. Tani and L. Tomesani: Journal of Materials Processing Technology, 2007, Vol. 191, p.111

[123] K.H. Magee, V.E. Merchant and C.V. Hyatt: Proceedings of ICALEO 1990, Boston, MA (Laser Institute of America, 1990), pp. 382-399

[124] T. Jokinen, P. Jernstrom, M. Karhu, I. Vanttaja and V. Kujanpaa: Proc. 1st Int. Symp. on 'High-power laser macroprocessing', Osaka, Japan, May 2002, Osaka University, p.307

[125] Y. Naito, S. Katayama and A. Matsunawa: First International Symposium on High-Power Laser Macroprocessing – Proceedings of SPIE, 2003, Vol. 4831, p.357

[126] A. Fellman, P. Jernstrom and V. Kujanpaa: Proceedings 9th NOLAMP, Conference on Laser Materials Processing in the Nordic Countries, Trondheim, Norway, 4-6 August 2003, p.103

[127] J. Alexander and W.M. Steen: Institution of Metallurgists, Great Britain: Joining of Metals; Practice and Performance, Spring Residential Conference, 1981, No. 18, p.155

[128] S. Katayama, Y. Naito, S. Uchiumi and M. Mizutani: Transactions of JWRI, 2006, Vol. 35, No. 1, p.13

[129] M. Gao and X. Y. Zeng, Effect of shielding gas on hybrid laser–arc welding, in Hybrid Laser-Arc Welding, F.O. Olsen (ed.), Woodhead Publishing Limited, Abington Hall, Granta Park, Great Abington, Cambridge, UK, 2009, p.85

[130] D. Petring, C. Fahrmann, N. Wolf and R. Poprawe: Proc of the 22nd Int. Congress on Applications of Lasers and Electro-Optics (ICALEO), Jacksonville, LIA, 2003, Section A, 1-10 (CD:301)

[131] H. Staufer, Industrial robotic application of laser-hybrid and laser-hybrid-tandem welding, in Hybrid Laser-Arc Welding, F.O. Olsen (ed.), Woodhead Publishing Limited, Abington Hall, Granta Park, Great Abington, Cambridge, UK, 2009, p.192

[132] J. K. Kristensen, Shipbuilding applications of hybrid laser–arc welding, in Hybrid Laser-Arc Welding, F.O. Olsen (ed.), Woodhead Publishing Limited, Abington Hall, Granta Park, Great Abington, Cambridge, UK, 2009, p.178

[133] L. Liu, Hybrid welding of magnesium alloys, in Hybrid Laser-Arc Welding, F.O. Olsen (ed.), Woodhead Publishing Limited, Abington Hall, Granta Park, Great Abington, Cambridge, UK, 2009, p.143

[134] Jiaming Ni, Zhuguo Li, Jian Huang and Yixiong Wu: Materials and Design, 2010, Vol. 31, p.4876

[135] C. Pascal, C. Merlet, R-M. Marin-Ayral, J-C. Tedenac and B. Boyer: Microchim. Acta, 2004, vol. 145, p.147

[136] N. Saunders, X. Li, P. Miodownik and J. Ph. Schille: "Proc. Symp. Materials Design Approaches and Experiences", eds J.-C. Shao et. al., 2001, p.185, Warrendale, PA, TMS

[137] G.D. Pigrova: Metal Science and Heat Treatment, Plenum Publishing Corporation, 1985, vol. 27 (9), p.750

[138] Y.N. Ahn and C. Kim: Materials Science Forum, 2011, Vol. 695, p.247-

[139] M.C. Flemings, Solidification Processing, McGraw-Hill, New York, 1974.

[140] P.N. Quested and M. McLean: Conf. on Solidification Technology in the Foundry and Cast House, The Metals Society, London, 1980, p.586

[141] L. Liu and F. Sommer: Scripta Metallurgica et Materialia, 1994, Vol. 30, p.587

[142] H.D. Brody: in Advances in Welding Science and Technology, S.A. David, ed., ASM international, Metals Park, OH, 1986, p.83

[143] R. Nikkalil, N.L. Richards and M.C. Chaturvedi: Metallurgical Transactions A, 1993, vol. 23A, p.1169

[144] E. Scheil: Z. Metallk., 1942, vol. 34, p.70

[145] J.N. DuPont, C.V. Robino, A.R. Marder and M.R. Notis: Metall. Mater. Trans. A, 1998, vol. 29 A, p.2797

[146] H.D. Brody and M.C. Flemings: Trans. AIME, 1966, vol. 236, p.615

[147] O.A. Ojo, N.L. Richards and M.C. Chaturvedi: Metall. Mater. Trans. A, 2006, vol. 37A, p.421

[148] R.K. Sidhu, O.A. Ojo and M.C. Chaturvedi: Metall. Mater. Trans. A, 2007, vol. 83A, p.858

[149] L. O. Osoba, R.G. Ding and O.A. Ojo: Materials Characterization, 2012, vol. 65, p.93

[150] G.A. Knornovsky, M. J. Cieslak, T.J. Headley, A.D. Romig, Jr., and W.F. Hammeter: Metall. Trans. A, 1989, Vol. 20A, p.2149

[151] R.G. Thompson, D.E. Mayo and B. Radhakrishnann: Metall. Trans. A, 1991, vol. 22A, p.557

[152] Y. Nakao and K. Shinozaki: Proc. Int. Conf. on High Temperature Materials, Liege, Belgium, 1990, p.24

[153] D. Turnbull: J. Chem. Physiol., 1950, vol. 18, p.198

[154] W.F. Savage, C.D. Lundin, and A.H. Aronson: Weld. J., 1965, vol. 44, p.175s

[155] W.F. Savage and A.H. Aronson: Weld. J., 1966, vol. 45, p.85s

[156] W.F. Savage, C.D. Lundin, and T.F. Chase: Weld. J., 1968, vol. 47, p.522s

[157] L. Liu, B.L. Zhen, A. Banerji, W. Reif and F. Sommer: Scripta Metall. Mater., 1994, vol. 30, p.593

[158] K. Banerjee, N.L. Richards and M.C. Chaturvedi: Metall. Mater. Trans. A, 2005, Vol. 36A, p.1881

[159] W. Wallace, R.T. Holt and T. Terada: Metallography, 1973, vol. 6, p.511

[160] ASM Handbook: "Welding of Nickel Alloys," Welding, Brazing and Soldering, 1993, Vol. 6, p.740

[161] A.T. Egbewande, H.R. Zhang, R.K. Sidhu and O.A. Ojo, Metall. Mater. Trans. A, vol. 40A, 2009, p.2695

[162] K. Masubuchi: Analysis of Welded Structures, International Series on Materials Science and Technology, Vol. 33, Copyright Pergamon Press Ltd, 1980, p.149

[163] K.C. Antony and J.F. Radavich: Superalloy: Metallurgy and Manufacture, B.H. Kear Ed., Claitor's Pub. Division, 1976, p.137

[164] D. McLean: Grain Boundaries in Metals, Clarendon Press, Oxford, 1957

[165] E.D. Hondros, M.P. Seah: Physical Metallurgy, R.W. Chan (Ed), 3rd edition, North Holland, Amsterdam, 1984

[166] T.M. Williams, A.M. Stoneham and D.R. Harries: Met. Sci., 1976, Vol. 10, p.14

[167] H.B. Aaron and G.R. Kotler: Metall. Trans., 1971, Vol. 2, p.393

[168] M.J. Whelan: Metal Science Journal, 1969, Vol. 3, p.95

[169] A.R. Eivani, H. Ahmed, J. Zhou and J. Duszczyk: Philosophical Magazine, 2010, Vol. 90, No. 21, p.2865

[170] J.R. Davis: ASM Specialty Handbook – Nickel, Cobalt and Alloys, 2000, p.267

[171] Y.E. Wu and Y.T. Wang: Journal of Materials Engineering and Performance, 2010, Vol. 19, p.1362

[172] M.O. Okubo and H. Uryu: Welding International, 1996, Vol. 10. No. 4, p.274

[173] L.M. Pike: Superalloys 2008, The Minerals, Metals and Materials Society, 2008, p.191

[174] C. Ravindran and M.C. Chaturvedi: Metall. Trans. A, 1975, Vol. 6, No. 1, p.213

[175] V.P. Demyantsevich: Welding Production, 1969, Vol. 14, No. 3, p.1

[176] O.A. Ojo and M.C. Chaturvedi: Mater. Sci. Eng. A, 2005, Vol. 403, p.77

[177] J.M. Fragomeni: Recent Advances in Solids and Structures, 1999, Vol. 398, p.179

[178] B. Reppich, P. Schepp and G. Wehner: Acta Metall., 1982, Vol. 30, p.95

[179] E. Nembach, S. Schanzer, W. Schroer and K. Trinckauf: Acta Metall., No. 6, 1988, Vol. 36, p.1471

[180] A.J. Ardell: Metall. Trans. A, 1985, Vol. 16A, p.2131

[181] T.F. Chase: “High-Temperature Properties of Welded Cast Co-Base Alloys”, Superalloys-Processing; Proceedings of The Second International Conference, The Metallurgical Society AIME, September 18-20, 1972, Seven Springs Mountain Resort, Champion, PA, p.R1

[182] M.I. Gitgarts, A.V. Tolstoy and V.V. Ivashin: Fiz. Metal. Metalloved, 1972, Vol. 33, No. 4, p.820

[183] L.C. Lim, J.-Z. Yi, N. Liu and Q. Ma: Mater. Sci. Technol., 2002, Vol. 18, p.407

[184] R.K. Sidhu, N.L. Richards and M.C. Chaturvedi: Mater. Sci. Technol., 2008, Vol. 24, No. 5, p.529

[185] Y. Nakao: Trans. Japan Weld. Soc., 1988, Vol. 19, No. 1, p.66

[186] R. Kayacan, R. Varol and O. Kimilli: Mater. Res. Bull., 2004, Vol. 39, p.2171

[187] R. Thamburaj, W. Wallace and J.A. Goldak: Int. Metals Rev. 1983, Vol. 28, No. 1, p.1

[188] E.G. Thompson, S. Sunez and M. Prager: Weld. J, 1968, Vol. 47, No. 7, p.299-s

RESEARCH CONTRIBUTIONS

CONTRIBUTIONS FROM THIS CURRENT WORK

- US PATENT Application No. 61/858042: O.T. Ola, O.A. Ojo, M.C. Chaturvedi and A. Birur: *Pre-Weld Heat Treatment of γ' Precipitation Strengthened Nickel-Based Superalloys*. (Application Filed)

- O.T. Ola, O.A. Ojo and M.C. Chaturvedi: *The Role of Filler Alloy Composition on Laser-Arc Hybrid Weldability of Nickel-Base IN 738 Superalloy,* Materials Science and Technology (Submitted)

- O.T. Ola, O.A. Ojo and M.C. Chaturvedi: *Laser-Arc Hybrid Weld Microstructure in Nickel-Base IN 738 Superalloy,* Materials Science and Technology, 2013, Vol. 29, No 4, pp.426-438

OTHER CONTRIBUTIONS

Papers in Referred Journals

- O.T. Ola, O.A. Ojo and M.C. Chaturvedi. *Effect of Deformation Mode on Hot Ductility of A γ' Precipitation Strengthened Nickel-Base Superalloy,* Materials Science and Engineering A. (Accepted on June 18, 2013)

- O.T. Ola, O.A. Ojo, P. Wanjara and M.C. Chaturvedi: *A Study of Linear Friction Weld Microstructure in Single Crystal CMSX-486 Superalloy*, Metallurgical and Materials Transactions A, 2012, Vol. 43, No 3, pp.921-933

- O.T. Ola, O.A. Ojo, P. Wanjara and M.C. Chaturvedi: *Enhanced Resistance to Weld Cracking by Strain-Induced Rapid Solidification during Linear Friction Welding,* Philosophical Magazine Letters, 2011, Vol. 91, pp.140-149

- O.T. Ola, O.A. Ojo, P. Wanjara and M.C. Chaturvedi: *Analysis of Microstructural Changes Induced by Linear Friction Welding in a Nickel-Base Superalloy,* Metallurgical and Materials Transactions A, 2011, Vol. 42A, pp.3761-3777

Papers in Referred Conference Proceedings

- M.Y. Amegadzie, O.T. Ola, O.A. Ojo, P. Wanjara and M.C. Chaturvedi: *On Liquation and Liquid Phase Oxidation during Linear Friction Welding of Nickel-Base IN 738 and CMSX-486 Superalloys,* Superalloy 2012 – The 12th International Symposium on Superalloys, 9-13 September, 2012, Pennsylvania, USA, pp.587-594

- O.T. Ola, O.A. Ojo, P. Wanjara and M.C. Chaturvedi: *Linear Friction Welding of Single Crystal Nickel-Base CMSX 486 Superalloy,* JOM-16 (16th International Conference on the Joining of Materials), Helsingør-Denmark 10-13 May 2011

- O.T. Ola, O.A. Ojo, P. Wanjara and M.C. Chaturvedi: *Crack-Free Welding of IN 738 by Linear Friction Welding,* Advanced Materials Research, 2011, Vol. 278, pp.446-453 (Presented at Euro Superalloy 2010)